VOLCANIC GAS QUANTIFICATION UNDER SUBOPTIMAL CONDITIONS

By

D. Skye Kushner, B.S., M.S.

A Dissertation Submitted in Partial Fulfillment of the Requirements for the Degree of

Doctor of Philosophy

In

Geoscience

University of Alaska Fairbanks

December 2023

APPROVED:

Dr. Taryn Lopez, Committee Chair

Dr. Christoph Kern, Committee member

Dr. Jessica Larsen, Committee member

Dr. William Simpson, Committee member

Dr. Bernard Coakley, Chair

Department of Geosciences

Dr. Karsten Hueffer, Dean

College of Natural Science and Mathematics

Dr. Richard Collins, Director

Graduate School

Abstract

Volcanic gas emissions are challenging to quantify. Achieving high confidence in gas composition, column concentrations, and emission rates acquired using remote sensing techniques is thought to require optimal atmospheric conditions. These conditions are often not met, creating a reluctance to preform measurements under non-ideal atmospheric conditions with inherent uncertainty about how useful those measurements may be. In the case of volcanic eruptions, the hazardous nature of the volcanic plume creates an environment where it is often not safe to collect measurements. This dissertation presents three projects which aim to constrain the quantity of two specific volcanic gases, mercury (Hg) and sulfur dioxide (SO_2), released under non-ideal measurement conditions. Specifically, chapter 2 aims to constrain Hg emission during volcanic eruptions, chapter 3 aims to characterize the uncertainty in SO_2 emission rates acquired under specific non-ideal atmospheric conditions, and chapter 4 aims to improve constraints on plume altitude for scanning remote sensing measurements of SO_2 emission rates acquired from a single instrument.

Ash is a potential sink of volcanically-sourced atmospheric mercury, and the concentration of particle-bound Hg may provide constraints on Hg emissions during eruptions. In Chapter 2, the Hg concentrations in 227 bulk ash samples from the Mt. Spurr (1992), Redoubt (2009), and Augustine (2006) volcanic eruptions are examined to investigate large-scale spatial, temporal, and volcanic-source trends. No significant difference in Hg concentrations is found in bulk ash by distance from the eruption source or for discrete eruptive events at each volcano, suggesting that in-plume reactions converting gaseous Hg^0 to adsorbed Hg^{2+} are happening on timescales shorter or longer than considered in this study (minutes to hours) and any additional in-plume controls may be masked by intra-volcanic sample variability. A significant difference is found in Hg concentration in ash among volcanic sources, which indicates that specific volcanoes may emit comparatively high or low quantities of Hg. These findings allow for the calculation of minimum, first-order estimates of volcanic Hg emissions during eruption in combination with total mass estimates of ashfall deposits. Mt. Spurr is found to be a high Hg emitting volcano such that its 1992 particulate Hg emissions likely contributed substantially to the global eruptive volcanic Hg budget for that year. Based on this study, previous approaches that used long-term Hg/SO_2 mass ratios to estimate eruptive total Hg under-account for Hg emitted in explosive events, and global volcanogenic Total Hg estimates need revisiting.

A large source of error in SO_2 emission rates derived from mobile differential optical absorption spectroscopy (DOAS) is the uncertainty in atmospheric light paths between the scattered sunlight and the instrument, particularly under non-ideal atmospheric conditions such as the presence of clouds beneath the volcanic plume. In Chapter 3, numerical simulations using the McArtim model are used to examine

the radiative transfer associated with zenith-facing mobile DOAS traverses for scenarios where there is a cloud layer between the instrument and the volcanic plume. In total, 217 permutations of atmospheric optical conditions are considered, allowing for the determination of errors associated with atmospheric scattering. Objective criteria are also developed for selecting SO_2 baselines and plume limits for each simulated traverse. This study then applies models to a real-world dataset from the 2021 Cumbre Vieja eruption to explore the effects of ground-level haze on a measured SO_2 column densities for the volcanic plume. All modeling results find large modifications in the shape of the analyzed plume SO_2 column density versus distance curve, even under scenarios with translucent clouds. Despite modification of the plume shape, the presence of a low cloud or haze layer is typically not a large source of error in determination of the total SO_2 quantity measured over the entirety of the traverse, which suggests that fairly accurate SO_2 emission rate measurements can be obtained even under non-ideal atmospheric measurement conditions. The real-world dataset from Cumbre Vieja is found to be best explained by a layer of ground-level laze containing SO_2 and a volcanic plume located between 2 – 4 km altitude.

A large source of uncertainty in SO_2 emission rates derived from scanning DOAS instruments is the cross-sectional area of the detection, which is determined from the vertical and horizontal distance of the plume from the instrument. In Chapter 4, a novel method is employed to estimate plume altitude based on modeled wind speed data and validated against available webcam imagery at Cleveland Volcano in the Aleutian Islands, Alaska. This estimated plume altitude is used to calculate SO_2 emission rates from single-station campaign scanning DOAS measurements at Cleveland Volcano, Gareloi Volcano, and Korovin Volcano (Alaska) in 2019, where the instrument was deployed for several days at each site. This method is also applied to a long-term dataset of scanning SO_2 measurements acquired from a permanent scanning DOAS instrument installed at Cleveland Volcano September 2022 – June 2023. It is found that the method of estimating plume altitude in the long-term dataset produces a lower emission rate and a smaller sample variance than assuming a fixed summit plume altitude. The remaining variance in the data is then interpreted to represent variability in SO_2 emissions during times of relative quiescence at each studied volcano.

Table of Contents

Page

List of Figures

Page

List of Tables

Page

List of Frequently Occurring Abbreviations

Chapter 2:

GEM – Gaseous Elemental Mercury

GOM – Gaseous Oxidized Mercury

PBM – Particulate Bound Mercury

THg – Total Mercury

VEI – Volcanic Explosivity Index

Chapter 3:

DOAS – Differential Optical Absorption Spectroscopy

SZA – Solar Zenith Angle

AOD – Aerosol Optical Depth

CSB – Cross-sectional Burden

SCD – Slant Column Density

VCD – Vertical Column Density

Chapter 4:

NOVAC – Network for Observation of Volcanic and Atmospheric Change

Acknowledgements

Reflecting on the possibilities of my youth, finishing a doctorate was not something I thought would be open to me. So firstly, thank you to my advisor, Taryn Lopez, for taking a risk in bringing me on as a PhD student, securing funding to keep my research going, and allowing me to participate in extended periods of fieldwork. As your first PhD student, I think this was a learning experience for both of us and the flexibility you showed between a delayed project, the onset of a global pandemic, and the added blessing of managing students with a growing family is more than anyone could have asked for. Thanks are also owed to Pavel Izbekov, Valerie Wasser, Julia Gestrich, and Alex Iezzi for suggesting I go to UAF in the first place.

Thank you to the rest of the Lopez cohort, Valerie Wasser and Pablo Saunders-Shultz, for keeping me sane through this process and taking over satellite SO_2 monitoring when I was too busy writing this dissertation.

Thank you to the entire Alaska Volcano Observatory staff for allowing me the privilege of conducting fieldwork in the Aleutians and allowing me to participate in monitoring and conversations. A special thank you to all observatory technicians for working diligently to ensure gas flight time during the cruises in which I participated, and for putting up with me over long stretches aboard the ship. A very special thank you, of course, to Max Kaufman, without whom my stations would be sitting in a box in Fairbanks.

Thank you to the Cascades Volcano Observatory staff for advice and equipment on and off the ship. Thank you to Allan Lerner for creating the "friends of gas distinction," which helps to drive an outsized amount of work from non-gas people.

Thank you to my advisory committee, Christoph Kern, Jessica Larsen, and William Simpson, for the undue amount of time needed to review my writing and guide me through this process.

Thank you to my family, Cara Kushner, Paul Kushner, and Gayle Fiks, for not completely understanding the content of this thesis or my life choices, but at least attempting to understand.

Thank you to Mike Walleri and Kathy Hodges for graciously opening up their home to me when I first arrived in Fairbanks, through to the end. I cannot express enough gratitude for how much easier this entire degree has been with your help.

Thank you to Jennifer Moses, Ron Beller, Jesse Beller, Vita Newstetter, and Leah Beller, for the continued support and unwavering encouragement.

Thank you to Sarah Beller, without whom the sun does not rise.

And finally, thank you to my mother, Linda Cohen, who I hope would have been proud.

Chapter 1 Introduction

Volcanoes are geologically transient features. Some have been persistently active throughout human history; others have been sporadically active, only infrequently erupting; and a large portion on this planet will never erupt again. Despite the hazards posed by historically violent eruptions, a significant portion of humanity—1.1 billion people as of 2015—live within 100 km of a volcano which has erupted within the last 10,000 years (Freire et al., 2019). With a globalized economy volcanoes provide additional threats to humanity as explosive eruptions now disrupt air travel along routes far from populated areas (Guffanti et al., 2010). While many of the volcanoes closest to population centers are near infrastructure which would support a robust monitoring network (transport access, power), a large portion are not. In the state of Alaska, several eruptions occur each year along the Aleutian-Alaska Arc from remote, and in some cases unmonitored or sparsely monitored, volcanoes (Cameron et al., 2018). Field campaigns to install or maintain geophysical equipment, make gas measurements, and/or collect geologic or volcanic gas samples at Alaska volcanoes are frequently conducted each summer. However, only a fraction of the 54 historically active volcanoes within the state are visited each year (Cameron et al., 2022). This dissertation aims to enhance the constraints on volcanic degassing from these remote volcanoes, especially for cases when regular and robust monitoring is challenging, and sample collection opportunities are limited.

The following section will provide a general background on sources of volcanic gas emission and the methods by which they are quantified. This introduction will focus on quantifying the release of mercury (Hg) and sulfur dioxide (SO_2) from volcanic sources, the volcanic gases targeted in this study.

1.1 Volcanic gas sources

Gases released from volcanoes originate from a mixture of mantle, slab, and crustal sources, depending on the tectonic setting (Aiuppa et al., 2017). The mantle, to some degree, contains water, carbon, sulfur, and trace concentrations of other volatile species which may enter a magmatic phase with the onset of melt generation. The crust and slab, by contrast, contain notable compositional differences from the mantle. It is difficult to generalize the chemical composition of a slab due to significant variations along slab segments or between different slabs with respect to organic elements such as carbon and nitrogen, but one important characteristic of subducting slabs is that they contain substantially more water content than the mantle (Plank et al., 2013) and generally more sulfur (Oppenheimer et al., 2014).

Bodies of magma are compositionally variable, depending on processes of melt generation and evolutionary trends. Magma itself is a byproduct of tectonic processes (subduction and rifting) or mantle upwelling (hotspots). When material that is stable under a specific field of heat or pressure moves to new fields of instability, melt may be generated (Cas and Wright, 1988). In the case of arc-magmatism, the

zone of instability is related to the increased supply of heat from the mantle and the pressure of subduction in addition to a lowering of the melting point of mantle material in the presence of water (Kushiro et al., 1968). As an oceanic slab is subducted beneath the crust, rising heat and pressure coupled with water fluxing leads to conditions in which melt may be generated, at approximately 100 km depth (Wada et al., 2008), along the hydrous upper portion of the slab. Certain assemblages of minerals may also be melted as pressure is removed through decompression, as is the case with the upper mantle at midocean ridges or during continental rifting events. In the case of rift magmatism, a decrease in pressure caused by two tectonic plates pulling apart may cause melting (Bonin, 2007). In the case of hotspot magmatism, magma at great depths within the primordial lower mantle is advected into the upper mantle (Carey and Bursik, 2015). In rare cases during large orogenic events, magma may also be generated close to the surface through compression (Roger et al., 2010). In all cases, the melt generated is less dense than the surrounding material and thus more buoyant. The natural tendency of buoyant bodies is to migrate upwards through the crust as diapirs (Pitcher, 1979) or through channels as dikes (Vigneresse and Clemons, 2000). Magma includes the generated melt, but also any solid crystals, and gaseous or supercritical components (Cas and Wright, 1988). These multiphase components evolve within the magma over time during magma ascent as pressures and temperatures decrease. Different temperature and pressure conditions lead to different zones of stability, allowing for mineral formation within the magma body. Initial mineral content in a melt may be minor and sparsely distributed but granted enough time or the proper conditions to facilitate growth, a melt may become dominated by solid phase minerals. Magma bodies may remain buoyant and sufficiently upwardly mobile to facilitate a volcanic eruption up to approximately 50 – 70% crystallinity by volume (Sparks et al., 2019).

The composition of volatiles dissolved in magmas vary through time as magma evolves and ascends. As a body migrates upwards into the shallow crust, a loss of pressure induces volatiles previously dissolved in melt to exsolve – or form a new volatile phase in equilibrium with the melt. The point at which a melt is saturated with respect to a particular volatile species depends on several factors, though most importantly by pressure. In the case of noble gases, carbon, and helium, the point of volatile saturation within melt and volatile exsolution is quite deep (Giggenbach et al., 1996). For other species such as sulfur and water the point of exsolution is generally shallower in the crust, and other species such as halogens may remain dissolved in the melt until shallow depths (Giggenbach et al., 1996). As a body stalls in the crust, cooling may lead to magma crystallization, which can further induce volatile exsolution. Other metals may partition from the melt into exsolved volatile phases in the form of chemical complexes, as is the case for chalcophile elements. As volatiles move to shallower depths than the melt, lower pressures and temperatures or interaction with wall rocks along fracture zones may favor

mineralization. This process of concentrating economically important elements forms the basis of many important ore deposit models.

1.2 Volcanic gas emission

Much like their source magmas, volcanic gas emissions are compositionally variable and evolve with time. Generally, the primary gases released from volcanoes are water (H_2O), carbon dioxide (CO_2), and sulfur species (SO_2, H_2S). In addition to major gases, trace compounds (halogens, noble gases) and metals including mercury (Hg) are measurable (Giggenbach et al., 1996; Oppenheimer et al., 2014). The relative proportions of these species vary among volcanoes, and over time within the same volcano. One of the most important discoveries within the volcanic gas community with relevance to volcanic monitoring is that over time and as conditions change within the subsurface, the rate and relative proportions of gas emissions may change (Aiuppa et al., 2007). As discussed in the previous sections, the relative proportions of emitted gases may be altered by introducing fresh magma from depth, which will tend to be CO_2-rich relative to SO_2 (Werner et al., 2013). During ascent, a particular species may also be removed as may be the case with SO_2 in response to interactions with groundwater or wall rock material (Symonds et al., 2001). The relative proportions of these gaseous species, such as CO_2/SO_2 or H_2O/CO_2 may be used to infer exsolution depth or the subsurface processes modifying gas emissions. Deviations in the normal proportions of gases or changes in the total volcanic gas flux may be linked to changing conditions within the volcano (Aiuppa et al., 2017; Shinohara et al., 2008). The ability to establish a background degassing baseline and confidently measure changes in emitted gaseous species thus becomes a high priority for volcano observatories and researchers alike.

Once volcanic gases have exsolved from their host magma, they may remain with their host magma in what is referred to as closed-system degassing or separate from their host magma in what is referred to as open-system degassing (Oppenheimer et al., 2014). If permeable pathways exist, these exsolved gases can travel up the conduit into the atmosphere through an "open" volcanic vent. Alternatively, if the conduit or vent are sealed, the gases may accumulate within the upper part of the volcanic system at shallow depths. Vent and conduit permeability may vary, and some volcanoes may transition between open and closed vents through time (Reath et al., 2018). Much like open and closed vent behavior, volcanoes may also transition between open and closed systems of degassing.

1.3 Insights into volcanic systems from gas emissions

In addition to the relative proportion of different volcanic gases, the absolute flux or emission rate of a specific gas species may give insight into the subsurface magmatic system. As discussed later in this section, it is relatively easy to measure the emission rate of SO_2 using remote techniques and thus changes to the emission rate may be monitored to provide insights into the volcanic system. If more SO_2 relative

to background is measured, it may be indicative of magma recharge—when a volatile-rich, deep magma source has moved to a shallower depth (Wallace, 2001). Conversely, if a lower SO_2 emission rate is measured relative to baseline, it may be indicative of conduit sealing and potential overpressure of the system (Edmonds et al., 2003). In both cases the baseline SO_2 emission rate and natural variability must be accurately established to determine if a change has occurred.

Mercury is also present in volcanic plumes and requires specific direct sampling or in situ measurement techniques which make its quantification challenging. Nonetheless, research related to volcanic Hg emissions is important due to the toxicity of the metal to biota and its relatively long atmospheric lifetime in gaseous elemental state (2 – 6 months; Driscoli et al., 2013). Studies have documented a difference between the concentration of Hg within volcanic plumes along volcanic arc settings and between arc and non-arc volcanoes (Edwards et al., 2021), which implies that there is a source control mechanism for Hg emissions. As a benefit of its long atmospheric lifetime, Hg has also been found to be a useful marker in the geologic record for periods of high volcanic output related to continental breakup and the creation of large igneous provinces (Svensen et al., 2023).

1.4 Quantification of gas emissions

Quantifying volcanic gas emissions can be done using an array of collection and analytical techniques. Generally, the techniques can be divided into the broad categories of remote, and direct or in situ methods. Direct gas sampling and in situ methods involve collecting gases at their emission source or measuring gases within a mixed volcanic gas–air plume, respectively, whereas remote measurements are commonly performed at a distance, generally via techniques measuring absorption of infrared, visible, and ultraviolet radiation bands by volcanic gases. Below we focus primarily on the remote and in situ measurement techniques related to this study.

1.4.1 Remote measurement techniques

The use of remote sensing for volcanic gas emission quantification began in the 1980's with the adaptation of atmospheric instruments developed for quantifying SO_2 pollution from coal power plants to volcanic plumes (Milan, 1980; Stoiber et al., 1983). The original instrument, the correlation spectrometer (COSPEC), used absorption spectroscopy—the loss of radiation at molecularly characteristic quantities of energy—to measure atmospheric concentration of SO_2. COSPEC instruments, while pivotal to early studies, were difficult to transport due to their large size and weight, required calibration between each use, and are no longer produced and thus minimally available for volcanic gas studies today.

More recently, lower cost portable UV spectrometer based instruments were developed using a slightly different absorption spectroscopy method: differential optical absorption spectroscopy, commonly referred to as DOAS (Galle et al., 2003). The DOAS technique examines a differential absorption cross

section, where broad band features are removed to enable the column density (in mol cm^{-2}), or the concentration of overlying species from the photon source to the instrument (elaborated on in chapter 3), of characteristic narrow band absorption features to be determined. A series of column density measurements of the target gas species, in our case SO_2, can be compiled to form a two-dimensional cross section of the plume (in molec cm^{-1}), representing the concentration of a species within the cross section. A third dimension—time—may be added by multiplying the plume SO_2 cross section by windspeed to calculate an emission rate (also known as flux) which represents the mass of SO_2 released to the atmosphere over a unit of time (in t day^{-1} or kg s^{-1}). When applied to volcanic plumes, a series of DOAS measurements across the volcanic plume can be used to construct a two-dimensional slice of a plume via one of two methods: (1) the traverse method, where the spectrometer is pointed up and carried beneath a plume, or (2) the scanning method, in which the instrument scans across a plume from a fixed position. Both methods have advantages and disadvantages. With the traverse method plume geometry is simple to quantify and effects of radiative transfer are less substantial. Conversely, with the scanning method, plume geometry and atmospheric radiative transfer become more difficult to resolve, but measurements can be automated and collected continuously over extended time periods. DOAS instruments have a significant advantage over COSPEC, as they are much smaller, lighter, and more portable, and can be built using off-the-shelf components (Platt and Stutz, 2008). DOAS instruments are now widely used among the remote volcanic gas measurement community due to their ease of use and low instrument cost, and a strategic funding initiative to provide volcano monitoring instruments via the NOVAC project, which seeks to set up networks of similarly modulated DOAS instruments at high-priority volcanoes (Galle et al., 2010).

1.4.2 Direct and in situ measurement techniques:

Direct collection methods are particularly useful for quantifying total gas composition, which is not possible with a single remote sensing technique. The quintessential method of volcanic gas sampling, the Giggenbach method (Giggenbach, 1975), was described first in the 1970's and is still in use almost 50 years later with small variations (Sortino et al., 2006). This method collects gases using an evacuated flask or bottle containing an absorbing solution and allows for analysis of most of the major and trace volcanic gas species.

An alternative to Giggenbach flasks for quantifying major-species gas composition are multicomponent gas analyzer systems (multiGAS), which were first described and developed for volcanic purposes in the early 2000's (Aiuppa et al., 2005; Shinohara et al., 2005). These devices typically consist of a pump to pull volcanic plume gases through a series of in-line electrochemical and infrared sensors to simultaneously determine concentrations for multiple volcanic gas species. Typical multiGAS

instruments include sensors to quantify CO_2, SO_2, H_2S, and H_2O, and some variations include sensors for other gases such as H_2 (Aiuppa et al., 2011) or CH_4 (Salas-Navarro et al., 2022). MultiGAS and multiGAS-type variants attached to helicopters and drones have successfully collected valuable plume gas composition information (de Moor et al., 2019). The advantage of airborne collection is that it allows for constraints to be placed on variables such as plume altitude and wind speed which may be important for complementary studies.

Some alternatives now exist to measure volcanic species of interest which are not initially trapped or easily resolved using the Giggenbach method or measured in situ such as through MultiGAS. Collecting or characterizing metals emitted from volcanoes in the particulate phase on filter paper is common (Martin et al., 2012; Ilyinskaya et al., 2021), or on specialized traps consisting of either gold-coated sand or iodated carbon, in the case of elemental gaseous Hg. Some limited efforts have been made to collect for speciated forms of Hg by attaching a chemically coated denuder and glass wool before the gaseous elemental Hg section to collect for oxidized Hg gases and Hg absorbed to particles (Witt et al., 2008). If a pump with a known flow rate (generally in l min^{-1}) is used to control the flow of gas through a trap, then the in-plume concentration (in weight or molecules m^{-3}) can be established. If an Hg trap with a known flow rate is attached in-line or nearby a multiGAS instrument analyzing for SO_2, then it is possible to establish a volume-normalized ratio of Hg to SO_2. Once this ratio is established, it is possible to estimate a total volcanic Hg emission rate by using DOAS-derived SO_2 emission rate or flux (Werner et al., 2013). The proxy method of extrapolating emission rate by using SO_2 as a "tracer gas" is broadly applicable to other species for which emission rate may not be easily resolved using remote sensing (e.g., CO_2). One key assumption for this method is that the target gas-tracer gas ratio does not change in time.

1.5 Overview of Dissertation Chapters

This dissertation will present three chapters unified around the theme of quantifying volcanic gas measurements from limited or incomplete datasets. The motivation behind this work is the difficulty of obtaining accurate measurements under specific eruptive, atmospheric, or instrumental conditions. Thus, the aim for each chapter is to present a new method to better constrain emission of a particular volcanic volatile species given a specific limitation. Chapter 2 investigates emissions of volcanic mercury (Hg) deposited on ash from recent eruptions within the Cook Inlet area of Alaska; Chapter 3 investigates the influence of below-plume clouds or fog on DOAS measurements of SO_2 absorption, to characterize when these data can provide robust constraints on SO_2 emission rate; and Chapter 4 develops a novel technique to estimate plume altitude using modeled wind speed to minimize uncertainties in single-station DOAS deployments and presents SO_2 emission rates from a set of three remote Alaska volcanoes.

1.5.1 Overview of Chapter 2: Estimates of volcanic mercury emissions from Redoubt Volcano, Augustine Volcano, and Mt. Spurr eruption ash

Chapter 2 provides some of the first quantification of volcanic mercury emission during eruptions. The main logistic challenge behind quantifying eruptive mercury emissions is the need for in plume sample collection, which is often not feasible during eruptions. This study aims to minimize this knowledge gap by taking advantage of the rapid absorption of emitted gaseous Hg^0 onto the surface of volcanic ash particles to form particulate-bound mercury (von Glasow, 2010). Ash samples from well-characterized Alaska eruptions are used to determine if there are spatial, temporal, or geographic variations in the amount of Hg absorbed to ash. In total, 227 ash samples were analyzed to find that there are no discernable patterns in the concentration of Hg on an ash sample from the distance from the eruption source or over time within an eruptive sequence. This study found a significant difference in the amount of Hg emitted from different volcanoes. Because there does not appear to be a correlation at any volcano between Hg concentration and distance from the vent or eruptive event, an average mass of Hg per mass of ash is appropriate for extrapolating total hg emissions for individual volcanoes so long as there is a significant sample size to account for potential bias from large sample variance. Thus, if there are sufficient samples to estimate an eruptive mass for any single volcanic eruption then it should be possible to put minimum constraints on the total amount of volcanic emitted Hg. This study provides a simple framework to constrain minimum volcanic Hg fluxes during volcanic eruptions from three Alaska volcanoes, with the potential for global application. This paper was published in *Frontiers* as Kushner et al. (2023).

1.5.2 Overview of Chapter 3: The ghost plume phenomenon and its impact on Mobile DOAS measurements of SO_2 emission rates

Chapter 3 examines a phenomenon known as a "ghost plume" which has been identified but not well-characterized within the volcanic gas community (e.g., Williams-Jones et al., 2008). The emergence of a ghost plume is related to the scattering of sunlight when there is a condensed layer, such as cloud or fog, in the atmosphere between a measuring instrument and a volcanic plume. The ghost plume effect results in an appearance of an illusory volcanic plume in addition to or instead of the real volcanic plume. The phenomenon's effect on DOAS traverses has previously been unquantified. This unknown and potentially large effect on SO_2 emission rates under these conditions has led many researchers to dismiss or not collect data under these conditions. The goal of this project was to quantify and characterize the effect of below-plume clouds on derived SO_2 emission rates. In this study, a series of radiative transfer simulations were conducted in order to quantify error in the SO_2 absorption cross section acquired during a DOAS traverse with a condensed aerosol layer (i.e., cloud) between the instrument and volcanic plume.

Simulations for a series of atmospheric conditions show that while the shape of a DOAS traverse cross section may change drastically with different atmospheric conditions, the SO_2 cross sectional burden and derived emission rate remains within approximately ± 25% of their true values. These simulations are then used to investigate a potential ghost plume observed in a DOAS transect during the 2021 eruption of Cumbre Vieja Volcano, Canary Islands. This paper has gone through coauthor review and will be submitted for publication to *Volcanica* (www.jvolcanica.org) soon.

1.5.3 Overview of Chapter 4: Using modeled windspeeds to estimate volcanic plume altitude with application to single-station Scanning DOAS-derived SO_2 emission rates from Cleveland, Korovin and Gareloi Volcanoes, Alaska

Chapter 4 aims to provide an independent way to estimate plume altitude, an important input parameter for calculating SO_2 emission rates from scanning DOAS measurements, and thereby reduce measurement uncertainties when only one DOAS station is available. Properly constraining the plume altitude is important for interpreting the plume's true width, and from it the number of SO_2 molecules in a two-dimensional plume cross section. In ideal cases, two or more stationary scanning DOAS stations are deployed around a volcano to allow simultaneous detection of the plume and geometric quantification of the plume altitude, which is used to calculate the width of the plume and total SO_2 cross sectional burden of each DOAS scan. In 2019 in conjunction with Alaska Volcano Observatory fieldwork, single-station campaign scanning DOAS instruments were deployed at Gareloi Volcano, Korovin Volcano, and Cleveland Volcano in the Aleutian Islands, Alaska. In addition to these single-station campaign DOAS deployments, one permanent scanning DOAS was installed at Cleveland Volcano in 2022. While these campaign-style deployments have the advantage of automatically acquiring high temporal resolution measurements of volcanic SO_2 flux over days of deployment, with only one station it is not possible to solve for plume altitude, which creates large uncertainties in derived emission rates. This chapter presents a new method to constrain plume altitude from modeled wind data, which ultimately improves the precision of single-station DOAS derived SO_2 emission rates. This method is based on the inverse relationship between wind speed and plume altitude during passive degassing conditions, where high winds lead to ground-hugging or grounded plumes and light winds lead to lofted plumes. Twenty-three webcam images with views of Cleveland Volcano were used to estimate plume altitudes, which are then paired with coincident modeled windspeeds to construct a fitted regression. Estimated plume altitude based on this regression line are shown through this project to improve precision of values and provide better agreement with helicopter DOAS traverses during periods when windspeed is highly variable. This method can be applied to increase the amount of SO_2 emission rate data collected, especially for remote

and/or resource-limited volcanoes where only one DOAS station may be installed or operating. This paper will be distributed for coauthor review soon.

1.6 References

Aiuppa, A., Federico, C., Giudice, G., and Gurrieri, S. (2005). Chemical mapping of a fumarolic field: La Fossa Crater, Vulcano Island (Aeolian Islands, Italy). *Geophysical Research Letters*, 32, L13309. doi:10.1029/2005GL023207.

Aiuppa, A., Moretti, R., Federico, C., Giudice, G., Gurrieri, S., Liuzzo, M., Papale, P., Shinohara, H., and Valenza, M. (2007). Forecasting Etna eruptions by real-time observation of volcanic gas composition. *Geology*, 35 (12), 1115-1118. doi:10.1130/G24149A.1.

Aiuppa, A., Shinohara, H., Tamburello, G., Giudice, G., Liuzzo, M., and Moretti, R. (2011). Hydrogen in the gas plume of an open-vent volcano, Mount Etna Italy. *Journal of Geophysical Research,* 116: B10204. doi:10.1029/2011JB008461.

Aiuppa, A., Fischer, T.P., Plank, T., Robidoux, P., and Napoli, R.D. (2017). Along-arc, inter-arc and arc-to-arc variations in volcanic gas CO2/ST ratios reveal dual source of carbon in arc volcanism. *Earth-Science Reviews*, 168, 24-47. doi:10.1016/j.earscirev.2017.03.005.

Bonin, B. (2007). A-type granites and related rocks: Evolution of a concept, problems and prospects: *Lithos*, v. 97, p. 1-29. doi:10.1016/j.lithos.2006.12.007.

Cas, R.A.F., and J. V. Wright (1988). *Volcanic Successions Modern and Ancient*, 1-532 pp., Chapman & Hall, London.

Cameron, C.E., Prejean, S.G., Coombs, M.L., Wallace, K.L., Power, J.A., and Roman, D.C. (2018). Alaska Volcano Observatory Alert and Forecasting Timeliness: 1989–2017. *Frontiers in Earth Science*, 6(86). doi:10.3389/feart.2018.00086

Cameron, C.E., Schaefer, J.R., and Perreault, J.M., (2022). Historically active volcanoes of Alaska. Alaska Division of Geological & Geophysical Surveys Miscellaneous Publication 133 v. 5, 2 sheets. doi:10.14509/30851

Carey, S., and M. Bursik (2015). Volcanic Plumes, *in The Encyclopedia of Volcanoes*, edited by H. Sigurdsson, pp. 571-585, Elsevier Inc., doi:10.1016/B978-0-12-385938-9.00032-8.

Driscoli, C.T., Mason, R.P., Chan, H.M., Jacob, D.J., and Pirrone, N. (2013). Mercury as a global pollutant: sources, pathways, and effects. *Environmental Science and Technology*, 47(10), 4967–38. doi:10.1021/es305071v.

Edmonds, M., Oppenheimer, C., Pyle, D.M., Herd, R.A., and Thompson, G. (2003). SO2 emissions from Soufrière Hills Volcano and their relationship to conduit permeability, hydrothermal interaction and degassing regime. Journal of Volcanology and Geothermal Research, 124(1-2), 23-43. doi:10.1016/S0377-0273(03)00041-6.

Edwards, B.A., Kushner, D.S., Outridge, P.M., and Wang, F. (2021). Fifty years of volcanic mercury emission research: Knowledge gaps and future directions. *Science of the Total Environment*, 757, 143800. doi:10.1016/j.scitotenv.2020.143800

Freire, S., Florczyk, A.J., Pesaresi, M., and Sliuzas, R. (2019). An Improved Global Analysis of Population in Proximity to Active Volcanoes, 1975–2015. *International Journal of Geo-Information*, 8(8), 341. doi:10.3390/ijgi8080341

Galle, B., Johansson, M., Rivera, C., Zhang, Y., Kihlman, M., Kern, C., Lehmann, T., Platt, U., Arellano, S., and Hidalgo, S. (2010). Network for Observation of Volcanic and Atmospheric Change (NOVAC)—A global network for volcanic gas monitoring: Network layout and instrument description. *Journal of Geophysical Research*, 115. doi:10.1029/2009JD011823.

Galle, B., Oppenheimer, C., Geyer, A., McGonigle, A.J.S., Edmonds, M., and Horrocks, L. (2003). A miniaturised ultraviolet spectrometer for remote sensing of SO2 fluxes: a new tool for volcano surveillance. *Journal of Volcanology and Geothermal Research*, 119(1–4), 241-254. doi:10.1016/S0377-0273(02)00356-6.

Giggenbach, W.F. (1975). A simple method for the collection and analysis of volcanic gas samples. *Bulletin of Volcanology*, 39, 132-145.

Giggenbach, W.F. (1996). Chemical composition of volcanic gases. *in Monitoring and Mitigation of Volcano Hazards*, edited by R. Scarpa and R. I. Tilling, pp. 221-256, Springer, Berlin, doi:10.1007/978-3-642-80087-0_7.

von Glasow, R. (2010). Atmospheric Chemistry in Volcanic Plumes. *Proceedings of the National Academy of Sciences,* 107(15), 6594-99. doi:10.1073/pnas.0913164107.

Guffanti, M., Casadevall, T.J., and Budding, K. (2010). Encounters of aircraft with volcanic ash clouds; A compilation of known incidents, 1953–2009: *U.S. Geological Survey Data Series 545*, ver. 1.0, 12 p., plus 4 appendixes including the compilation database, <http://pubs.usgs.gov/ds/545>.

Ilyinskaya, E., Mason, E., Wieser, P.E., Holland, L., Liu, E.J., Mather, T.A., Edmonds, M., Whitty, R.C., Elias, T., Nadeau, P.A., Schneider, D., McQuaid, J.B., Allen, S.E., Harvey, J., Oppenheimer, C., Kern, C., and Damby, D. (2021). Rapid metal pollutant deposition from the volcanic plume of Kīlauea, Hawai'i. *Communications Earth & Environment*, 2, 78. doi:10.1038/s43247-021-00146-2.

Kushiro, I., Syono, Y., and Akimoto, S. (1968). Melting of a peridotite nodule at high pressures and water high water pressures. *Journal of Geophysical Research*, 73, 6023-6029. doi:10.1029/JB073i018p06203.

Kushner, D.S., Lopez, T.M., Wallace, K.L., Damby, D.E., Kern, C., and Cameron, C.E. (2023): Estimates of volcanic mercury emissions from Redoubt Volcano, Augustine Volcano, and Mount Spurr eruption ash. *Frontiers in Earth Sciences*, 11:1054521. doi:10.3389/feart.2023.1054521

Martin, R.S., Sawyer, G.M., Day, J.A., LeBlond, J.S., Ilyinskaya, E., and Oppenheimer, C. (2012). High-resolution size distributions and emission fluxes of trace elements from Masaya volcano, Nicaragua. *Journal of Geophysical Research*, 117, B08206, doi:10.1029/2012JB009487.

Millán, M.M. (1980). Remote sensing of air pollutants. A study of some atmospheric scattering effects. *Atmospheric Environment*, 14, 1241-1253.

de Moor, J.M., Stix, J., Avard, G., Muller, C., Corrales, E., Diaz, J.A.,, Alan, A., Brenes, J., Pacheco, J., Aiuppa, A., and Fischer, T.P. (2019). Insights on hydrothermal-magmatic interactions and eruptive processes at Poás volcano (Costa Rica) from high-frequency gas monitoring and drone measurements. *Geophysical Research Letters*, 46, 1293–1302. doi:10.1029/2018GL080301

Oppenheimer, C., Fischer, T., and Scaillet, B. (2014). Volcanic degassing: process and impact. H.D. Holland, K.K. Turekian (Eds.), *Treatise on Geochemistry* (Second edition), Elsevier. Pp. 111-179. doi:10.1016/B978-0-08-095975-7.00304-1.

Pitcher, W.S. (1979). The nature, ascent and emplacement of granitic magmas. *Journal of the Geological Society*, 136(6), 627-662. doi:10.1144/gsjgs.136.6.0627.

Plank, T., Kelley, K.A., Zimmer, M.M., Hauri, E.H., Wallace, P.J. (2013): Why do mafic arc magmas contain ~4 wt% water on average?. *Earth and Planetary Science Letters*, 364, 168-179. doi:10.1016/j.epsl.2012.11.044.

Platt, U. and Stutz, J. (2008). Differential Optical Absorption Spectroscopy: Principles and Applications; Springer Berlin Heidelberg.

Reath, K., Pritchard, M., Poland, M., Delgado, F., Carn, S., Coppola, D., Andrews, B., Ebmeier, S.K., Rumpf, E., Henderson, S., Baker, S., Lundgrin, P., Wright, R., Biggs, J., Lopez, T., Wauthier, C., Moruzzi, S., Alcott, A., Wessels, R., Griswold, J., Ogburn, S., Loughlin, S., Meyer, F., Vaughan, G., and Bagnardi, M. (2019). Thermal, deformation, and degassing remote sensing time series (CE 2000–2017) at the 47 most active volcanoes in Latin America: Implications for volcanic systems. *Journal of Geophysical Research: Solid Earth*. 124, 195–218. doi:10.1029/2018JB016199.

Roger, F., Jolivet, M., and Malavieille, J., (2010). The tectonic evolution of the Songpan-Garzê (north Tibet) and adjacent areas from Proterozoic to present: A synthesis. *Journal of Asian Earth Sciences*, 39, 254-269. Doi:10.1016/j.jseaes.2010.03.008.

Salas-Navarro, J., Stix, J., and de Moor, J.M. (2022). A new Multi-GAS system for continuous monitoring of CO2/ CH4 ratios at active volcanoes. *Journal of Volcanology and Geothermal Research*, 426. doi:10.1016/j.jvolgeores.2022.107533.

Shinohara, H. (2005). A new technique to estimate volcanic gas composition: plume measurements with a portable multi-sensor system. *Journal of Volcanology and Geothermal Research*, 143(4), 319-333. doi:10.1016/j.jvolgeores.2004.12.004.

Shinohara, H., Aiuppa, A., Giudice, G., and Liuzzo, M. (2008). Variation of H_2O/CO_2 and CO_2/SO_2 ratios of volcanic gases discharged by continuous degassing of Mount Etna volcano, Italy. *Journal of Geophysical Research*, 113, B09203. doi:10.1029/2007JB005185.

Sortino, F., Nonell, A., Toutain, J.P., Munoz, M., Valladon, M., and Volpicelli, G. (2006). A new method for sampling fumarolic gases: Analysis of major, minor and metallic trace elements with ammonia solutions. *Journal of Volcanology and Geothermal Research*, 158(3-4), 244-256. doi:10.1016/j.jvolgeores.2006.05.005.

Sparks, R.S.J., Annen, C., Blundy, J.D., Cashman, K.V., Rust, A.C., and Jackson, M.D. (2019). Formation and dynamics of magma reservoirs. Philosophical Transactions of the Royal Society, A 377, 20180019. doi:10.1098/rsta.2018.0019.

Stoiber, R.E., Malinconico, L.L., and Williams, S.N. (1983). Use of the correlation spectrometer at volcanoes. In: Tazieff H, Sabroux, JC (ed) *Forecasting volcanic events*. Elsevier, Amsterdam, 424-444.

Svensen, H.H., Jones, M.T., Percival, L.M.E., Grasby, S.E., and Mather, T.A. (2023). Release of mercury during contact metamorphism of shale: Implications for understanding the impacts of large igneous province volcanism. *Earth and Planetary Science Letters*, 619. doi:10.1016/j.epsl.2023.118306.

Symonds, R.B., Gerlach, T.M., and Reed, M.H. (2001). Magmatic gas scrubbing: implications for volcano monitoring. *Journal of Volcanology and Geothermal Research*, 108(1-4), 303-341. doi:10.1016/S0377-0273(00)00292-4.

Vigneresse, J.A., & Clemens, J.D. (2000). Granitic magma ascent and emplacement: neither diapirism nor neutral buoyancy. *Geological Society,* London, Special Publications, 174(1), 1-19.

Wada, I., Wang, K., He, J., and Hyndman, R.D. (2008). Weakening of the subduction interface and its effects on surface heat flow, slab dehydration, and mantle wedge serpentinization, *Journal of Geophysical Research*, 113, B04402. doi:10.1029/2007JB005190.

Wallace, P.J. (2001). Volcanic SO2 emissions and the abundance and distribution of exsolved gas in magma bodies. *Journal of Volcanology and Geothermal Research*, 108(1-4), 85-106. doi:10.1016/S0377-0273(00)00279-1.

Werner, C., Kelly, P.J., Doukas, M., Lopez, T., Pfeffer, M., McGimsey, R., and Neal, C. (2013): Degassing of CO2, SO2, and H2S associated with the 2009 eruption of Redoubt Volcano, Alaska. *Journal of Volcanology and Geothermal Research*, 259, 270-284. doi:10.1016/j.jvolgeores.2012.04.012.

Williams-Jones, G., Stix, J., and Hickson, C. (2008). The COSPEC Cookbook: Making SO2 Measurements at Active Volcanoes. *IAVCEI Methods in Volcanology*, 1, 121-167. doi:10.13140/RG.2.2.13728.99845.

Witt, M.L.I., Mather, T.A., Pyle, D.M., Aiuppa, A., Bagnato, E., and Tsanev, V.I. (2008). Mercury and Halogen Emissions from Masaya and Telica Volcanoes, Nicaragua. *Journal of Geophysical Research: Solid Earth,* 113(6), 1–15. doi:10.1029/2007JB005401.

Chapter 2 Estimates of volcanic mercury emissions from Redoubt Volcano, Augustine Volcano, and Mt. Spurr eruption ash[1]

2.1 Introduction

Mercury (Hg) is a volatile and toxic metal released to the environment by both natural and anthropogenic sources. Volcanoes are considered to be one of the largest primary natural sources of Hg, with previous estimates of total annual volcanic Hg emissions between ~50–700 t a^{-1} (e.g., Nriagu and Becker, 2003; Pyle and Mather, 2003). However, large uncertainties exist in speciation, reaction pathways, total emission to the atmosphere, and the ultimate fate of volcanic Hg in the environment (see Figure 1 in Edwards et al., 2021, for a schematic of Hg chemistry in volcanic environments).

Despite these uncertainties, volcanic sources are measured to release prodigious quantities of Hg to the atmosphere as Gaseous Elemental Mercury (GEM; Hg^0, Bagnato et al., 2015). Oxidation of GEM to Gaseous Oxidized Mercury (GOM; Hg^{2+}) and subsequent uptake in the form of Particulate-Bound Mercury (PBM; generally Hg^{2+}) is the principal pathway for atmospheric removal of volcanic Hg emissions (Driscoll et al., 2013). GEM is relatively insoluble in water and has an atmospheric lifetime of ~3 months under standard tropospheric conditions, theoretically allowing for long-distance transport (Horowitz et al., 2017). However, modeling has suggested that conditions within volcanic plumes, including the presence of halogen species, may facilitate rapid oxidation of > 80% of volcanically-sourced GEM to PBM within minutes of emission (von Glasow, 2010). These model results are supported by field observations, which found depletion of GEM emitted from volcanic features on the order of minutes (Aiuppa et al., 2007). Empirical attempts to constrain speciation of emitted volcanic Hg have also been performed up to hundreds of meters from emission sources in ash-poor plumes, and have found PBM to represent anywhere from low (1–5%; Bagnato et al., 2007; Witt et al., 2008; Mather et al., 2012) to high (40–90%; Zambardi et al., 2009) proportions of Total Hg (THg) emitted to the atmosphere. These observations suggest that oxidation of GEM and subsequent removal through wet or dry deposition may be more efficient, albeit variable, under certain conditions in volcanic plumes than in the background atmosphere.

The main sources of uncertainty in the speciation and total emission of volcanic Hg are rooted in a lack of measurements from volcanic eruptions, due to the logistical challenges of collecting gaseous Hg samples from actively erupting plumes. Therefore, nearly all existing studies (summarized in Bagnato et al., 2015 and Edwards et al., 2021) have focused on volcanic Hg emissions from quiescent persistently degassing volcanoes. Scrubbing of emitted metals from volcanic plumes occurs through particle surface

[1] Kushner, D.S., Lopez, T.M., Wallace, K.L., Damby, D.E., Kern, C., and Cameron, C.E. (2023). Estimates of volcanic mercury emissions from Redoubt Volcano, Augustine Volcano, and Mount Spurr eruption ash.

adsorption and acid aerosol formation (Ayris and Delmelle, 2012; Ilyinskaya et al., 2021), though little analytical work has been performed to constrain the extent of these processes with respect to Hg and in particular the role of the substrate on Hg adsorption (Stewart et al., 2020). One potential method to better characterize volcanic Hg speciation during eruption and to better quantify total volcanic Hg emissions is through the analysis of PBM adsorbed to the surface of volcanic ash particles, which can readily be sampled on the ground downwind of eruptions. For this approach, we presume that Hg in our samples is present on ash surfaces and that Hg in our ash deposits is synonymous with PBM, though we recognize there may be other modes of co-deposition including wet deposition through dissolution into condensed aqueous phases (Lindberg and Stratton, 1998).

Herein, we analyze Hg concentrations on 227 bulk ash samples to investigate how PBM concentration varies (1) with distance from the source, (2) between distinct events within the same eruption, and (3) between different volcanoes. We then apply a new approach to estimate Hg emissions from the target eruptions, whereby we integrate our Hg-ash data with previous mass estimates of total erupted ash. We consider our estimates to be minimums because they do not account for the unconstrained abundance of Hg that remains in the atmosphere down-plume, which can still be measurable over thousands of kilometers (Babu et al., 2022).

These points of investigation provide an eruption-scale understanding of Hg, from emission to in-plume reactions and removal/deposition. First, PBM concentration variation with distance is used to constrain the timing of GEM oxidation and adsorption as the plume travels downwind, which is wholly unconstrained for ash-rich plumes. Sustained oxidation-adsorption of GEM to PBM may result in increasing concentrations of PBM as the ash-rich plume travels downwind so long as GEM abundance does not become rate limiting, whereas rapid formation of PBM would favor no discernable increase of PBM with distance on the km scale investigated here. Second, PBM concentration variation between distinct events is used to investigate potential Hg variability over the eruption duration, which is also unconstrained at present. Variations in Hg concentration throughout the eruptive sequence may be a function of Hg solubility in magma. For example, if Hg readily exsolves from magma at depth, Hg may accumulate in a pre-eruptive exsolved volatile phase and therefore be preferentially released early in the eruption and subsequently absorbed on ash (Varekamp and Buseck, 1986). In contrast, if Hg is relatively soluble in magma it may degas upon surface eruption and exhibit no obvious temporal trend in concentration over the eruption duration. Finally, differences in PBM concentration in ash samples from the target volcanoes are used to investigate variability in Hg emissions across volcanoes and eruption cycles. Differences in PBM concentration between the target volcanoes may reflect different Hg concentrations in source magmas or may result from different oxidative potentials in the eruption plumes. Variance in Hg concentration within source magmas may be due to the relative mantle, slab, and crustal

contribution where the mantle is recognized as Hg-poor relative to the crust and slab (Canil et al., 2015; Wedepohl, 1995).

We focus on three recent and well-characterized eruptions from Mt. Spurr (1992), Redoubt (2009), and Augustine (2006) volcanoes, Alaska. Volcanic ash samples from these eruptions were readily available for analysis from the Alaska Volcano Observatory (AVO) and have well-characterized corresponding eruption mass estimates to address our proposed questions. Through this work we provide new constraints on the amount of PBM from these three target eruptions and discuss possible implications of our findings on global volcanic Hg budgets. Our data provide a first estimate of mercury input into the local environment for the areas impacted by our target eruptions, and can be used to refine mercury cycling in the region.

2.2 Eruptive history

We target three volcanoes within Alaska (Figure 2.1A) that have undergone explosive volcanic eruptions within the past three decades. These volcanoes were selected on the basis of their well-characterized recent eruptions, production of significant ash clouds, and the spatially and temporally extensive sampling of volcanic ash rapidly following the eruptive events by AVO scientists. From east to west the target volcanoes (with eruption year in parentheses) are Mt. Spurr (1992), Redoubt (2009), and Augustine (2006).

Mt. Spurr (61.2989 N, 152.2539 W; 3374 MASL) is an andesitic to dacitic stratovolcano with recent eruptions in 1953 and 1992 (Miller et al., 1998). The 1992 eruption had a Volcanic Explosivity Index (VEI) of 3 (0.1–0.01 km^3 erupted tephra; Newhall and Self, 1982) and consisted of three distinct subplinian explosive events on June 27, August 18, and September 16-17, with the largest event (August 18) producing a plume that reached 15 km above sea level (ASL; Eichelberger et al., 1995). In total, the eruption is estimated to have produced 106×10^9 kg of cumulative tephra and ~830 kt SO_2 (Eichelberger et al., 1995; McGimsey et al., 2001).

Redoubt Volcano (60.4852 N, 152.7438 W; 3108 MASL) is an andesitic stratovolcano with recent eruptions in 1966, 1967, 1989–90, and 2009 (Miller et al., 1998; Wallace et al., 2013). The 2009 VEI 3 eruption consisted of 19 distinct explosive events between March and April, followed by extrusion of lava domes. In total, the eruption is estimated to have had a maximum plume altitude of 19 km ASL, produced 55×10^9 kg of tephra and 1270 kt SO_2, and dispersed ash over an 80,000 km^2 region (Werner et al., 2013; Wallace et al., 2013).

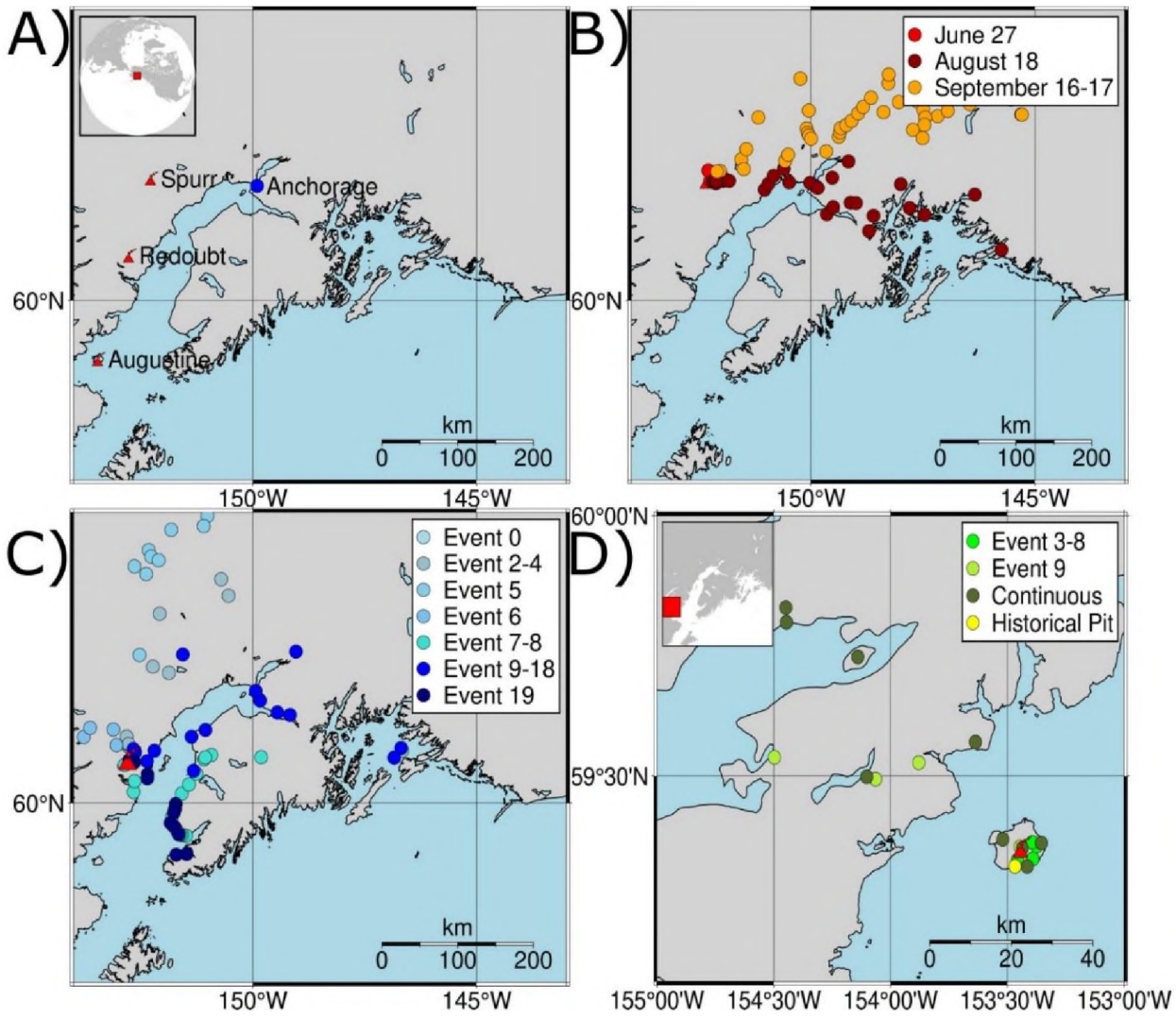

Figure 2.1 (A) Location of studied volcanoes with sample collection location for (B) Mt. Spurr (1992), (C) Redoubt (2009), and (D) Augustine (2006). Distinct eruptive events are color coded in the inset.

Augustine Volcano (59.3629 N, 153.435 W; 1260 MASL) is an andesitic to dacitic stratovolcano with recent eruptions in 1963, 1976, 1986, and 2006 (Miller et al., 1998; Wallace et al., 2010). The 2006 VEI 3 eruption consisted of 13 distinct explosive events and effusive phases between January and March (Wallace et al., 2010). In total, the eruption is estimated to have had a maximum plume altitude of 13.5 km ASL, produced 22×10^9 kg of tephra and 630 kt SO_2, and dispersed ash up to 185 km away (McGee et al., 2010; Wallace et al., 2010).

2.3 Methods

2.3.1 Ash samples

A subset of ash samples from the target eruptions was selected based on their spatial coverage of discrete explosive events. Specifically, we targeted events that had estimates of total ash-mass and included samples that were deposited at various down-wind distances from the vent and collected no more than a week after deposition. Collection notes were used to exclude samples that may have been contaminated, such as the sample being near an industrial area or possibly containing non-representative material. We also aimed to collect samples from a minimum of 3 events per eruption spanning the beginning, middle, and end of the eruption. Bulk ash samples previously collected for mass per unit area analysis (full sample list, collection procedure, and processing details for each eruption are detailed in McGimsey et al., 2001; Wallace et al., 2010; Wallace et al., 2013) were queried from the Geologic Database of Information on Volcanoes in Alaska (GeoDIVA; Cameron, 2004). In total, 227 samples were selected: 84 from Mt. Spurr (1992), 114 from Redoubt (2009), and 29 from Augustine (2006). Outside the immediate scope of our hypotheses but of additional interest are 4 historic samples collected from a pit on Augustine. All samples were bagged and stored in boxes on large shelving units in an area removed from sunlight at the Geologic Materials Center or the U.S. Geological Survey (USGS) tephra labs in Anchorage, Alaska. Grain sizes of the bulk material was not used a determinant in subsampling but samples represent a mixture of extremely fine ash to lapilli (detailed particle size distributions are presented in McGimsey et al., 2001; Wallace et al., 2010; Wallace et al., 2013). It is assumed for the purpose of this study that no Hg has been lost or gained under these storage conditions. Ash masses of 0.1–5.0 g per sample were subsampled from the repositories using sterile instruments.

2.3.2 Hg concentration analysis of ash samples

Bulk volcanic tephra subsamples were freeze-dried and analyzed for THg via direct combustion using Atomic Absorption Spectroscopy (AAS) on a Milestone DMA-80 instrument (Milestone Srl, Italy) following the United States Environmental Protection Agency (U.S. EPA) Method 7473 (U.S. EPA, 1998) in the Marine Ecotoxicology and Trophic Assessment Laboratory at the University of Alaska Fairbanks. All samples (weights 0.01-0.1 g) were heated to 800 °C and analyzed at least in duplicate with a precision range of ± 10%, apart from 15 limited quantity samples on which singlicate analysis was conducted. Calibration curves were prepared using an internal liquid standard to a 0.5 ng Hg limit of quantification. Accuracy checks were routinely performed after analysis of 20 samples using two internal standards (10 ppb, 100 ppb) and a National Institute of Standards and Technology Standard Reference Material (NIST SRM 1633c – Trace Elements in Coal Fly Ash; certified value: 1005 ± 22 ng g^{-1}). The values of these standards were determined by our AAS analyses to be 93.9 ± 3.1 ng g^{-1} (n = 39) for the 100 ppb liquid

standard, 9.8 ± 1.0 ng g^{-1} (n = 52) for the 10 ppb liquid standard, and 1017.9 ± 31.8 ng g^{-1} (n = 55) for NIST SRM 1633c.

Ash samples are assumed in this study to have no Hg adsorbed onto the surface at the time of fragmentation and ejection from the vent. In-plume Hg concentration at the time of all three eruptions was not measured, but assumed from GEM measurements of other volcanic systems (Bagnato et al., 2015) to be 2–3 orders of magnitude larger than the modeled ambient atmospheric concentration of ~1.5 ng m^{-3} for this area (Zhang and Zhang, 2022).

2.3.3 Variable classification and statistical approach

In this study, we test the following three hypotheses: (1) there is a significant dependence of bulk ash Hg concentration from individual eruption events on the distance of the sampling location from the source vent; (2) there is a significant difference in bulk ash Hg concentration between eruption events; and (3) there is a significant difference in bulk ash Hg concentration between volcanoes.

Data were categorized by volcano of origin, event number within each eruption sequence, and distance from the vent. Eruption events were grouped together in cases where sample collection did not allow for discrimination to specific events (e.g., Redoubt events 7–8). Eruption chronology, definitions, groupings of eruption events, and eruption mass estimates were defined or calculated in Wallace et al. (2013) for the 2009 Redoubt eruption, Wallace et al. (2010) for the 2006 Augustine eruption, and McGimsey et al. (2001) for the 1992 Mt. Spurr eruption. The distance of each ash sample from the vent was determined using the collected GPS coordinates and the eruptive vent coordinates as defined by the AVO. More details on the samples used can be found in the supplementary materials.

We use multivariable linear regression using the R stats package (R core team, 2013; supplementary materials) to test the relationships among the three factors (sampling distance, eruption event, volcano of origin) on Hg concentration in our ash samples. This statistical test was identified as the most appropriate due to our dataset including multiple independent variables. This method assumes a normally distributed sample population, which was confirmed for our sample sets through a Kolmogorov-Smirnov Normality Test for Mt. Spurr ($p = 0.22$), Redoubt ($p = 0.07$), and Augustine ($p = 0.12$). Testing of statistical significance was conducted in four separate linear regression model runs: the first three considered the influence of distance and eruption event on Hg concentration for each of the three volcanoes, and the fourth looked at the influence of volcano of origin on Hg concentration. For this fourth test, we combined all Hg concentration data per volcano so that it is independent of eruption event and distance. Following our calculations, we apply a P value threshold to determine whether each of our factors influence Hg concentration, where $p > 0.05$ indicates that factor does not exert a statistically significant influence on our sample set. Significance is only considered for sample sets of $n \geq 5$. We also

calculate descriptive statistics for the measured Hg concentration per sample for each volcano and event, including mean, standard deviation, and quartiles.

2.4 Results

2.4.1 Mt. Spurr (1992)

The largest number of samples analyzed in this study were from Mt. Spurr's two most well-documented events (Figure 2.2A) on 18 August (n = 33) and 16–17 September (n = 49), with samples distributed fairly evenly over the total distance collected (5–378 km). Associated p-values (Table 2.1) show no significant difference in sample Hg concentration with distance or among events. The 27 June event had a small sample size (n = 2) of only proximal samples and data are plotted but not examined statistically. The mean Hg concentration for all Mt. Spurr samples is 77.6 ± 48.7 ng g^{-1} (range: 19–338 ng g^{-1}), which is the highest mean Hg concentration measured for the three target volcanoes (Table 2.1).

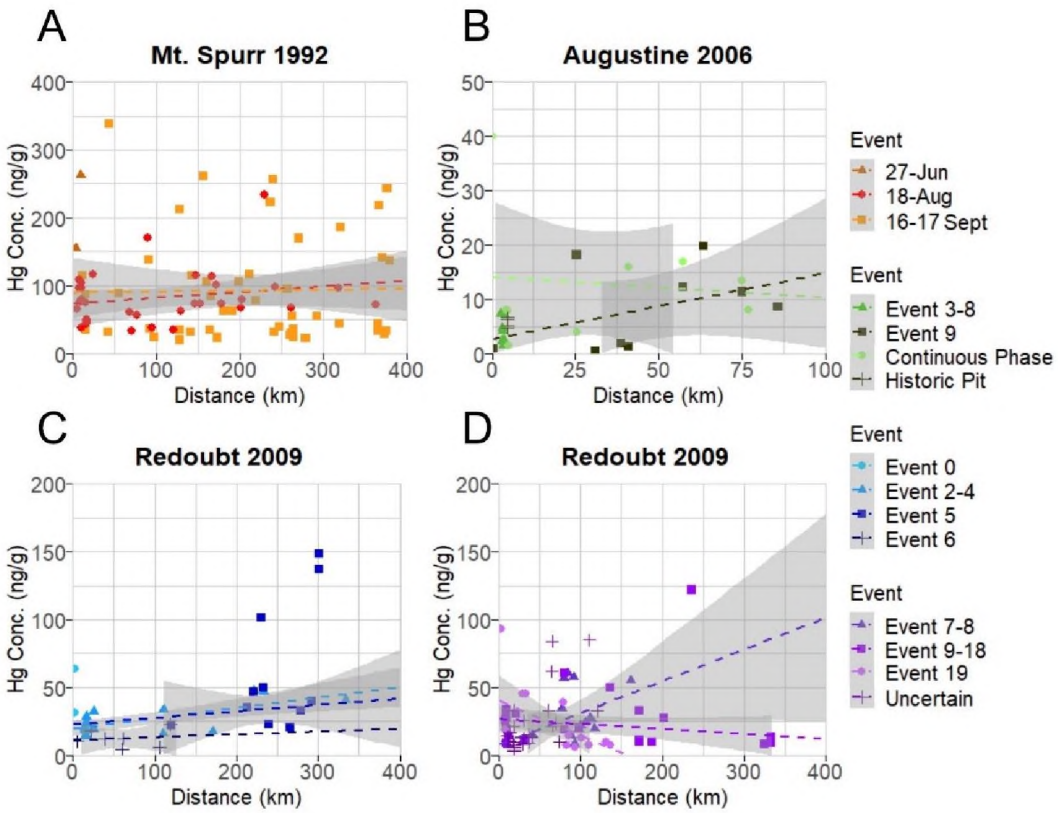

Figure 2.2 Plot of Hg concentration measured as PBM on volcanic ash versus distance for individual events within (A) Mt. Spurr, (B) Augustine, and (C and D) Redoubt (separated to avoid plot crowding) eruptions. Dashed lines are linear model fits used in determining significance and grey shaded areas are 95% confidence intervals. Note the high variance in measured PBM for each eruptive event and occurrence of sample Hg concentrations plotting outside 95% confidence interval regions indicating no significant relationship between Hg concentration and distance for these events.

Table 2.1 Descriptive statistics of analyzed Mt. Spurr, Redoubt, and Augustine ash. Concentration data are presented as ng g^{-1}

Volcano	*n*	Hg Concentration Mean ± SD	Hg Quartiles (25%, 75%)	Regression p-value
Mt. Spurr 1992	**77**	**77.6 ± 48.7**	**37.5, 114.5**	**0.08[a], 0.24[b]**
June 27	1	155.3	NA	
Aug 18	32	77.7 ± 29.9	59.6, 97.0	
Sept 16–17	44	75.7 ± 58.4	32.0, 108.3	
Redoubt 2009	**107**	**22.8 ± 15.1**	**11.0, 33.2**	**0.09[a], 0.61[b]**
Event 0	2	47.6 ± 23.1	39.4, 55.7	
Events 2–4	16	26.6 ± 11.0	18.4, 32.7	
Event 5	8	33.8 ± 11.3	22.9, 41.6	
Event 6	7	12.4 ± 6.4	8.1, 15.3	
Events 7–8	17	27.7 ± 18.6	14.4, 34.6	
Events 9–18	20	22.3 ± 14.3	11.1, 28.6	
Event 19	11	19.6 ± 15.9	7.7, 29.3	
Uncertain	26	16.6 ± 12.9	8.6, 21.7	
Augustine 2006	**25**	**7.2 ± 6.0**	**1.9, 12.0**	**0.22[a], 0.68[b]**
Events 3–8	8	3.9 ± 2.4	2.1, 5.3	
Event 9	8	8.3 ± 7.6	1.2, 12.2	
Continuous Phase	9	9.5 ± 5.5	6.8, 14.0	
Historic Pit	*4*	*5.7 ± 0.9*	*5.0, 6.4*	
All Volcanoes	**209**	**NA**	**NA**	**2.2×10^{-16} [c]**

[a]p-value for event; [b]p-value for distance; [c]p-value between volcanoes

2.4.2 Augustine (2006)

The 2006 Augustine eruption had the smallest sample set analyzed (n = 25) of all three target volcanoes owing to the volcano's location on an island, with most ashfall deposited into the ocean. Samples for this volcano were also more limited in spatial coverage than the other two, covering distances of 1–85 km from the vent, and were split between events 3–8, 9, and a continuous phase (Figure 2.2B). All samples for events 3–8 were collected from the island and only cover a distance gradient of 2–3 km from source, while event 9 and continuous phase sample coverage include island and mainland Alaska coverage (Figure 2.1D). Samples from the continuous phase and event 9 show no significant difference between event groups or distance. Of additional interest are 4 historic samples collected from a pit on

Augustine that have similarly low Hg concentrations (Table 2.1; Figure 2.3). The mean Hg concentration for all Augustine samples is 7.2 ± 6.0 ng g^{-1} (range: 0.5–40 ng g^{-1}), which is the lowest mean Hg concentration measured for the three target volcanoes (Table 2.1).

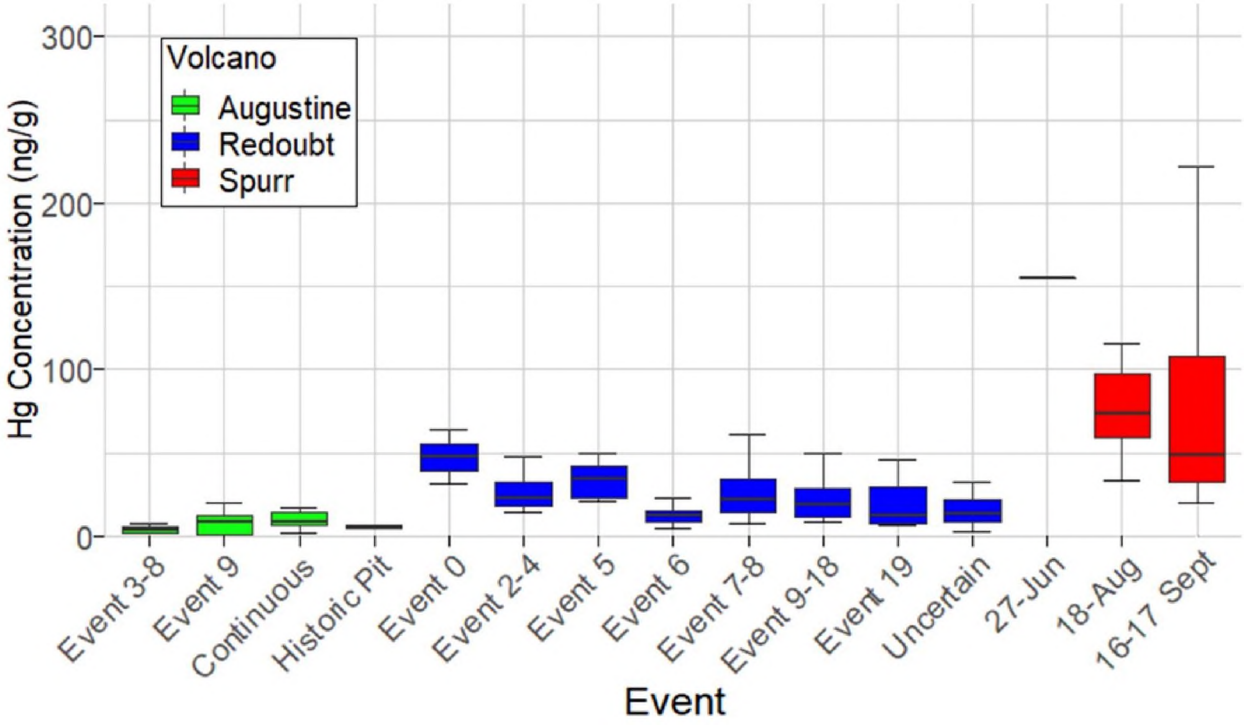

Figure 2.3 Box plot of sample Hg concentration measured as PBM on volcanic ash for individual events within Augustine (green), Redoubt (blue), and Mt. Spurr (red) eruptions showing median Hg concentration (thick lines), interquartile ranges (colored boxes), and minimum/maximum values (horizontal caps).

2.4.3 Redoubt (2009)

The dataset for Redoubt comprises samples subdivided into three composite event groupings (events 2-4, 7–8, 9–18) and discrete events within the 2009 eruption sequence (Figures 2.2C, 2.2D). The full sample distribution covers 3–333 km, however some individual event groupings have limited spatial coverage (e.g., event 5 covers 120–301 km and event 6 covers 5–119 km). No statistically significant difference in Hg concentration is seen between event grouping or distance from source (Table 2.1; Figures 2.2C, 2.2D). Samples from eruption event 0 and those with uncertain event origins were excluded from variance analysis due to either the small sample size or unknown event origin. The mean Hg concentration for all Redoubt samples is 22.8 ± 15.1 ng g^{-1} (range: 3.6–148 ng g^{-1}) (Table 2.1).

2.4.4 Total particulate-bound Hg from the target eruptions

A linear regression model fit to data from all three volcanoes finds a significant difference in Hg concentration in ash among these three volcanoes ($p = 2.2 \times 10^{-16}$; Table 2.1). Thus, for the three volcanoes considered here, there is no statistical difference in Hg concentration by distance or eruptive event, however there is a statistical difference in Hg concentration by volcano of origin. On this basis, all samples from an individual volcano may be grouped together irrespective of distance or eruptive event (Figure 2.4A), simplifying methods to estimate the total PBM emission from each volcano (Figure 2.4B).

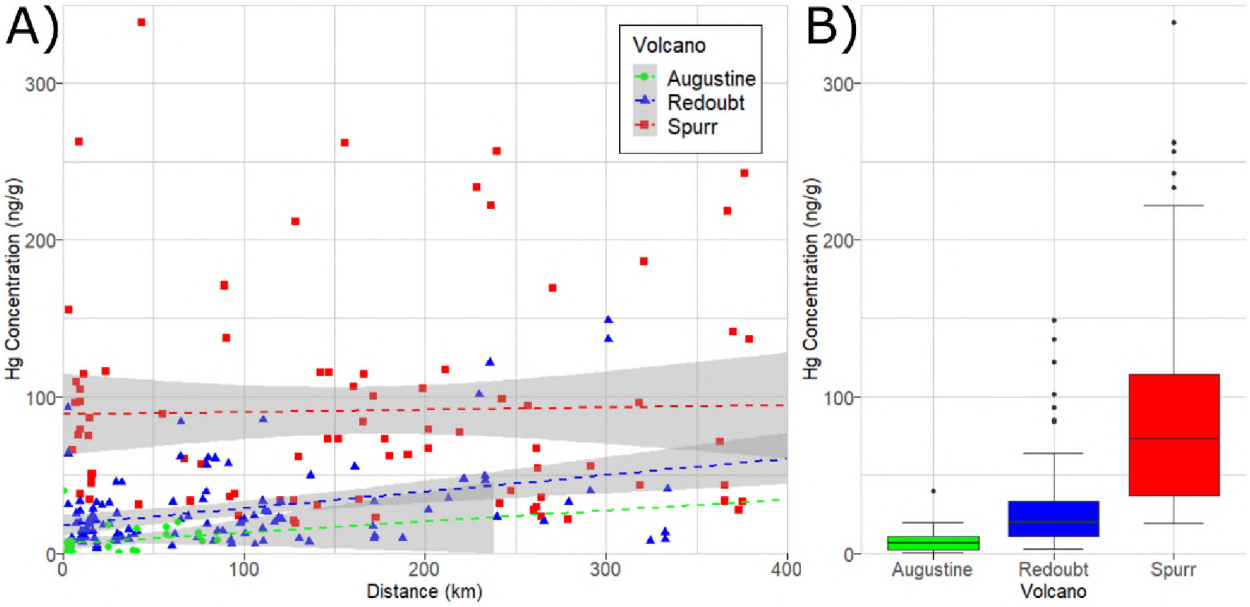

Figure 2.4 Hg concentration measured as PBM on volcanic ash from Spurr (1992), Redoubt (2009) and Augustine (2006) volcanic eruptions in Alaska. (A) PBM on ash as a function of ash deposition distance from the eruption vent, with dashed lines showing linear regressions. Note the high variance in measured PBM for each eruption and occurrence of sample Hg concentrations plotting outside gray (95% confidence interval) regions indicating no significant relationship between Hg concentration and distance for these eruptions. (B) Box plot showing the observed difference in median Hg concentration (thick lines), interquartile ranges (colored boxes), minimum/maximum values (horizontal caps), and outliers (black circles).

We calculate the total PBM in the tephra deposit from each target eruption by multiplying existing total eruption ash mass estimates by the mean Hg concentration of our bulk ash samples. We infer this to provide a minimum estimate of total Hg emissions for these eruptions, as we do not account for remaining GEM or unbound Hg^{2+} within the volcanic plume. The resulting Hg emissions (as PBM) per volcanic eruption are shown in Table 2.2.

Table 2.2 Total particulate-bound Hg from each volcano

Volcano	Eruption Mass ($\times 10^9$ kg)	Mean Hg Conc. (ng g^{-1})	Emitted PBM (t)
Mt. Spurr 1992	106.0[a]	77.6	8.23
Redoubt 2009	54.7[b]	22.8	1.25
Augustine 2006	21.7[c]	7.2	0.16

Total erupted tephra mass from [a]McGimsey et al., 2001; [b]Wallace et al., 2013; [c]Wallace et al., 2010

2.5 Discussion

2.5.1 Mercury variation with distance from vent

Our results find no significant difference in Hg concentration on volcanic ash based on downwind distance, at least on the scale of 1-500 km downwind distances investigated here. Volatile trace metals (e.g., Cu, Cd, Pb) have been shown to partition strongly into non-silicate particulate matter and preferentially deposit proximally (Ilyinskaya et al., 2021). It has also been suggested that volcanic plumes may provide a medium to rapidly oxidize entrained atmospheric GEM within minutes (von Glasow, 2010) which would lead to PBM as the dominant Hg species within the nearer distances considered for this study. Alternatively, the more distal samples from both Mt. Spurr and Redoubt contain higher proportions of fine ash material than proximal samples (McGimsey et al., 2001; Wallace et al., 2013), providing a correspondingly higher surface area for adsorption reactions to take place (Ermolin et al., 2018; 2021) which would favor higher bulk-sample concentrations of PBM. Despite these pathways potentially favoring a decrease or increase of PBM with distance, respectively, neither process appears to be discernible within the variability of our samples. Though there is large variability (>50%) in the PBM concentration of ash between these volcanic sources, the absence of a correlation with either downwind distance or eruptive event suggests that either substantial GEM oxidation happened before deposition at our closest sampling sites (~1-5 km) and any further in-plume oxidation is not distinguishable within the sample variability, or that the GEM oxidation process is much slower than the timescales on which ash dispersion and sampling are occurring (minutes to hours) and thus cannot be identified in this dataset. We consider the first explanation to be the more likely one. The most proximal samples from both Redoubt and Mt. Spurr were collected at ~5 km downwind, corresponding to plume transport times exceeding 10 minutes, which would still allow for the rapid oxidation processes proposed by von Glasow (2010) and be consistent with other findings of elevated PBM in proximal ash from Marumoto et al. (2017) or elevated Hg in soils and lichens from select volcanic areas (Catán et al., 2020), which are interpreted to result from very near-vent deposition and uptake. Previous studies which have attempted to constrain the speciation of Hg within volcanic plumes have all been performed on much shorter spatial scales – within hundreds of meters of the vent – such that rapid oxidation of GEM may occur, but the extent is not captured on the 1–500 km scale of existing studies (Witt et al., 2008; Bagnato et al., 2015). If oxidation is occurring on

much slower timescales than represented in this dataset our study would represent an underestimation of erupted PBM; however, this is unlikely as we detect oxidized Hg on all of our studied ash samples, indicating that this process has taken place.

Based on our findings, we suggest that bulk samples for determining average volcanic PBM may be sourced from downwind distances ranging from 1–500 km, as it is likely that by those distances most GEM has either been oxidized and scrubbed by ash or aerosols or is no longer being efficiently adsorbed due to significant plume dilution with background air. However, the variation seen within each sample set suggests that accurate characterization of Hg present in the ash of a single volcano should not be based on small sample sizes. A good illustration of this is presented in our Hg concentrations for Redoubt, which are higher than previously reported for a single sample of the same Redoubt eruption (Coufalík et al., 2018; Table 2.3).

2.5.2 Mercury variation across volcanoes

We find a significant difference in PBM concentrations on ash between eruptions from our three target volcanoes. This suggests that Hg concentration may be controlled in part by either volcanic source conditions or by conditions within the volcanic plume that promote or hinder adsorption of Hg after release from the vent.

Different initial concentrations of Hg emanating from the volcanoes, reflecting a source control, would lead to different quantities of GEM being available for oxidation and adsorption. Specifically, volcanoes with Hg-poor plumes would have less available Hg, and ash samples from these volcanoes would therefore be expected to contain less PBM. Wide arrays of measurements from passively degassing volcanic environments (summarized in Bagnato et al., 2015 and Edwards et al., 2021) show orders of magnitude differences of GEM within volcanic plumes at downwind distances within ~1 km of the vent, ranging from near ambient (4 ng m^{-3}) at Gorely (Russia) and Poás (Costa Rica) volcanoes to orders of magnitude higher (373 ng m^{-3}) at Nyiragongo (Democratic Republic of the Congo) volcano. A compilation of literature values for PBM on volcanic ash (Table 2.3) shows similar orders-of-magnitude differences between volcanic sources as we have found here. This suggests that the notable variations in Hg concentration on deposited ash seen in our study and globally may be attributable to variable (comparatively high and low) Hg emissions by source, which could result from large-scale variations in the source of Hg incorporated into magma. A significant difference in Hg concentration by source (different volcanoes and geologic settings) would mechanistically account for the variation between Hg in ash samples and GEM concentrations in volcanic plumes.

Table 2.3 Literature values of PBM in volcanic ash

Volcano	Eruption Year	Hg concentration (ng g^{-1})	Reference	Analytical Method
Mt. Spurr	1992	77.6	This work	AAS
Augustine	2006	22.8	This work	AAS
Redoubt	2009	7.2	This work	AAS
Redoubt	2009	6	Coufalik et al. (2018)	AAS
Eyjafjallajökull	2010	0.3	Coufalik et al. (2018)	AAS
Sakurajima	1985	11 - 80	Ohki et al. (2016)	AAS
Sakurajima	2010	6 - 66	Ohki et al. (2016)	AAS
Aso (magmatic)	2014 - 2015	1 - 4	Marumoto et al. (2017)	AAS
Aso (phreatic)	2015 - 2016	145 - 354	Marumoto et al. (2017)	AAS
Kilauea	2018	37 - 180	Damby et al. (2022)	AAS
Etna	2001	3 - 16	Stracquadanio et al. (2003)	CVAFS
Tolbachik	2012	70 - 73	Ermolin et al. (2018; 2021)	ICP-MS
Tolbachik Fissure Eruption	1975-76	23	Ermolin et al. (2021)	ICP-MS
Klyuchevskoy	2015	75 - 80	Ermolin et al. (2018; 2021)	ICP-MS
Puyehue	2011	<8	Ermolin et al. (2018)	ICP-MS
Kizimen	2010	10	Ermolin et al. (2021)	ICP-MS
Shiveluch	2010	<3	Ermolin et al. (2021)	ICP-MS
Copahue	2000	7 - 22	Smichowski et al. (2003)	ICP-MS

The lack of distinction among events at all three volcanoes in this study suggests that Hg emissions are consistent throughout an eruptive sequence and potentially across multiple eruptive episodes. Despite variability of major gas species during an eruptive sequence (Werner et al., 2013), a consistent abundance of Hg throughout each of the examined eruptions is supported by similar PBM concentration on ash. The undated ash samples collected from a historical pit at Augustine (Table 2.1) were also found to have similar Hg concentrations as the 2006 eruption, suggesting that Augustine's low-Hg emissions have persisted across multiple eruption cycles. Similarly, ash samples collected and analyzed for PBM from two eruptions from Sakurajima volcano (Japan, 1985 and 2010; Ohki et al., 2016) were found to be within the same range, further supporting this idea. Conversely, two sets of proximal samples from Aso volcano (Japan, Marumoto et al., 2017) collected during phreatic and magmatic (strombolian) eruptions were found to have PBM concentrations that differed by two orders of magnitude

(Table 2.3). Marumoto et al. (2017) propose that the orders-of-magnitude difference in PBM concentrations may be attributable to different eruption styles. If an eruption is sourced from low-Hg magma, it is not surprising that phreatic eruptions (i.e., eruptions that do not erupt juvenile material) would have higher quantities of emitted Hg than magmatic eruptions for the same volcano. Some crater lakes such as the one overlying Mt. Ruapehu have been measured to contain high concentrations of Hg (Deely and Sheppard, 1996) signifying there may also be potential for Hg contribution from hydrothermal systems in phreatic eruptions. Therefore, while our findings together with the literature suggest that volcanoes may be characteristically high- or low-Hg emitters, even over multiple eruption cycles, it is possible that Hg emissions can vary substantially for different eruption styles at the same volcano.

Certain physical or chemical conditions within the volcanic plume could facilitate adsorption of Hg on ash particles, which include: 1) the presence of gaseous species facilitating GEM oxidation (e.g., halogens, ozone); 2) a large quantity of aerosols which would increase the surface area for uptake; 3) the availability of sunlight at the eruption time (Amos et al., 2012; von Glasow, 2010). Rapid ozone depletion and formation of BrO have been measured in Redoubt's plume (Kelly et al., 2013), which may indicate that conditions favorable to the oxidation of GEM were sustained for this and potentially other eruptions. Comparable measurements at Mt. Spurr and Augustine are not available, but previous studies have found different BrO concentrations in volcanic plumes at other volcanoes (Bobrowski et al., 2015), and the variation in PBM from our study sites could in part be controlled by the availability of reactive species. Photolytic conditions between our studied volcanoes may be extrapolated by the timing of eruptions and resulting availability of solar radiation. Specifically, Mt. Spurr erupted in a period of high solar radiation (June–September), while Augustine (January–February) and Redoubt (March–April) both erupted during periods of lower solar radiation. Events within each of the studied eruptive sequences include both day and nighttime-only events with no discernable difference in PBM noted at equivalent downwind distances, so it is unlikely that variations in solar radiation had a significant effect on our samples. As an example, the Mt. Spurr eruption contains two well documented events (McGimsey et al., 2001) during daytime (August 18, ~7:00 PM eruption) and nighttime (September 16-17; 1:00 AM eruption), but the Hg concentrations measured in downwind samples are not distinguishable from each other. It is also unlikely that the geographic location played a primary role in the observed variation in Hg concentration, as all three eruptions had similar Volcanic Explosivity Index (~3–4), plume altitudes (13–19 km), and occurred at similar latitudes (~60°N).

A geologic mechanism that could explain initial Hg concentration differences across volcanoes would be related to heterogeneous distribution of Hg within the crust or subducting slab. The mantle is measured to be Hg-poor relative to crustal material (Canil et al., 2015; Wedepohl, 1995), so magma derived primarily from the mantle (e.g., hotspot volcanoes) would be Hg-poor compared to those which

have incorporated more material from a dehydrating subducted oceanic slab or crust (arc volcanoes). Similar metal-rich or metal-poor signatures have been measured between arc and non-arc volcanoes (Edmonds et al., 2018; Edwards et al., 2021), and crustal incorporation as a source of volcanic Hg has previously been proposed (Coufalík et al., 2018). Records of ascending Hg-rich fluids are preserved in regions of subduction of oceanic sediments underneath continental crust as economically significant Hg mineral deposits, which typically occur in low-temperature environments where numerous deposits may be dispersed over a wide region (Rytuba, 2003). Therefore, Hg-rich volcanoes could be explained by either the direct recycling of Hg-rich fluids sourced from subducted sediments to arc volcanoes, or by the assimilation of Hg-rich crust during magma storage and ascent. We note that the volcanoes in this study which contain higher concentrations of PBM (Mt. Spurr and Redoubt) are built upon thicker sections of crust (Zhang et al., 2019), including lithologies containing high proportions of evolved granitoids and terrestrial sediments (Wilson et al., 2015).

Differing source controls on the quantity and concentration of Hg emitted from volcanic sources would also lead to environmental implications. Levels of Hg in Alaska marine mammals have been found to exhibit spatial variability which is not entirely accounted for by anthropogenic sources, suggesting in part a natural source (Ricca et al., 2008; Rea et al., 2020). Volcanoes are a likely natural source to explain variability in Hg uptake by marine mammals over both space and time, as individual eruptions will provide Hg input into the local environment. The immediate availability of any PBM deposited through ash for uptake by local flora or fauna is still not well constrained, but minimum estimates of ash masses deposited over well-defined areas presented here provide a starting point for modeling Hg cycling within the local environments downwind from our target volcanoes.

2.5.3 Insights into global volcanic Hg estimates

Different approaches have been used to extrapolate global volcanic Hg estimates over space and time. The two most cited estimates, both of which differentiate between eruptive and persistent degassing contributions, rely on an assumed Hg/SO_2 mass ratio in the gas phase to some extent (Nriagu and Becker, 2003; Pyle and Mather, 2003). Both studies found that eruptive contributions made up approximately half to the majority of annual volcanic Hg emissions. Nriagu and Becker (2003) approximate eruptive THg contributions as 57 t a^{-1} Hg out of a total volcanic Hg flux of 112 t a^{-1} over the two-decade period of 1980-2000 based on the number of days each volcano was in an eruptive phase vs. days on which they were passively degassing. For cases without Hg measurements, they assumed a constant eruptive Hg/SO_2 mass ratio of 1.18×10^{-5}. Similarly, Pyle and Mather (2003) approximate a time-averaged Hg flux for small explosive eruptions of ~500 t a^{-1} Hg (60–2000 t a^{-1} Hg range) out of a total volcanic Hg flux of ~700 t a^{-1} (80–4000 t a^{-1} Hg range) by assuming an Hg/SO_2 mass ratio range of 1 x 10^{-5}–2×10^{-4} paired with a time-averaged global eruptive SO_2 flux. In both studies, persistently degassing volcanoes are assigned a lower

Hg/SO_2 ratio of 3.18×10^{-8} (Nriagu and Becker, 2003) and 10^{-6}–10^{-4} (Pyle and Mather, 2003) compared to eruptive degassing. While Hg/SO_2 ratios for persistently degassing volcanoes have been quantified (Aiuppa et al., 2007; Bagnato et al., 2015; 2007), no such measurements exist for explosive eruptions. Instead, the higher Hg/SO_2 ratio for explosive volcanism was inferred from volcanically attributed records of increased Hg concentration in peat bogs (Roos-Barraclough et al., 2002) and select eruptions in glacial cores (Schuster et al., 2002). Chronology reassessment of glacial records in Chellman et al. (2017) has questioned the assignment of large Hg depositional events in Schuster et al. (2002) as volcanically sourced, so it is possible that the assumptions underpinning a higher Hg/SO_2 ratio for active explosions in these studies is not uniformly valid. No direct Hg/SO_2 measurements have been collected yet for our target volcanoes in any stage of activity, however we may extrapolate a minimum Hg/SO_2 ratio for our target eruptions given the measured PBM emissions and available SO_2 output provided in the eruptive history section as 9.9×10^{-6} for Mt. Spurr (1992), 9.8×10^{-7} for Redoubt (2009), and 2.5×10^{-7} for Augustine (2006). Though these estimates do not account for unconstrained Hg speciation, they are within the range of Hg/SO_2 ratios measured from open-conduit quiescent degassing in Bagnato et al. (2015).

Our interpretation of high- and low-Hg emitting volcanoes potentially challenges previous assumptions that Hg accounting based on SO_2 emissions may be uniformly applied across all volcanic sources. The global eruptive THg estimate in Nriagu and Becker (2003) is particularly useful for comparison with our study as it includes our three target volcanoes as constituents of the ~57 t a^{-1} Hg average eruptive flux. The 20-year period attributes 2.67 t Hg to Augustine (600 days erupting), 4.73 t Hg to Redoubt (201 days erupting), and 0.71 t Hg to Mt. Spurr (80 days erupting). The 1980-2000 period evaluated for Augustine and Redoubt volcanoes does not encompass our studied eruptions, but their analysis for the Mt. Spurr eruption appears to be solely composed of the 1992 events, and therefore should be directly comparable to our results. If we compare the erupted PBM on ash from the 1992 Mt. Spurr eruption, determined here as ~8.23 t Hg, to the inferred eruptive THg estimate from Nriagu and Becker (2003) of 0.71 t Hg, our results suggest that their eruptive THg emissions are underestimated by at least one order of magnitude, and potentially by more as our study considers only PBM and not other Hg phases. The 21-day duration of the Redoubt 2009 eruption (Wallace et al., 2013) accounts for only ~10% of the 201 total erupted days over the 20-year period analyzed by Nriagu and Becker (2003), yet our eruptive PBM estimate comprises ~25% of their 4.73 t eruptive THg estimate, again suggesting that their eruptive THg estimates may be underestimated. For Augustine, our PBM estimate represents 17 days of explosive-phase plumes (Wallace et al., 2010), or ~3% of the 80-day period used by Nriagu and Becker (2003), yet comprises ~6% of Nriagu and Becker's eruptive THg estimate despite Augustine appearing to be a low-Hg volcano. These discrepancies show that the most cited explosive global Hg estimates (57 t a^{-}

[1], Nriagu and Becker, 2003) are likely too low and may not be appropriately accounting for variations in individual volcanic input. Individual-scale comparisons to other studies which consider only global SO_2 emissions and a fixed Hg/SO_2 ratio are difficult (Pyle and Mather, 2003; Nriagu, 1989).

Given these comparisons, dedicated analysis of globally significant eruptions would be required to confidently provide a minimum global eruptive PBM contribution for a given year. However, each of our target eruptions are cataloged by the Global Volcanic Program (2013) as among the largest eruptions for those years, so we could estimate that the total contribution of PBM to THg from explosive events is on the order of 10–100 t a^{-1} given a typical annual number (<10) of VEI 3 or 4 eruptions with comparable eruption mass to our studied volcanoes. This estimate for PBM is within the same order of magnitude as that of THg by Nriagu and Becker (2003), suggesting that the Nriagu and Becker (2003) is likely underestimated. Our constraints for PBM are on the lower end of the range of THg provided within Pyle and Mather (2003), suggesting that this global estimate is likely more accurate though potentially variable depending on the number of large eruptions each year and volcanic sources. We suggest that, global eruptive contributions of volcanically-sourced PBM could exceed 100 t a^{-1} only in a year with atypically numerous eruptions from lower-Hg volcanoes or a single VEI 5+ eruption from a high-Hg volcano. Expanding on the method presented in this study to analyze ash samples from recent large eruptions with corresponding eruption mass estimates may then allow for more precision to be placed on the upper bounds of our estimate.

2.6 Conclusions

Analysis of Hg adsorbed onto volcanic ash may provide a logistically straightforward and safe collection method to gain insights into Hg emissions from explosive eruptions, including historic eruptions, where syn-eruption campaign measurements and emissions sampling within the volcanic plume is hazardous. Statistical analysis of Hg data from ash samples collected over a wide range of downwind distances and eruptive events from three different explosive volcanic eruptions shows that, despite variability in PBM concentration among samples, there is no significant difference in Hg concentration on ash either between different eruptive events from the same volcano or by distance from the vent. We find that the most determinative factor for PBM concentration is the volcano of origin, with mean PBM concentrations ranging over 3 orders of magnitude among our target volcanoes. This finding suggests that certain volcanoes may be comparatively high- or low-Hg emitters, potentially due to local-regional geologic source controls such as Hg-rich subducted sediments or crust.

We present a new approach for providing minimum constraints on Hg released during volcanic eruptions by integrating our PBM data with prior estimates of erupted ash deposit masses. We calculate total PBM from our target eruptions of 8.23 t Hg, 1.25 t Hg, and 0.156 t Hg for Mt. Spurr (1992), Redoubt (2009), and Augustine (2006) volcanic eruptions, respectively. Our estimates are considered a minimum

because they do not account for the unconstrained abundance of Hg that remains in the atmosphere. Still, our findings for these three volcanoes exceed previous estimates of Hg emissions for individual volcanoes, which has ramifications for estimates of global volcanic Hg emissions.

2.7 Acknowledgements

The authors would like to thank all original collectors of the samples used in this study, especially Game McGimsey, for their rapid eruption responses and the staff of the Geologic Materials Center for diligently curating the samples. We are also grateful to the Marine Ecotoxicology and Trophic Assessment (METAL) lab at UAF for use of their equipment in sample analysis. This work was partially funded through U.S. Geological Survey Cooperative Agreement No. G21AC10384. Any use of trade, firm, or product names is for descriptive purposes only and does not imply endorsement by the U.S. Government.

Supplementary materials to this article can be found online at doi:10.3389/feart.2023.1054521

2.8 References

Aiuppa, A., Bagnato, E., Witt, M.L.I., Mather, T.A., Parello, F., Pyle, D.M., and Martin, R.S. (2007). Real-Time Simultaneous Detection of Volcanic Hg and SO2 at La Fossa Crater, Vulcano (Aeolian Islands, Sicily). *Geophysical Research Letters,* 34(21). doi:10.1029/2007GL030762.

AMAP/UN Environment (2019). Technical Background Report for the Global Mercury Assessment 2018. Arctic Monitoring and Assessment Programme. Oslo, Norway. https://www.amap.no/documents/doc/technical-background-report-for-the-global-mercury-assessment-2018/1815.

Amos, H.M., Jacob, D.J., Holmes, C.D., Fisher, J.A., Wang, Q., Yantosca, R.M., Corbitt, E.S., Galarneau, E., Rutter, A.P., Gustin, M.S., Steffen, A., Schauer, J.J., Graydon, J.A., St. Louis, V.L., Talbot, R.W., Edgerton, E.S., Zhang, Y., and Sunderland, E.M. (2012). Gas-Particle Partitioning of Atmospheric Hg(II) and Its Effect on Global Mercury Deposition. *Atmospheric Chemistry and Physics,* 12(1), 591–603. doi:10.5194/acp-12-591-2012.

Andres, R. J., and Kasgnoc, A.D. (1998). A Time-Averaged Inventory of Subaerial Volcanic Sulfur Emissions. *Journal of Geophysical Research Atmospheres,* 103(D19), 25251–61. doi:10.1029/98JD02091.

Ayris, P.M. and Delmelle, P. (2012). The immediate environmental effects of tephra emission. *Bulletin of Volcanology,* 74, 1905–1936. doi:10.1007/s00445-012-0654-5.

Babu, S.R., Nguyen, L.S.P., Sheu, G.R., Griffith, S.M., Pani, S.K., Huang, H.Y., and Lin, N.H. (2022). Long-range transport of La Soufrière volcanic plume to the western North Pacific: Influence on atmospheric mercury and aerosol properties. *Atmospheric Environment*, 268. doi:10.1016/j.atmosenv.2021.118806.

Bagnato, E., Aiuppa, A., Parello, F., Calabrese, S., D'Alessandro, W., Mather, T.A., McGonigle, A.J.S., Pyle, D.M., and Wängberg, I. (2007). Degassing of Gaseous (Elemental and Reactive) and Particulate Mercury from Mount Etna Volcano (Southern Italy). *Atmospheric Environment*, 41(35), 7377–7388. doi:10.1016/j.atmosenv.2007.05.060.

Bagnato, E., Tamburello, G., Avard, G., Martinez-Cruz, M., Enrico, M., Fu, X., Sprovieri, M., and Sonke, J. E (2015). Mercury Fluxes from Volcanic and Geothermal Sources: An Update. *Geological Society Special Publication,* 410(1), 263–285. doi:10.1144/SP410.2.

Bobrowski, N., von Glasow, R., Giuffrida, G.B., Tedesco, D., Aiuppa, A., Yalire, M., Arellano, S., Johansson, M., and Galle, B. (2015). Gas Emission Strength and Evolution of the Molar Ratio of BrO/SO2 in the Plume of Nyiragongo in Comparison to Etna. *Journal of Geophysical Research: Atmospheres,* 120(1),277–291. doi:10.1002/2013JD021069.

Cameron, Cheryl (2004). The Geologic Database of Information on Volcanoes in Alaska (GeoDIVA): A Comprehensive and Authoritative Source for Volcanic Information. *Alaska GeoSurvey News* 7: 2. doi:10.14509/14592.

Canil, D., Crockford, P.W., Rossin, R., and Telmer, K. (2015). Mercury in Some Arc Crustal Rocks and Mantle Peridotites and Relevance to the Moderately Volatile Element Budget of the Earth. *Chemical Geology,* 396, 134–142. doi:10.1016/j.chemgeo.2014.12.029.

Catán, S.P., Bubach, D., Messuti, M.I., Arribére, M.A., and Guevara, S.R. (2020). Mercury in a Geothermal and Volcanic Area in Patagonia, Southern South America. *Atmospheric Pollution Research,* 11(3),566–573. doi:10.1016/j.apr.2019.12.005.

Chellman, N., McConnell, J.R., Arienzo, M., Pederson, G.T., Aarons, S.M., and Csank, A. (2017). Reassessment of the Upper Fremont Glacier Ice-Core Chronologies by Synchronizing of Ice-Core-Water Isotopes to a Nearby Tree-Ring Chronology. *Environmental Science & Technology*, 51(8), 4230–4238. doi:10.1021/acs.est.6b06574.

Coufalík, P., Krmíček, L., Zvěřina, O., Meszarosová, N., Hladil, J., and Komárek, J. (2018). Model of Mercury Flux Associated with Volcanic Activity. *Bulletin of Environmental Contamination and Toxicology,* 101(5), 549–553. doi:10.1007/s00128-018-2430-5.

Damby, D.E., Bronstein, A.C., Dawrs, S. et al. (2022). Respiratory health hazard of ash from Kīlauea volcano, Hawaii: 2008 Halema'uma'u opening and 2018 summit collapse. *Bulletin of Volcanology*.

Deely, J.M. and Sheppard, D.S. (1996). Whangaehu River, New Zealand: geochemistry of a river discharging from an active crater lake.

Driscoli, C.T., Mason, R.P., Chan, H.M., Jacob, D.J., and Pirrone, N. (2013). Mercury as a global pollutant: sources, pathways, and effects. *Environmental Science and Technology*, 47(10), 4967–4938. doi:10.1021/es305071v.

Edmonds, M., Mather, T.A., and Liu, E.J. (2018). A Distinct Metal Fingerprint in Arc Volcanic Emissions. *Nature Geoscience*, 11(10), 790–794. doi:10.1038/s41561-018-0214-5.

Edwards, B.A., Kushner, D.S., Outridge, P.M., and Wang, F. (2021). Fifty Years of Volcanic Mercury Emission Research: Knowledge Gaps and Future Directions. *Science of The Total Environment,* 757: 143800. doi:10.1016/j.scitotenv.2020.143800.

Eichelberger, J., Keith, T., Miller, T., and Nye, C. (1995). The 1992 Eruptions of Crater Peak Vent, Mount Spurr Volcano, Alaska: Chronology and Summary. *U.S. Geological Survey Bulletin* 2139.

Ermolin, M.S., Fedotov, P.S., Malik, N.A., and Karandashev, V.K. (2018). Nanoparticles of Volcanic Ash as a Carrier for Toxic Elements on the Global Scale. *Chemosphere,* 200, 16–22. doi:10.1016/j.chemosphere.2018.02.089.

Ermolin, M.S., Ivaneev, A.I., Fedyunina, N.N., and Fedotov, P.S. (2021). Nanospeciation of Metals and Metalloids in Volcanic Ash Using Single Particle Inductively Coupled Plasma Mass Spectrometry. *Chemosphere,* 281, 130950. doi:10.1016/j.chemosphere.2021.130950.

Glasow, R. (2010). Atmospheric Chemistry in Volcanic Plumes. *Proceedings of the National Academy of Sciences,* 107(15), 6594–6599. doi:10.1073/pnas.0913164107.

Global Volcanism Program (2013). Volcanoes of the World, v. 4.11.0 (08 Jun 2022). Venzke, E. (ed.). Smithsonian Institution. Downloaded 16 Jun 2022. doi:10.5479/si.GVP.VOTW4-2013.

Halmer, M.M., Schmincke, H.U., and Graf, H.F. (2002). The Annual Volcanic Gas Input into the Atmosphere, in Particular into the Stratosphere: A Global Data Set for the Past 100 Years. *Journal of Volcanology and Geothermal Research,* 115(3), 511–528. doi:10.1016/S0377-0273(01)00318-3.

Horowitz, H.M., Jacob, D.J., Zhang, Y., Dibble, T.S., Slemr, F., Amos, H.M., Schmidt, J.A., Corbitt, E.S., Marais, E.A., and Sunderland, E.M. (2017). A New Mechanism for Atmospheric Mercury Redox Chemistry: Implications for the Global Mercury Budget. *Atmospheric Chemistry and Physics*, 17(10), 6353–6371. doi:10.5194/acp-17-6353-2017.

Ilyinskaya, E., Mason, E. Wieser, P.E., Holland, L., Liu, E.J., Mather, T.A., Edmonds, M., Whitty, R.C.W., Elias, T., Nadeau, P.A., Schneider, D., McQuaid, J.B., Allen, S.E., Harvey, J., Oppenheimer, C., Kern, C., and Damby, D. (2021). Rapid metal pollutant deposition from the volcanic plume of Kīlauea, Hawai'i. *Communications Earth & Environment*. 2, 78. doi:10.1038/s43247-021-00146-2.

Kelly, P.J., Kern, C., Roberts, T.J., Lopez, T.M., Werner, C., and Aiuppa, A. (2013). Rapid Chemical Evolution of Tropospheric Volcanic Emissions from Redoubt Volcano, Alaska, Based on Observations of Ozone and Halogen-Containing Gases. *Journal of Volcanology and Geothermal Research,* 259, 317–333. doi:10.1016/j.jvolgeores.2012.04.023.

Lindberg, S.E. and Stratton, W.J. (1998). Atmospheric Mercury Speciation: Concentrations and Behavior of Reactive Gaseous Mercury in Ambient Air. *Environmental Science & Technology,* 1(32). doi:10.1021/es970546u.

Martin, R.S., Witt, M.L.I., Pyle, D.M., Mather, T.A., Watt, S.F.L., Bagnato, E., and Calabrese, S. (2011). Rapid Oxidation of Mercury (Hg) at Volcanic Vents: Insights from High Temperature Thermodynamic Models of Mt Etna's Emissions. *Chemical Geology,* 283(3–4), 279–286. doi:10.1016/j.chemgeo.2011.01.027.

Marumoto, K., Sudo, Y., and Nagamatsu, Y. (2017). Collateral Variations between the Concentrations of Mercury and Other Water Soluble Ions in Volcanic Ash Samples and Volcanic Activity during the 2014-2016 Eruptive Episodes at Aso Volcano, Japan. *Journal of Volcanology and Geothermal Research,* 341, 149–157. doi:10.1016/j.jvolgeores.2017.05.022.

Mather, T.A., Witt, M., Pyle, D.M., Quayle, B.M., Aiuppa, A., Bagnato, E.R., Martin, R.S., Sims, K.W., Edmonds, M., Sutton, A.J., and Ilyinskaya, E. (2012). Halogens and trace metal emissions from the ongoing 2008 summit eruption of Kīlauea volcano, Hawai`i. *Geochimica et Cosmochimica Acta, 83*, 292-323. doi:10.1016/J.GCA.2011.11.029.

McGee, K.A., Doukas, M.P., McGimsey, R.G., Neal, C.A., & Wessels, R.L. (2010). Emission of SO_2, CO_2, and H_2S from Augustine Volcano, 2002 – 2008. In J. A. Power, M. L. Coombs, & J. T. Freymueller (Eds.), *The 2006 eruption of Augustine Volcano, Alaska*. U.S. Geological Survey Professional Paper 1769, 631– 644.

McGimsey, R.G., Neal, C.A., and Riley, C.M. (2001). Areal Distribution, Thickness, Mass, Volume, and Grain Size of Tephra-Fall Deposits from the 1992 Eruptions of Crater Peak Vent, Mt. Spurr Volcano, Alaska. *USGS Open-File Report 01–370*. http://pubs.er.usgs.gov.

Miller, T.P., McGimsey, R.G., Richter, D.H., Riehle, J.R., Nye, C.J., Yount, M.E., and Dumoulin, J.A. (1998). Catalog of the Historically Active Volcanoes of Alaska. *Open-File Report*. doi:10.3133/ofr98582.

Newhall, C.G., and Self, S. (1982): The Volcanic Explosivity Index (VEI) an Estimate of Explosive Magnitude for Historical Volcanism. *Journal of Geophysical Research: Oceans* 87 (C2): 1231–1238. doi:10.1029/JC087iC02p01231.

Nriagu, J. and Becker, C. (2003). Volcanic Emissions of Mercury to the Atmosphere: Global and Regional Inventories. *Science of the Total Environment,* 304(1–3), 3–12. doi:10.1016/S0048-9697(02)00552-1.

Ohki, A., Nakajima, T., Hayashi, K., Taniguchi, H., Haraguchi, K., and Takanashi, H. (2016). Levels of Hg and other chemical elements in volcanic ash fall samples erupted from Mt. Sakurajima, Japan. *Toxicological and Environmental Chemistry*. 98(7), 778-786. doi:10.1080/02772248.2016.1139117.

Pyle, D.M. and Mather, T.A. (2003). The Importance of Volcanic Emissions for the Global Atmospheric Mercury Cycle. *Atmospheric Environment,* 37(36), 5115–5124. doi:10.1016/j.atmosenv.2003.07.011.

Rea, L.D., Castellini, J.M., Avery, J.P., Fadely, B.S., Burkanov, V.N., Rehberg, M.J., and O'Hara, T.M. (2020). Regional variations and drivers of mercury and selenium concentrations in Steller sea lions. *Science of The Total Environment,* 744. doi:10.1016/j.scitotenv.2020.140787.

Ricca, M.A., Miles, A.K., amd Anthony, R.G. (2008). Sources of organochlorine contaminants and mercury in seabirds from the Aleutian archipelago of Alaska: Inferences from spatial and trophic variation. *Science of The Total Environment,* 406, 308-323. doi:10.1016/j.scitotenv.2008.06.030.

Roos-Barraclough, F., Martinez-Cortizas, A., García-Rodeja, E., and Shotyk, W. (2002). A 14 500 Year Record of the Accumulation of Atmospheric Mercury in Peat: Volcanic Signals, Anthropogenic Influences and a Correlation to Bromine Accumulation. *Earth and Planetary Science Letters,* 202(2), 435–451. doi:10.1016/S0012-821X(02)00805-1.

Rytuba, James J. (2003). Mercury from Mineral Deposits and Potential Environmental Impact. *Environmental Geology,* 43(3), 326–338. doi:10.1007/s00254-002-0629-5.

Schuster, P.F., Krabbenhoft, D.P., Naftz, D.L., Cecil, L.D., Olson, M.L., Dewild, J.F., Susong, D.D., Green, J.R., and Abbott, M.L. (2002). Atmospheric Mercury Deposition during the Last 270 Years: A Glacial Ice Core Record of Natural and Anthropogenic Sources. *Environmental Science & Technology,* 36(11), 2303–2310. doi:10.1021/es0157503.

Smichowski, P., Gómez, D., Rosa, S., and Polla, G. (2003). Trace Elements Content in Size-Classified Volcanic Ashes as Determined by Inductively Coupled Plasma-Mass Spectrometry. *Microchemical Journal,* 75(2), 109–117. doi:10.1016/S0026-265X(03)00089-4.

Stewart, C., Damby, D.E., Tomašek, I., Horwell, C.J., Plumlee, G.S., Armienta, M.A., Hinojosa, M.G.R., Appleby, M., Delmelle, P., Cronin, S., Ottley, C.J., Oppenheimer, C., and Morman, S. (2020). Assessment of leachable elements in volcanic ashfall: a review and evaluation of a standardized protocol for ash hazard characterization. *Journal of Volcanology and Geothermal Research,* 392. doi:10.1016/j.jvolgeores.2019.106756.

Stracquadanio, M., Dinelli, E., and Trombini, C. (2003). Role of Volcanic Dust in the Atmospheric Transport and Deposition of Polycyclic Aromatic Hydrocarbons and Mercury. *Journal of Environmental Monitoring,* 5(6), 984–988. doi:10.1039/B308587B.

U.S. EPA. (1998): EPA Method 7473 (SW-846). Mercury in Solids and Solutions by Thermal Decomposition, Amalgamation, and Atomic Absorption Spectrophotometry. Washington D.C. https://www.epa.gov/esam/epa-method-7473-sw-846-mercury-solids-and-solutions-thermal-decomposition-amalgamation-and.

Varekamp, J.C. and Buseck, P.R. (1986). Global mercury flux from volcanic and geothermal sources. *Applied Geochemistry,* 1(1), 65–73. doi:10.1016/0883-2927(86)90038-7.

Wallace, K.L., Neal, C.A., and McGimsey, R.G. (2010). Timing, Distribution, and Character of Tephra Fall from the 2005-2006 Eruption of Augustine Volcano. *US Geological Survey Professional Paper*, no. 1769, 187–215. doi:10.3133/pp17699.

Wallace, K.L., Schaefer, J.R., and Coombs, M.L. (2013). Character, Mass, Distribution, and Origin of Tephra-Fall Deposits from the 2009 Eruption of Redoubt Volcano, Alaska-Highlighting the Significance of Particle Aggregation. *Journal of Volcanology and Geothermal Research,* 259, 145–169. doi:10.1016/j.jvolgeores.2012.09.015.

Wedepohl, H.K. (1995). The Composition of the Continental Crust. *Geochimica et Cosmochimica Acta,* 59(7), 1217–1232. doi:10.1016/0016-7037(95)00038-2.

Werner, C., Kelly, P.J., Doukas, M., Lopez, T.M., Pfeffer, M., McGimsey, R., and Neal, C. (2013). Degassing of CO2, SO2, and H2S associated with the 2009 eruption of Redoubt Volcano, Alaska. *Journal of Volcanology and Geothermal Research,* 259, 270-284. doi:10.1016/j.jvolgeores.2012.04.012.

Wilson, F.H., Hults, C.P., Mull, C.G, and Karl, S.M (2015). Geologic Map of Alaska. *U.S. Geological Survey Scientific Investigations Map 3340*, 196. doi:10.3133/sim3340.

Witt, M.L.I., Mather, T.A., Pyle, D.M., Aiuppa, A., Bagnato, E., and Tsanev, V.I. (2008). Mercury and Halogen Emissions from Masaya and Telica Volcanoes, Nicaragua. *Journal of Geophysical Research: Solid Earth,* 113(6), 1–15. doi:10.1029/2007JB005401.

Zambardi, T., Sonke, J.E., Toutain, J.P., Sortino, F., and Shinohara, H. (2009). Mercury Emissions and Stable Isotopic Compositions at Vulcano Island (Italy). *Earth and Planetary Science Letters,* 277(1), 236–243. doi:10.1016/j.epsl.2008.10.023.

Zhang, Y., Li, A., and Hu, H. (2019): Crustal Structure in Alaska from Receiver Function Analysis. *Geophysical Research Letters* 46 (3): 1284–1292. doi:10.1029/2018GL081011.

Zhang, P. and Zhang, Y. (2022). Earth system modeling of mercury using CESM2 – Part 1: Atmospheric model CAM6-Chem/Hg v1.0. *Geoscientific Model Development,* 15, 3587–3601. doi:10.5194/gmd-15-3587-2022.

Chapter 3 The ghost plume phenomenon and its impact on zenith-looking remote sensing measurements of volcanic SO_2 emission rates[2]

3.1 Introduction

Monitoring volcanic sulfur dioxide (SO_2) emissions provides insights into subsurface conditions that may precede volcanic eruptions, such as changes in magma supply or conduit permeability (Fischer et al., 2002; Kunrat et al., 2022). After H_2O and CO_2, SO_2 is the third most abundant volatile species in volcanic plumes and is generally easier to measure relative to H_2O and CO_2 due to the negligible SO_2 present in the (unpolluted) background atmosphere (Mather, 2013; Oppenheimer et al., 2014). Differential Optical Absorption Spectroscopy (DOAS), using scattered ultraviolet (UV) solar radiation as a light source, is currently the most widely used technique for deriving high temporal resolution measurements of volcanic SO_2 emission rates (Edmonds et al., 2003; Galle et al., 2003; Galle et al., 2010; Arellano et al., 2021). This method builds upon the Bouguer-Lambert-Beer or extinction law which describes the extinction of radiation as it passes through a medium:

$$I(\lambda) = I_0(\lambda)e^{(-\sigma(\lambda)\times c\times L)} \quad \text{(Eq. 3.1)}$$

Here, $I_0(\lambda)$ is the initial light intensity without absorption by the medium as a function of wavelength λ, $I(\lambda)$ is the light intensity after absorption in the medium, $\sigma(\lambda)$ is the wavelength-dependent absorption cross section of the medium, c is the concentration of the absorbers, and L is the optical path length.

In addition to narrow-band absorption by trace gases, radiation traveling through the atmosphere is subject to scattering on air molecules and scattering and absorption on aerosols. These processes are broadband in nature, meaning they affect all wavelengths in a similar way, in this case over a window of several 10s of nanometers (nm). One exception is the Ring-effect (Grainger and Ring, 1962), which is highly structured and therefore it is treated as a pseudo-absorber. The DOAS technique separates the broadband effects from the trace gas absorption by including a low-order polynomial in the spectral analysis, thus effectively high-pass filtering the spectra (Platt and Stutz, 2008). This enables SO_2 to be successfully measured in Earth's atmosphere in the presence of light scattered by gases, aerosol particles, and cloud droplets.

The distribution of trace gases in the atmosphere is heterogeneous. For example, SO_2 may be present in a volcanic plume, but not in the background atmosphere. Because an individual DOAS

[2] Kushner, D.S., Lopez, T.M., Kern, C.K., Arellano, S.A., and Pérez-Rodríguez, N.M. (Submitted): The ghost plume phenomenon and its impact on zenith-looking remote sensing measurements of volcanic SO_2 emission rates.

measurement does not provide any information on the distribution c(l) of the sought-after trace gas concentration along the light path L, the column density is commonly introduced as follows:

$$S = \int_L^0 c(l)\, dl \qquad \text{(Eq. 3.2)}$$

Where dl is a differential element of light path. Using this terminology, the DOAS equation can then be formulated as:

$$\tau = ln\left(\frac{I_0}{I}\right) = \sum_i \sigma_i S_i + P_n \qquad \text{(Eq. 3.3)}$$

As shown in Eq. 3.3, the measured optical depth τ is modeled as a linear combination of all trace gases with absorption features in the chosen wavelength region, whereby the absorption cross section, σ_i, of each species is multiplied by a column density, S_i. Broadband scattering and absorption effects are described by the low-order polynomial, P_n. During the DOAS fit procedure, the column densities are varied until a best fit between the measurement of log (I_0/I) and the model is achieved (Platt and Stutz, 2008). The column densities, S_i, which achieve the best fit to the measurements represent the results of the DOAS measurement.

DOAS-derived SO_2 emission rates are calculated through a multistep process (detailed in Galle et al., 2003), and can be used by volcano observatories to track changes in volcanic emissions over time. A series of individual SO_2 column density measurements are collected while scanning across a plume perpendicular to its propagation direction. Integration of the SO_2 column densities over the plume cross section yields the SO_2 cross-sectional burden (CSB; e.g., in SO_2 molecules m^{-1}). Multiplication of this burden by the normal component of plume velocity (equal to wind speed at the plume altitude in m s^{-1}) yields the emission rate of the desired gas for the volcano (in units of molecules s^{-1}, which may then be converted to t d^{-1} or kg s^{-1}; McGonigle et al., 2005).

When volcanic SO_2 emission rates are retrieved from scanning or mobile DOAS measurements, it is often assumed that the measured light has passed through the region of interest (in this case the volcanic plume) along a straight path aligned with the telescope's viewing direction. However, under real-world conditions, photons may travel along complex pathways and may be absorbed or multiply scattered by aerosols or clouds in the atmosphere, complicating the interpretation of retrieved SO_2 column densities and potentially skewing the resulting emission rate calculations (Millán, M.M., 1980; Williams-Jones et al., 2008). Previous work has highlighted how non-ideal measurement conditions, such as an opaque plume or clouds between the instrument and plume can significantly impact photon paths in and around volcanic plumes and lead to order-of-magnitude errors in derived emission rates (Kern et al., 2010). Recent work by Wagner et al. (2023) has also highlighted that complex radiative transfer pathways may result in pixel saturation, artificially elongated plumes, and other geometric effects for satellite

observations of gases that absorb in the UV spectrum. Additionally, scattering of photons which have not passed through a volcanic plume into the instrument field of view may lead to substantial underestimation of SO_2 column densities, an effect commonly referred to as light dilution (Mori et al., 2006).

3.1.1 Ghost plumes

Further complicating accurate assessments of volcanic SO_2 cross-sectional burdens are phenomena dubbed "ghost plumes", where either an illusory plume is observed geometrically offset from where it is expected, or as a modification of the shape of the real plume. Ghost plumes occur when a cloud or layer aerosol of aerosolized particles is present between the DOAS telescope and the volcanic plume under specific conditions of illumination depending on the relative position of the sun, the plume, scattering cloud, and instrument. During these measurement conditions, solar UV radiation that has already passed through the plume is then scattered toward the instrument by a cloud layer below the plume. Particularly, if the sun is not directly overhead, this can lead to the plume being detected in a position or direction in which it is not actually located and potentially producing a skewed CSB. Because the ghost plume effect is a result of radiative transfer, this phenomenon is not restricted exclusively to DOAS (either scanning or zenith-facing) measurements and should also occur in other techniques used to measure volcanic degassing including SO_2 cameras and correlation spectrometers (COSPEC; Williams-Jones et al., 2008). Despite the potential ubiquity of this effect, there have not been quantitative studies to assess or identify the impact on field measurements. Hereafter, we concentrate on only zenith-facing DOAS measurements.

Photons that pass through the plume and then encounter a cloud layer are then scattered down into the telescope field of view at the incident solar angle (Figure 3.1). The result of photon scattering from a solar position which isn't directly on top of the plume is a projected (offset) location below a geometrically straight path from the sun position to the top of the cloud layer. Because of the potential large and unconstrained errors introduced in DOAS SO_2 measurements collected under non-ideal (e.g., cloudy or foggy) atmospheric conditions, these data are often not collected or utilized. This can result in limited observations to characterize volcanic degassing - especially for remote volcanoes such as in Alaska, which are infrequently visited in the field and often obscured by clouds and/or fog.

If several crucial aspects of an upwards-viewing traverse are known, then the emergence of a ghost plume should be geometrically resolvable through simple trigonometry. Specifically, the three important parameters required to determine the predicted distance between a real volcanic plume and a ghost plume are the solar zenith angle (SZA), the solar azimuth relative to the plume, and the altitude difference between the plume and a condensed layer (e.g. cloud or fog) producing single scattering of light. Figure 3.1 illustrates a case where the solar azimuth is parallel to the path of the DOAS traverse. In this scenario the ghost plume maximum SO_2 column density would be geometrically expected to occur

using the notation: d for horizontal distance of plume offset, h for difference in altitude between plume and scattering cloud, as shown in Figure 3.1:

$$d = h \times \tan(SZA) \quad \text{(Eq. 3.4)}$$

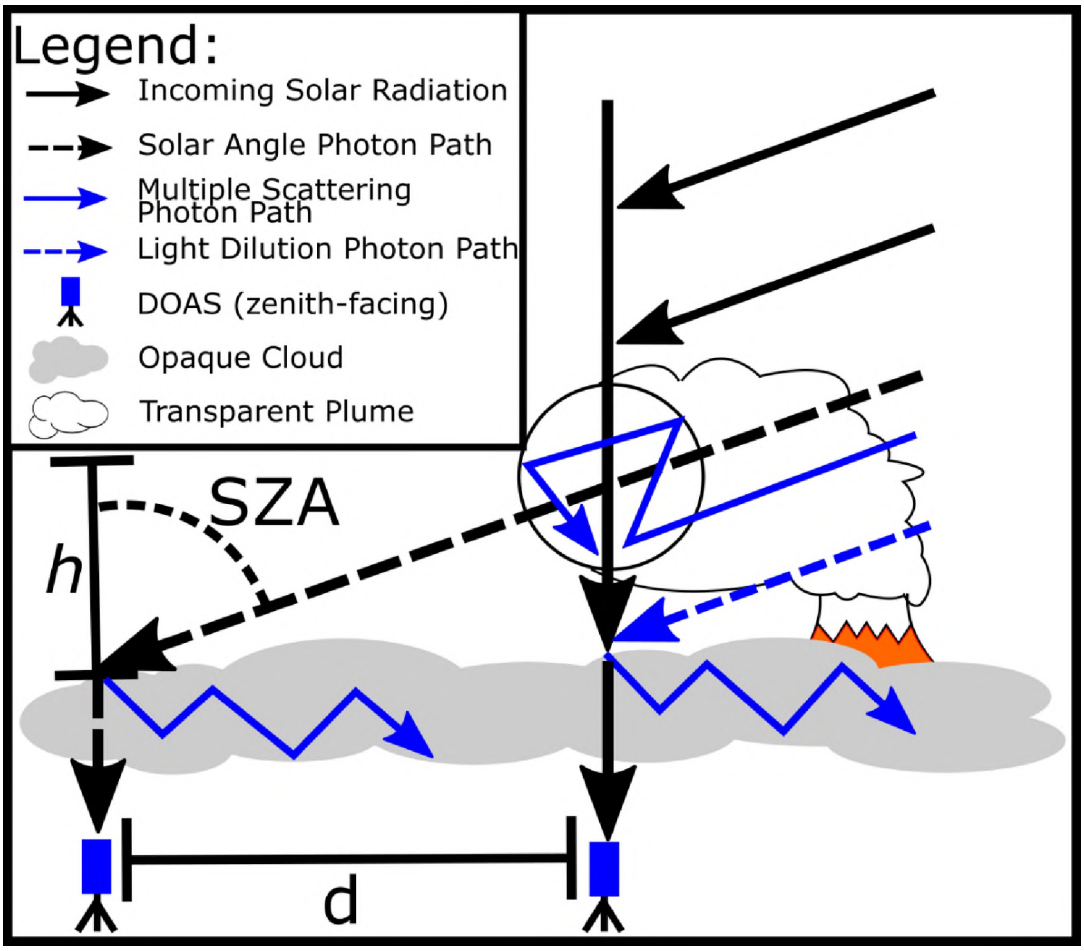

Figure 3.1 Ghost plume mechanism with an assumed ideal photon pathway from the direct solar beam that crosses the plume and gets scattered down by single scattering in a cloud below the plume towards an up-looking instrument. The key parameters are the solar zenith angle, SZA; the altitude difference between the plume and a lower layer of clouds, h; and the offset-distance d where the ghost plume is observed.

3.2 Methods

To assess the utility of real-world SO_2 emission rate measurements obtained where there is a cloud layer present between the DOAS telescope and the volcanic plume, we simulate upward-looking DOAS measurements under realistic conditions. We use a radiative transfer model to test the influence of factors such as SZA, cloud height, plume height, cloud layer thickness, cloud aerosol optical depth (AOD), and plume AOD on the derived SO_2 cross-sectional burdens. We compare cross-sectional burdens of simulated traverses to theoretical (input) parameters. We use these results to provide guidelines for

evaluating DOAS results under similar conditions to make the best use of available data within a reasonable uncertainty threshold. Our modeled results are then used to evaluate the utility of a sample set of DOAS measurements collected at La Palma (Canary Islands, Spain) volcanoes, under suboptimal conditions, that show what appears to be a ghost plume.

3.2.1 Model constraints

We simulate DOAS traverses using the McArtim radiative transfer model (Deutchmann et al., 2011) to test the effects of the specified parameters (Table 3.1) on the retrieved SO_2 CSB. McArtim is a 3-dimensional forward Monte Carlo radiative transfer model. It uses back-propagation to simulate photon paths from the instrument to the sun along Earth's atmosphere specified by different profiles of composition including gas molecules, clouds and aerosol particles with different scattering and absorption parameters. We conducted 217 different model permutations that vary cloud layer thickness, SZA, plume AOD, and cloud AOD to test the influence of these variables on the resulting plume SO_2 CSB. Each simulation assumes: (a) a cylindrical plume with constant diameter of 400-m, centered at 1600 m altitude containing a uniform SO_2 mixing ratio of 250 ppb corresponding to a column density through the plume center of 2.5×10^{17} molecule cm^{-2}, and (b) a rectangular aerosol cloud layer below the plume with infinite length and variable thickness (Table 3.1), centered at 400 m elevation and containing no SO_2. We simulate 10^5 photon trajectories through our modeled atmosphere that produce a statistical error in the radiance (noise) of <10%. By moving the horizontal position of our instrument, we retrieve the SO_2 column density at each measurement location within a simulated mobile DOAS traverse. A traverse consists of simulated SO_2 column density measurements made perpendicular to plume direction at 50 m increments, from -3000 m to +2000 m horizontal positions below the center of the simulated plume. The relative azimuth of the sun is chosen to be perpendicular to the plume for simplified geometric predictions of ghost plume location, where a non-perpendicular azimuth of the sun relative to the plume may cause a ghost plume manifestation closer to the plume. The traverse length is asymmetrical (1000 m longer on one side) to account for the expected manifestation of the ghost plume on the side farthest from the sun. Each simulated DOAS retrieval is conducted at 315 nm, which was selected to describe absorption from a typical DOAS fit window for SO_2 (Kern et al., 2010). Fixed instrument parameters during each simulation were an instrument altitude of 0 m and an instrument field of view of 0.3°. Fixed atmospheric parameters during each simulation were a plume single scattering albedo of 0.9 and an asymmetry factor of 0.8; a cloud single scattering albedo of 1 and an asymmetry factor of 0.8; and a ground albedo of 0.03.

Table 3.1 Model parameter values used in this study.

Parameter	Variables Used					
Cloud layer thickness [m]	200	400	800			
SZA [°]	1	30	60			
Plume AOD	0	1	4	8		
Cloud AOD	0	1	2	4	8	20

3.2.2 Plume selection criteria for determining cross-sectional burden

All DOAS measurements initially determine the column density along an effective light path of the measured photons. In upward-looking mobile DOAS measurements of volcanic plumes, it is common to assume that the effective light path is equal to a straight vertical line through the plume, the so-called vertical column density (VCD). Although this approximation can fail for opaque plumes or cloudy atmospheric conditions, as we will discuss here, it is an acceptable assumption for optimal viewing conditions and transparent plumes. The standard approach to calculate plume SO_2 CSB (molecule m^{-1}) is to integrate the area under the SO_2 VCD profile for each traverse. These integrated areas require defining (1) the plume limits, or the X (location) values where the plume profile transitions from background to plume and plume to background, and (2) the plume baseline, or the minimum SO_2 VCD value representative of background conditions. Both parameters present an opportunity to have user-induced bias which can contribute to measurement uncertainties.

We aim to define some criteria to allow plume baseline and limit parameters to be calculated consistently and automatically (Figure 3.2A). To identify plume limits we first calculate a moving mean SO_2 VCD for 5 adjacent pixels to minimize noise. We then identify plume limits as the derivative of the SO_2 VCD along horizontal position ($\frac{dVCD}{dx}$; Figure 3.2B) where the plume beginning and end are defined as the first and last $\frac{dVCD}{dx}$ value above and below a threshold value. We select -1×10^{13} (molecule cm^{-3}) as our plume limit threshold because it is sensitive enough to capture plume boundaries without being too sensitive to changes in VCD due to background noise. The minimum VCD value between the plume limits is then selected as the plume baseline and subtracted from all other VCD values. The simulated CSB, or the integrated area beneath the curve, was then compared to the theoretical CSB of the plume to assess accuracy, where the theoretical CSB may be calculated as:

$$CSB_{theoretical} = \frac{\pi}{4} \times V_{SO_2,max} \times d_{plume} \quad \text{(Eq. 3.5)}$$

with both the maximum VCD ($V_{SO2,\,max}$) and the plume diameter d_{plume} being known input parameters.

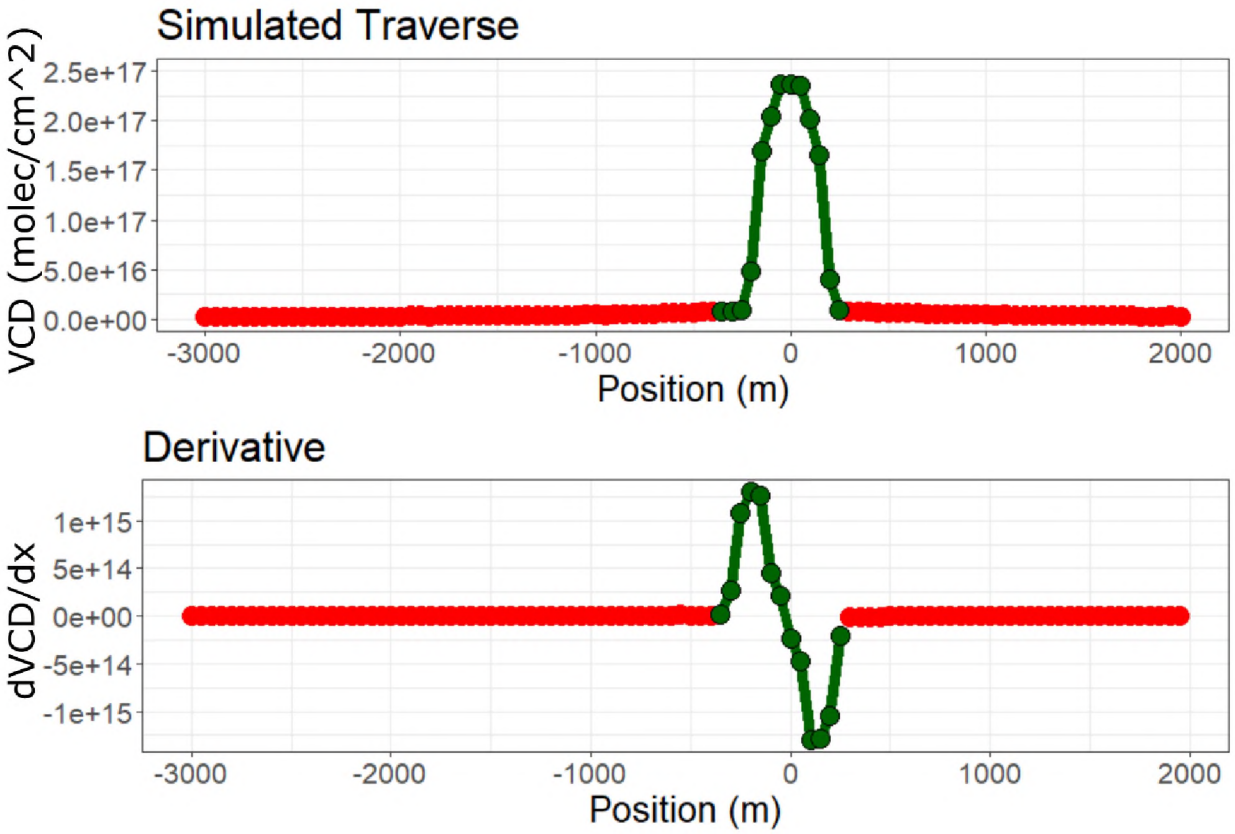

Figure 3.2 Illustration of baseline and plume limit selection method. (Top) Example traverse with points inside the limits of plume selection in green and points excluded in red. (Bottom) Plume baseline and limits related to the $\frac{dVCD}{dx}$ threshold, where the first value over 1×10^{13} (molecule cm^{-3}) is defined as the plume beginning and the last value under 1×10^{13} (molecule cm^{-3}) is defined as the plume boundaries.

3.3 Results

3.3.1 Modeled traverses

Based on our model runs, we find that increasing cloud and plume AOD cause a general broadening and decrease in the amplitude of the VCD curve, and SZA >1 lead to the formation of horizontally offset ghost plumes. These results are illustrated by six scenarios depicted in Figure 3.3A-F. The scenarios vary by increasing SZA from 1° (0° is avoided) to 30° to 60° as we model zenith-looking observations, with the left column representing a transparent plume (AOD = 0) and the right column representing an opaque plume (AOD = 4). We define AODs between 1 and 3 as translucent. Examples are shown for a 400 m thick cloud in each scenario with a cloud AOD varied from 0 representing a translucent plume, to 20 representing a highly opaque plume. Detailed observations for each scenario with 400 m thick clouds are described below.

3.3.1.1 Scenario A (Transparent plume, SZA = 1)

The simplest model scenario is shown in Figure 3.3A. In this case we have a SZA = 1°, representing photons supplied from a nearly directly overhead source and a translucent plume (AOD = 0). In each scenario the simulated SO_2 VCD curve is shown as a function of cloud AOD, which varies from 0 (red line – transparent cloud) to 20 (purple line - opaque cloud). In the case of a transparent cloud (AOD = 0, red line) the simulated measurements match the actual (input) plume SO_2 VCD versus position curve in shape and amplitude, with a plume width of ~400 m and a maximum VCD of 2.37×10^{17} molecule cm^{-2} at the plume center. Increasing cloud AOD produces a broadening (negative kurtosis) of the plume VCD curve. At lower cloud AOD values (1 – 4), this broadening is generally gradual and has minimal effect on the apparent plume width or maximum VCD. Transitioning to higher cloud AOD scenarios (e.g. >4), the peak broadening effect increases, resulting in measured plumes >2 km wider than the actual plume and maximum SO_2 VCDs <40% of actual values.

The observed variation in SO_2 CSB error with respect to the theoretical model as a function of increasing cloud AOD is shown in Figure 3.4A for both transparent (AOD = 0) and opaque (AOD >4) plumes. The integrated CSB from a case with both a transparent plume and cloud (e.g., Scenario A, red line, Figure 3.3A) is 95% of the expected value. Increasing cloud AOD values to >1 leads to increasing underestimations of the overall CSB until cloud AOD values of > 8, after which the burden trends back towards the expected value. In all cases for this scenario (transparent plume and vertical SZA), SO_2 CSBs are within 27% of the expected value and the majority are within 10% of the expected value.

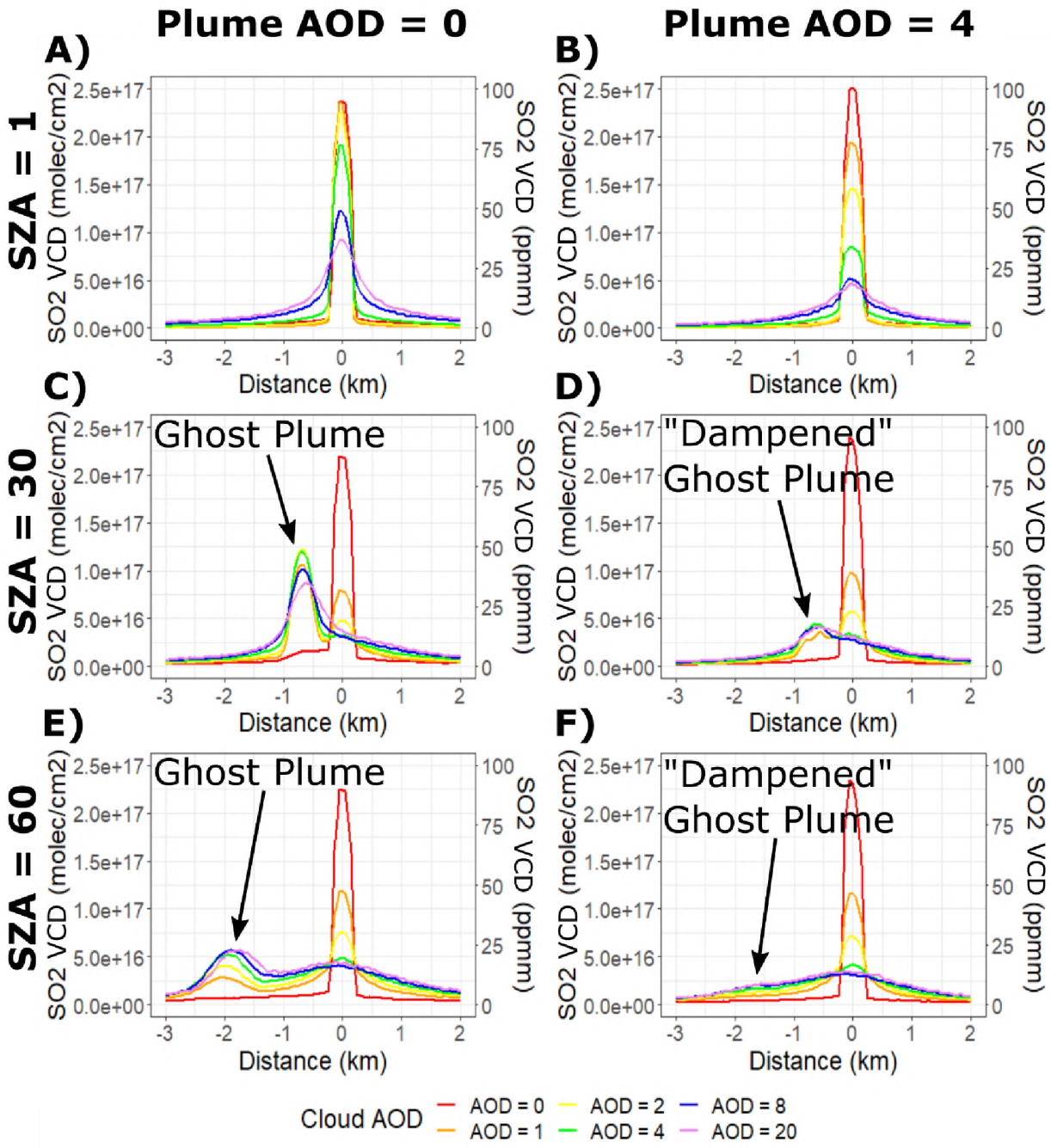

Figure 3.3 Simulated DOAS traverses for a 400 m diameter, 2.5×10^{17} molecule cm^{-2} SO_2 (100 ppm•m) column density volcanic plume with a 400 m thick cloud between the plume and the telescope. Traverses demonstrate two plume AOD conditions: transparent (AOD = 0; left column) and opaque (AOD = 4; right column), and three SZA (top: SZA = 1°; middle: SZA = 30°; bottom: SZA = 60°). The red line in all panels represents simulated traverse results for a transparent low cloud which accurately depicts the plume location. Increased SZA results in a peak SO_2 VCD displaced horizontally by ~700 m from the true location for a SZA of 30° and by ~2050 m for a SZA of 60°. Increased plume AOD results in an attenuation of the ghost plume effect such that it is barely perceptible for SZA = 60°, AOD >= 4 scenarios.

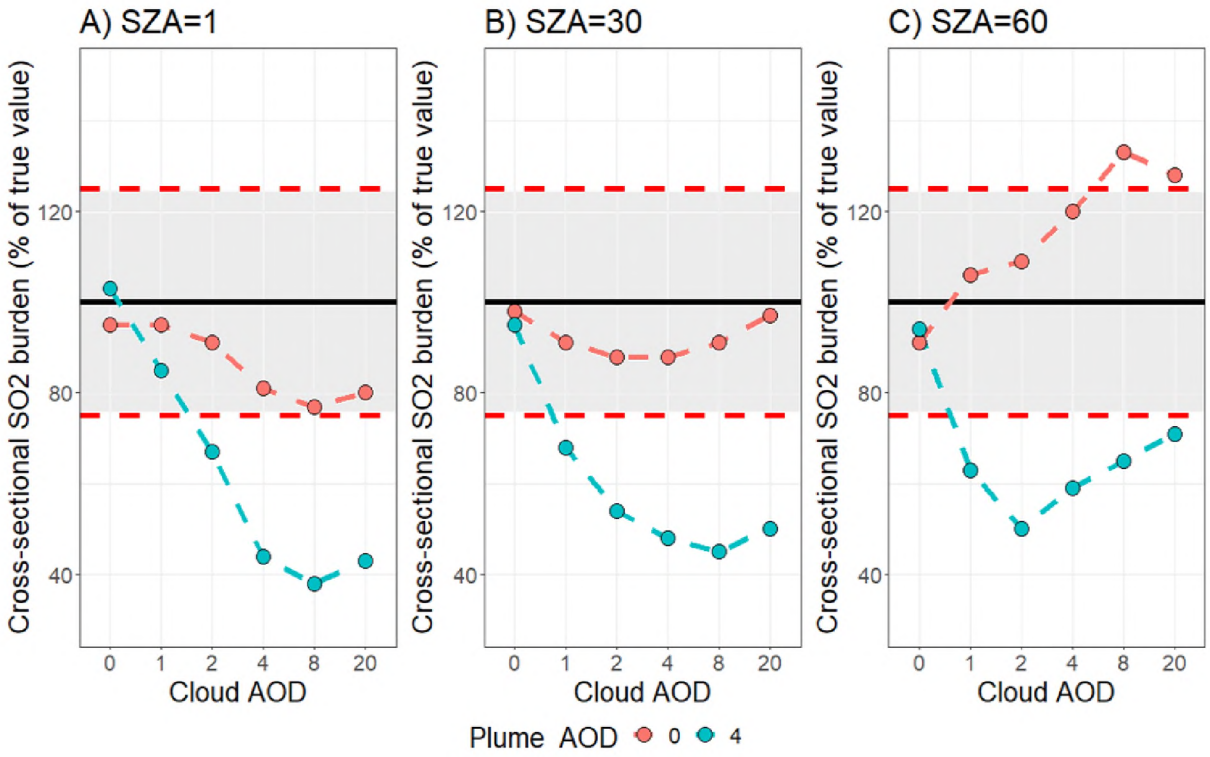

Figure 3.4 Error associated with clouds beneath six scenarios shown in Figure 3.3. SO_2 CSB is expressed as a % of the theoretical value (black horizontal line) with ±25% confidence intervals (red dashed horizontal line) for SZA = 1° (left), SZA = 30° (center), and SZA = 60° (right) under differing cloud AOD conditions (x-axis). CSB from transparent plumes and translucent to opaque low clouds (red points) are generally within the accepted confidence interval while CSB from traverses with translucent to opaque low clouds and opaque plumes (blue points) are largely underestimated below the ideal confidence interval.

3.3.1.2 Scenario B (Opaque plume, vertical SZA)

This scenario is identical to scenario A (SZA = 1°, cloud AOD = 0 – 20) with the exception that plume AOD has been increased to 4, representing an opaque plume. In this case we observe an immediate and rapid dampening of the plume maximum SO_2 VCD with the slightest increase in cloud opacity (Figure 3.3B), where the maximum VCD is reduced by ~20% for a translucent cloud with AOD = 1 and up to 82% for an opaque cloud with AOD = 20 in comparison to that of a transparent plume (AOD = 0). In this scenario the shape of the plume VCD curve also appears to be more rounded or negatively kurtosed than its transparent counterpart (scenario A), resulting in slightly broader profiles across all traverses where cloud AOD > 1.

Errors in plume CSB as a function of cloud opacity in scenario B follow similar trends to scenario A (blue line Figure 3.4A), if not more exaggerated. Initial CSB for transparent cloud scenarios are 103% of the expected value and decrease rapidly to an eventual minimum of 38% the expected value at a cloud

AOD = 8. At cloud AOD values > 8, SO_2 CSBs begins to trend upwards slightly. In the case of an opaque plume CSBs exceed errors of 20% of the expected value for cloud AOD > 1.

3.3.1.3 Scenario C (Transparent plume, SZA = 30°)

In scenario C, we start to investigate the effects of increasing SZA from 1° to 30°. First, with the cloud AOD = 0 traverse we find that an aspect of skewness, or tailing, is introduced into the VCD curve away from the direction of the sun. This tail manifests as an area of higher-than-background VCD extending approximately 1 km away from the plume center (Figure 3.3C), suggesting the hint of a ghost plume. Immediately at nonzero cloud AOD values we model apparent "ghost plumes" where a portion of the plume SO_2 VCD is spatially offset from its expected location, with a local VCD maximum at ~700 m for all cloud AOD > 0 values. At lower cloud AOD values of 1 – 2, our models indicate a rapid decrease in maximum SO_2 VCD to <40% of the value for a transparent cloud (Figure 3.3C) at the expected location. In conjunction with the rapid VCD decrease at the expected location, VCD rapidly increases under the ghost plume location leading to two local VCD maxima. Increasing cloud AOD > 4 finds no apparent peak at the actual plume location, but rather a single SO_2 maximum value in the geometrically offset (ghost-plume) location skewed slightly in the direction of the sun. Similar to scenario A, we find that traverses modeled under higher cloud AOD values lead to broader SO_2 VCD peaks.

All burdens under scenario C (Figure 3.4B) underestimate the actual value to within 12% regardless of cloud AOD. Transparent plume model results for these conditions give SO_2 burdens equal to 98% of the true value, the closest of all iterations considered for this study. A minimum burden of 88% of the expected value is achieved at cloud AOD values of 2. The SO_2 CSB increases to 97% of expected at cloud AOD = 20. Patterns observed in this scenario are similar to those under scenario A, however CSBs begin to increase again after a lower degree of cloud opacity around AOD values of 2 – 4.

3.3.1.4 Scenario D (Opaque plume, SZA = 30°)

In scenario D, we now consider an opaque plume (plume AOD = 4) with an increased SZA of 30°. In this case, we still observe a ghost plume, however the magnitude of the plume SO_2 VCD appears to be significantly "dampened" in comparison to scenario C. During opaque cloud conditions (AOD ≥ 4), a single peak is present with the maximum VCD manifesting ~700 m from the actual plume position with the direction of tailing towards the sun. Our model traverses also indicate some differences with respect to scenario C in VCD beneath the plume. At cloud AOD ≤ 2 values, the maximum VCD beneath the actual plume location is larger than scenario C (transparent plume).

SO_2 CSB for scenario D is underestimated with respect to theoretical for all cloud AOD conditions. With increasing cloud AOD there is a precipitous decline in SO_2 CSB, to an eventual minimum of 44% the true value at a cloud AOD of 8. At cloud AOD values >8, our estimates of the CSB

are slightly less underestimated, at 50% the true value. For this scenario of an opaque plume and SZA = 30° (blue line Figure 3.4B), only a cloud AOD = 0 achieves the desired uncertainty of ±25%.

3.3.1.5 Scenario E (Transparent plume, SZA = 60°)

In scenario E, we examine conditions under which a DOAS traverse is conducted with a solar position approaching the horizon (SZA = 60°). Many aspects of these traverses are similar to scenario C though slightly more exaggerated. During ideal conditions (plume AOD = 0) we observe tailing in the SO_2 VCD curve several kilometers further away from the sun and with a lower magnitude than in scenario C. Increasing cloud opacity (cloud AOD > 1) leads to a rapid decline in SO_2 VCD to < 50% of the value for no clouds and the emergence of a ghost plume ~2000 m from the expected location. In contrast to scenario C, cloud AOD values > 4 do not appear to entirely obfuscate the plume SO_2 peak beneath its expected location. Instead, our model shows one peak at the ghost plume location and one broad, heavily kurtosed, peak beneath the expected location.

Unlike the previous scenarios that largely underestimate the plume SO_2 CSB, scenario E shows an SO_2 plume CSB overestimated with respect to actual, in all cases except for a cloud AOD = 0. We observe a minimum SO_2 CSB of 90% the true value in ideal atmospheric conditions (cloud AOD = 0; Figure 3.4), and a maximum (overestimation) of 133% the true value for an opaque cloud (cloud AOD = 8). This scenario also shows the greatest variability in SO_2 CSB (43%) of those considered between high and low AOD traverses.

3.3.1.6 Scenario F (Opaque plume, SZA = 60°)

As an end-member scenario, we investigate a scenario with an opaque plume and a SZA = 60°. For cloud AOD = 0 conditions, the plume appears in its expected location with no apparent tail or ghost plume effect seen. As cloud opacity increases (cloud AOD > = 1) the SO_2 VCD curve appears in all cases to be a single, heavily kurtosed and slightly skewed peak. Curve skewness and kurtosis both increase with increasing cloud AOD and in no case is there a discernible ghost plume. Instead, in cloud AOD > 4 scenarios, we model a single SO_2 peak with a maximum VCD approximately beneath the expected plume location extending in width over ~5 km or ~4.5 km wider than theoretical.

The modeled SO_2 CSB for scenario F is underestimated with respect to theoretical in all cases. This underestimation increases to 50% of the true value as cloud opacity increases from AOD = 0 – 2. For cloud AOD > 2 conditions the underestimation decreases, reaching 71% of the true value. As also found in scenario E, only the cloud AOD = 0 case of scenario F yields an SO_2 CSB within the desired uncertainty of ±25%.

3.3.1.7 Additional Factors

General observations made for the 400 m thick cloud scenarios discussed above are broadly consistent with model runs performed for other cloud thickness and not discussed in detail here. Thicker clouds of 800 m and thinner clouds of 200 m do not produce appreciable deviations in observed peak shapes relative to the 400 m thick cloud scenarios, with the few exceptions being those scenarios with substantial amounts of multiple scattering such as for 800 m thick clouds and cloud AOD > 8.

We also explore the effects of plume AOD between 0 – 8 on the uncertainty in derived SO_2 CSBs. Unlike cloud thickness, different plume AOD values have a more substantial effect on CSB uncertainty as demonstrated in Figure 3.4 considering differences between a plume AOD of 0 and 4 and found in previous studies (Kern et al., 2010; Kern et al., 2012). We find that a plume AOD of 1, representing the limit of a plume considered translucent, leads to a burden underestimation 1 – 15% lower than corresponding transparent plume (AOD = 0) scenarios. We also find that CSBs under a heavily opaque plume (AOD = 8) are consistently lower than plume AOD = 4 scenarios, with uncertainties regularly exceeding 50% of theoretical.

3.4 Discussion

3.4.1 Model results and errors in CSB retrievals

Our model results find that accurate SO_2 emission rate measurements may be acquired for transparent plumes even when low clouds are present between the plume and the instrument. Our findings here show that, even though the maximum measured VCD decreases beneath the plume with increasing cloud opacity, thickness, and SZA (Figure 3.3), the resulting peak broadening for transparent plumes leads to CSBs that agree within ±25% of the theoretical input value, in most cases (Figure 3.4). Furthermore, we show that while there may initially be a decrease in CSBs with increasing cloud AOD, peak broadening eventually leads to larger CSBs that again approach the theoretical value (Figure 3.4). This suggests that non-ideal atmospheric conditions specifically due to low cloud presence create errors in CSB only to a point and in most circumstances are not contributing substantially (>25%) to total error, as long as the overhead volcanic plume is sufficiently transparent.

Our results also indicate that the location of the ghost plume can be predicted quite accurately from simple geometrical considerations about the position of the sun and difference in altitude between the plume and underlying cloud. For the scenarios we inspected we found lateral displacements of ~700 m and ~2000 m for SZA of 30° and 60°, respectively, and a difference in altitude of 1600 m; which agrees quite well with the prediction of Eq. 3.4.

Full error estimates in the construction of SO_2 emission rates consist of uncertainties in several broad categories including wind speed, instrumental error, measurement geometry, and atmospheric

scattering (Galle et al., 2010). Both atmospheric scattering and wind speed are identified as large components of error in total SO_2 emission rate calculations; our models address some of the effects caused by poor atmospheric conditions. Our scenarios B, D, and F with an opaque plume (plume AOD = 4) show a substantial underestimation of the CSB and demonstrate that atmospheric scattering is a large contributor to error in emission rate measurements under opaque plume and low cloud conditions (Figure 3.4). Our scenarios A, C, and E, however, find that conditions with a transparent plume and opaque cloud between the plume and the DOAS telescope yield acceptable uncertainties (within ±33% for all scenarios). This suggests that DOAS measurements can be collected under low-cloud conditions and still produce acceptable measurements. We would then suggest that opaque low clouds by themselves are not a large contributor to total SO_2 emission rate error and that definitions of poor atmospheric conditions could be narrowed to only include those with an opaque plume.

"Dampening" in the translucent plume case may be due to dilution caused by the cloud. Increased opacity of the plume counteracts this effect by multiple-scattering inside the plume. For the opaque plume case the dampening is worst probably because less photons from the plume actually reach the instrument as they become scattered away or extinct in the plume.

Determining plume transparency when the plume is obscured by low clouds will rarely be possible and will require external resources such as fortuitously located webcams and/or pilot reports. An incorrect assessment of plume transparency may also lead to errors in measurement geometry based on the misattribution of the true plume location which would then further impact the total error in SO_2 emission rate. All scenarios examined in our models where the sun is not directly overhead in conjunction with an opaque cloud layer between the DOAS instrument and plume cause modification of plume cross sectional shape and a majority lead to ghost plume emergence. Unexpectedly, ghost plumes are seen even at low cloud AODs of 1 in thinner cloud layers (200 m), which suggests that plume shape modification may begin to occur under a multitude of commonly occurring real-world situations. These low cloud AOD scenarios are common in otherwise optimal urban and marine conditions, where low-lying haze or aerosolized sea salt may generate ambient AOD values of 0.1 – 0.4 at the wavelengths considered for DOAS retrievals of SO_2 (Mulcahy et al., 2008).

3.4.2 Recommendations

Considering our model results, we recommend the following practices for collecting DOAS-traverse measurements of volcanic SO_2 emission rates for volcano monitoring. First, error should be minimized by ensuring that measurements are collected at least 1 km from the vent to increase the chance of low plume opacity. Measurements with a low cloud layer and transparent plume may be increasingly common further from the volcanic edifice as the plume dilutes in the atmosphere, generally at distances over one kilometer (Matsushima and Shinohara, 2006). Secondly, DOAS traverses recorded with low

cloud cover should extend beyond any SO_2 signals for several km to be able to capture and include any potential ghost plumes. For example, in our scenario of a plume ~1 km above the cloud layer we need to extend our traverse up to 1 – 2 additional kilometers perpendicular to the plume in order to properly capture background and any potential ghost plumes. In the case of conditions with scattered clouds beneath the plume, extending the traverse may provide an opportunity to visually constrain overlying plume conditions. In order to ascertain the degree of plume opacity during traverses, acquisition of complementary visual observations through webcam or unmanned aircraft systems (drone) imagery as described above is desirable in order to assign an approximate level of uncertainty to resulting emission rate measurements. If no resources exist to confirm the opacity of the plume during the traverse, the full list of shapes from our six scenarios (Figure 3.3) may also be used as a guide to ascribe a level of uncertainty (Figure 3.4) and help characterize overlying atmospheric and plume conditions of DOAS traverses from real-world scenarios (also see our case study below). Thirdly, simple judgement of the shape of the plume, the appearance of an image of the main plume and the relative location of the sensor, plume and sun should be used to determine if a ghost-plume may be present or not.

3.4.2.1 Automation of plume detection

As discussed above, selecting plume horizontal limits and SO_2 baseline values is somewhat subjective and different analysts likely use different guidelines to make these choices that ultimately impact the derived SO_2 CSB and emission rates. Our modeling study shows that, if we simply integrate the SO_2 column density along the entire traverse, we obtain approximately a 10% overestimate of the SO_2 CSB for optimal atmospheric conditions (transparent plume, no clouds). This is mostly caused photons that pass through the plume and are then scattered beneath it towards the instrument. These photons carry the absorption signature of SO_2 in the plume but, depending on the SZA, are detected away from the plume and lead to a slightly overestimated CSB. This effect is analogous to but less pronounced than the ghost plume effect and occurs even in cloud-free conditions due to scattering on air molecules rather than cloud droplets.

If we apply the plume selection criteria we introduced above, the SO_2 column densities along a traverse are adjusted for a small but non-zero baseline SO_2 VCD (typically in the range of $2 – 4\times10^{15}$ molecule cm^{-2} during optimal conditions). Low cloud conditions with moderate to high (> 4) AOD can further increase the automatically derived baseline VCD to $6 – 11 \times 10^{15}$ molecule cm^{-2} due to multiple scattering within the cloud layer causing a further broadening of the measured peak. Use of our method for automatically defining the plume limits is recommended, as we have found that our automation of the selection process appears to properly identify a reasonable background value and plume extent, such that the calculated CSB is within reasonable margins (±25%) of the theoretical value. In our analyses without an adjusted baseline under high cloud AOD and SZA scenarios, the CSB was at times overestimated by

upwards of 100%. Secondly, as SZA increases, an amount of skewness is introduced such that the plume is no longer symmetrical on each side. At high SZA values in optimal atmospheric conditions, the degree of skewness becomes more elongated such that the background VCD appears higher several kilometers beyond the plume on the side opposite the solar position. Because of the nature of these shapes, ~10% error was found in our ideal traverse CSBs depending on the thresholds and averaging which we selected for baseline determination. Both the challenge of manually selecting an appropriate baseline and/or manually defining plume limits indicate the opportunity for user-induced error in SO_2 emission rate calculations depending on what criteria are used for CSB determination.

For a plume SO_2 VCD of 2.5×10^{17} molecule cm^{-2} at plume center, a dVCD/dx threshold of 1×10^{13} (molecule cm^{-3}) to determine plume limits was found to be sensitive enough to accurately capture small features which should be considered part of the plume or ghost plume while not capturing noise. Additionally, averaging 5 adjacent consecutive SO_2 column measurements was found to reduce the model photon noise to below 1×10^{13} (molecule cm^{-3}), even for the extreme scenarios (e.g. Cloud AOD = 20, scenario F). Other threshold values may be more appropriate for differing sets of real-world data depending on the signal/noise ratio achieved during the respective measurement.

3.5 Case Study: Cumbre Vieja, 2021

3.5.1 DOAS retrieval and atmospheric conditions

In this section, we aim to compare real-world measurements of a volcanic plume and ghost plume to several simulated model scenarios and attempt to derive a best estimate of the encountered conditions and SO_2 emission rate. We use a DOAS dataset acquired during the 2021 eruption of Cumbre Vieja (Albertos et al., 2022), Canary Islands, Spain (51.78887° N, 178.79368° W; 1573 MASL), which shows what appears to be a ghost plume in the measured SO_2 VCD curve (Figure 3.5). DOAS spectra were collected by boat traverse at an azimuth (AZ) of 340° on November 27th between 11:50 – 12:30 UTC by staff of Instituto Volcanológico de Canarias (INVOLCAN). The solar position was approximately behind the ship for the entirety of the traverse at an AZ of ~160° and an SZA of ~55°. Measurements were collected over a distance of 16 km using a vertically oriented mobile-DOAS instrument, similar to that described in Galle et al. (2003), placed on the front of the ship (Figure 3.5). The instrument employs a telescope with a single quartz lens focusing incident light on the entrance of a quartz optical fiber bundle, a Hoya U-330 bandpass filter with long-wave cutoff at 330 nm, a grating spectrometer from Ocean Insight with 0.6 nm spectral resolution, and a GPS receiver. The resolution of the spectrometer was 0.6 nm and the time resolution was 1 second.

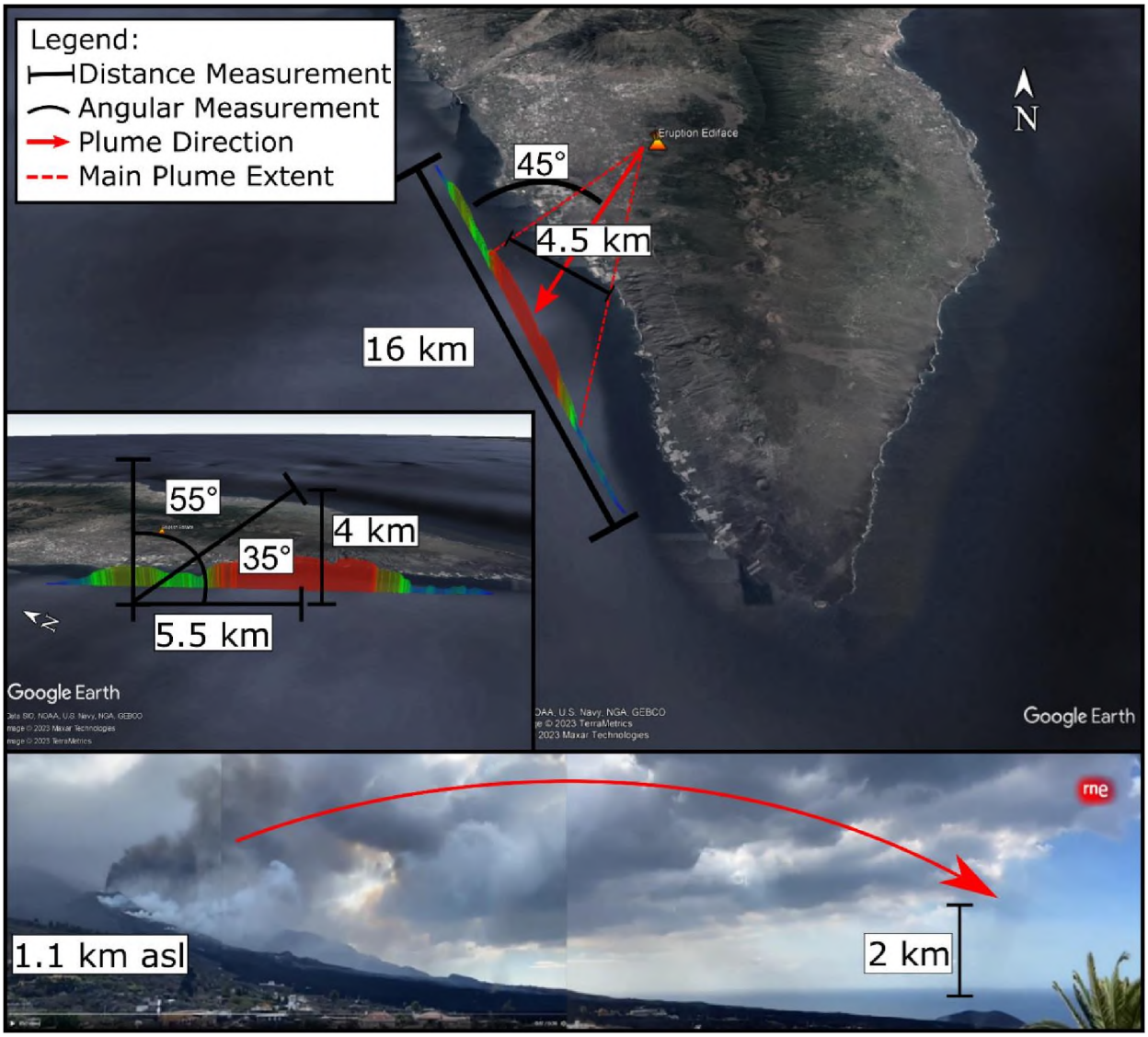

Figure 3.5 (Top) Oblique view of the November 27, 2021 Cumbre Vieja boat traverse with traverse distance, plume direction, extent, and width labeled in addition to angle between traverse and plume. A geometric solution to plume altitude based on the distance between the main plume and ghost plume and the known SZA parallel to the traverse (55°) is depicted in the inset. (Bottom) Panoramic photograph compiled from webcam video collected earlier in the day of the traverse reported and published by Radio Nacional (November 27, 2021). The approximate plume direction is indicated with the red arrow showing an ash and gas-rich plume gently rising from a flank vent at approximately 1.1 km a.s.l. and carried to the southwest by winds.

No photos were collected during the traverse, so we instead rely on complementary observations to describe atmospheric conditions. Webcam imagery collected from the morning of the traverse shows an opaque plume gently rising above a 1.1 km high vent and becoming increasingly transparent with distance. A thin layer of sea-level atmospheric haze can be seen extending out into the ocean below the plume. Romero et al. (2022) notes that during periods of the 2021 Cumbre Vieja eruption a significant

quantity of lava flowed into the ocean, which typically produces lava haze, or "laze" (Edmonds and Gerlach, 2006), which can increase atmospheric AOD at ground level. TROPOMI satellite imagery for that day (Theys et al., 2017) shows a single plume in a location SSW of the volcano consistent with the location estimated by the boat traverse.

For use in this study, traverse data were processed using the fit routines implemented in the DOASIS software (Kraus, 2006) and using a custom MATLAB code for spatial analysis of mobile DOAS data (mDOAS, as used by Kern et al., 2020). The DOAS fit was performed between 320 – 324.5 nm with absorption cross sections for SO_2 (Bogumil et al., 2003), O_3 (Vandaele et al., 2009), and a Ring-effect correction (Grainger & Ring, 1962). This atypical narrow wavelength range was chosen to avoid saturation effects from strong SO_2 absorption (e.g., Kern et al., 2010, Elias et al., 2018, Fickel et al., 2017) and hot pixels in the spectrometer's CCD detector, and to better facilitate comparisons to output from our monochromatic radiative transfer model (see following sections).

3.5.2 DOAS results

The DOAS retrieval yielded SO_2 VCDs of up to ~7,000 ppm•m SO_2 (1.75×10^{19} molecule cm^{-2}) and a potential ghost plume with VCDs of ~3,000 ppm•m (7.5×10^{18} molecule cm^{-2}) to the northwest of the main plume. The traverse intersected the plume at an angle of 45°, indicated by a source direction calculated with mDOAS at an AZ of approximately 25° and GPS tracks of the boat traverse at a bearing of AZ 340° (Figure 3.5, Top). The plume width along the traverse was approximately 6.5 km, which corresponds to a 4.5 km width normal to the wind direction. The potential ghost plume has a width of ~4 km along the transect. There is some variability in the retrieval VCSs which creates some ambiguity in determining the exact distance between the main plume and ghost plume peak, but the distance appears to be somewhere between 5.5 – 7 km.

3.5.3 Model comparisons

3.5.3.1 Model initialization

In total, four model scenarios were investigated in an attempt to best reproduce the SO_2 VCDs measured along the described traverse. All four model scenarios share the same plume, solar, and traverse dimensions. All simulations were conducted over a traverse path of -10 to +16 km with a measurement every 100 m. In order to replicate the real-world traverses in our model space, we simulated a traverse heading at an azimuth of 315° relative to a plume centered along the Y-axis (equivalent to North–South) (i.e. intersecting the plume at 45°) and define our instrument X (equivalent to East–West) and Y coordinates as:

$$Position_{Final}(X,Y) = Position_{Initial}(\sin 45° \times path, \cos 45° \times path) \qquad \text{(Eq. 3.6)}$$

where *path* describes instrument location for each 100 m traverse increment. The CSB of the simulated traverses and real-world data were calculated using the first derivative of VCD over distance in the same manner as described in our methods section, except we used a higher threshold value of ± 2.5 $\times 10^{14}$ (molecule cm^{-3}) to select our plume limits to accommodate the much larger Cumbre Vieja SO_2 VCD values.

Based on the known geometry for the transect and detected plume width, we model a plume width of 4.5 km (Figure 3.5 Top). The exact plume dimensions are not known but, as volcanic clouds tend to spread laterally more efficiently than they do vertically (Sparks et al., 1997; Bursik, 2001), we assume a rectangular plume cross section for the purposes of our modeling study. An AOD of 0.5 for the atmosphere above the ocean (marine layer) during the eruption (Filonchyk et al., 2022) were assumed for the lower laze layer and an in-plume AOD of 0 was used to simulate observations of a plume that appeared largely transparent down-wind of the vent. Finally, we simulate the radiative transfer at 320 nm to be consistent with the fit window used in the DOAS analysis of these measurements.

SO_2 emission rates are calculated from DOAS measurements by multiplying the SO_2 CSB with the perpendicular wind speed. Here, we use ERA5 wind reanalysis product provided by the European Center for Medium-Range Weather Forecasts (ECMWF) queried for the traverse location. Wind speeds between 2 and 5 km altitudes were all within 12 ± 1 m s^{-1} and directions were within ± 2° of each other. To concentrate on the effects of radiative transfer on our measurements, we consistently apply a single value of 12 m s^{-1} at AZ 18° to calculate emission rates for the real-world data and all model scenarios presented below.

3.5.3.2 Scenario A (2 km plume altitude with no laze)

The purpose of scenario A is to examine the radiative transfer effects of a transparent plume and atmosphere following a plume altitude of 2 km with an approximate vertical thickness of 1 km estimated from webcam videos taken near the time of the traverse. For this scenario a modeled plume SO_2 VCD of ~6,000 ppm•m (1.5×10^{19} molecule cm^{-2}) is used across the entirety of the layer corresponding to the approximate average SO_2 concentration through the main plume in the real-world data. This value was selected to best reproduce the SO_2 VCDs measured along the main plume in our model space.

For scenario A, we find the modeled plume detection is relatively symmetrical and captures the extent and magnitude of the real-world main plume. No ghost plume is apparent, and the shape of the real-world traverse is not replicated by our model (Figure 3.6A, dashed blue line). The theoretical and simulated SO_2 emission rate from this scenario are 79 and 77 kt day^{-1}, respectively, both slightly less than what is measured in the real-world traverse. An underestimation of real-world parameters is expected

under the modeled parameters given that a ghost plume is not expected to occur without a condensed atmospheric layer between the plume and clouds.

3.5.3.3 Scenario B (2 km plume altitude with an AOD = 0.5 laze)

For scenario B, we now examine the radiative transfer effects of a transparent plume with a layer of laze present. To examine how even a minor amount of atmospheric condensation may impact measurements, we assume the same parameters as scenario A with 400 m thick layer of AOD = 0.5 laze inserted at ground level.

Scenario B provides a slightly improved match with respect to the real-world main plume extent and shape. With the insertion of a condensed layer, we also begin to see a ghost plume emerge as a tail in the direction of the real-world traverse's "ghost plume" detection (Figure 3.6A, blue line), however the ghost plume is still not perfectly captured in extent and magnitude. The input SO_2 VCD and theoretical CSB is the same as scenario A, but the simulated emission rate is marginally lower at 73 kt d^{-1} (Table 3.2). This value is 21% lower than the DOAS measurements that ignore cloud and aerosol scattering. The discrepancy appears to stem from an inability to fully reproduce the secondary ghost plume measured to the north of the main peak. This mismatch in shape indicates that scenario B fails to describe the real-world situation completely and leads us to explore other atmospheric conditions that might lead to a better match in measured plume shape (see scenarios below).

Another consequence of the parameters we examine for this scenario is the production of a ghost plume which is partially within the margins of the main plume. This phenomenon appears to be related to the low plume altitude, large width of the plume, and steep solar position near the horizon. The "stacking" of a ghost plume is evidenced by higher VCD values than in scenario A, indicating that ghost plume need not be separate from the main plume under certain conditions. In the case of the real-world data, we observe a fully separated ghost plume which suggests that a higher altitude modeled plume would provide a better fit.

3.5.3.4 Scenario C (4 km plume altitude with an AOD = 0.5 laze)

In an attempt to better capture the secondary ghost plume on the north end of the measured traverse, we explored the influence of plume altitude on the simulations with a layer of AOD = 0.5 laze inserted at ground level. Here, we consider a plume centered at a 4 km altitude based on a geometric solution from the known solar geometry and the distance between the ghost plume and main plume (Figure 3.5 Top Inset). For high plume altitudes, the effects of light dilution on SO_2 VCD is expected to be significant such that reproducing the real-world measurements required initializing the model with a higher SO_2 VCD. We attempted to find appropriate model input SO_2 VCD concentrations to match real-world measurements by iteratively measuring model output SCD for a range of concentrations at 4 km

plume altitudes for the given solar geometry and plume dimensions of the real-world transect. Because of the increasing opacity of the modeled plume under high SO_2 VCDs, we were not able to achieve a modeled plume output that matched the real-world VCD, and instead optimized the model input such that the simulations returned the highest possible SO_2 VCDs (~11,000 ppm•m, 2.75×10^{19} molecule cm^{-2}).

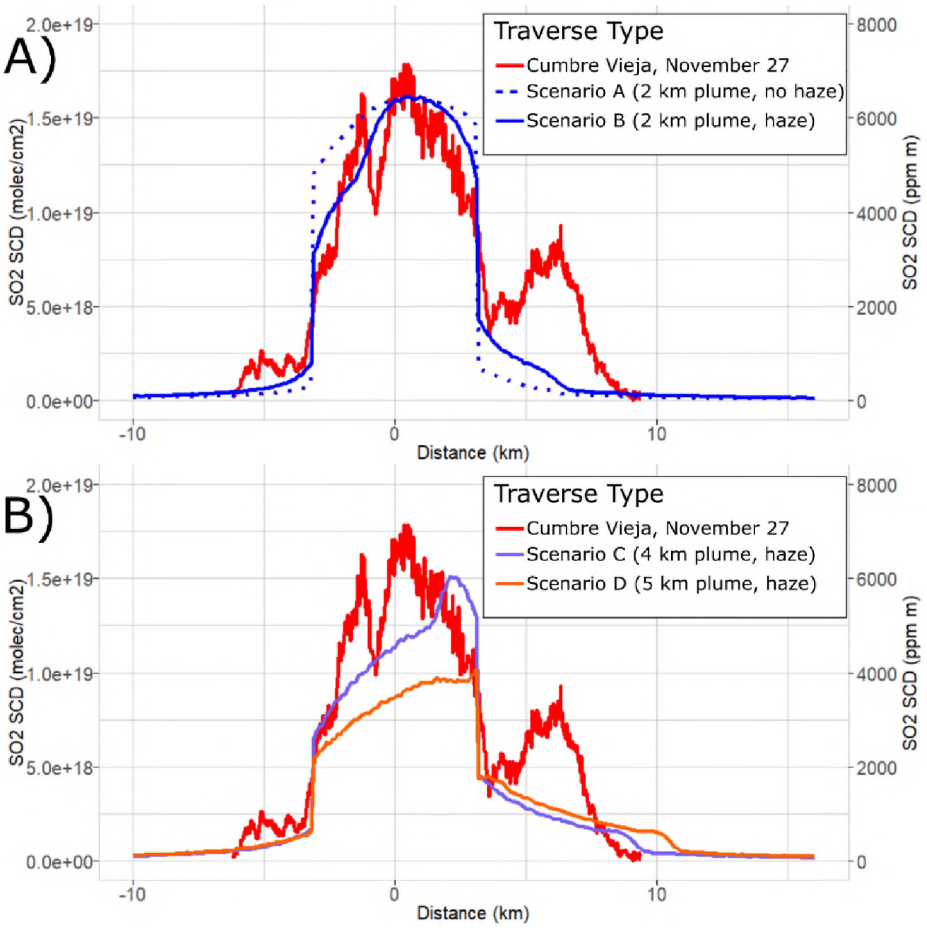

Figure 3.6 Simulated DOAS traverses plotted against real-world DOAS measurements from Cumbre Vieja volcano collected on November 27, 2021. Notice that the shape of the distribution of retrieved VCD shows features of a ghost plume, which would be expected given the measurement conditions. (A) Rectangular 4.5 × 1 km plume at 2 km altitude containing a VCD of ~6,000 ppm• m SO_2 plotted with a 400 m without a layer of laze at ground level (AOD = 0; dashed blue line) and with an AOD = 0.5 layer of laze at ground level (solid blue line) against the real-world measurements (solid red line). (B) Modeled traverses for the same plume parameters as in A but now shown for plume altitudes of 4 and 5 km. Scenarios C and D both contain a layer of laze (AOD = 0.5) present above ground level and a column density of ~10,000 ppm• m.

For scenario C we find that the resulting SO_2 VCD curve better replicates the extent and area of the ghost plume detection in the real-world dataset but performs worse than scenario A and B at replicating the area of the main plume (Figure 3.6B, purple line). Under a high plume geometry, we produce an SO_2 emission rate of 67 kt d^{-1} (Table 3.2), which is 28% lower than what is indicated from the

real-world dataset. The discrepancy within this scenario appears to stem from an inability to fully reproduce the magnitude of the main plume VCD at high plume altitude. The plume width and solar geometry with the plume altitudes in scenario C still results in a stacking effect of the main plume and ghost plume such that there is not a distinct ghost plume peak separate from the main plume. Thus, we attempt to explore the upper bounds of a geometric solution to plume altitude in an attempt to separate these features.

3.5.3.5 Scenario D (5 km plume altitude with an AOD = 0.5 laze)

For scenario D, we shift the plume altitude to 5 km to examine if a separated ghost plume can be reproduced. To accomplish this, we use the upper limits of a reasonable geometric solution based on the distance between the main plume and ghost plume to model a plume centered at 5 km altitude. We also employ the same iterative procedure of increasing plume SO_2 VCDs as scenario C to address the issue of light dilution. For this plume altitude we find that a VCD of ~11,000 ppm•m (2.75×10^{19} molecule cm^{-2}) is most appropriate.

At high altitudes, our simulation in Scenario D is subject to the largest amount of light dilution and performs worse than all previous scenarios at simulating the VCD of the main plume. Light dilution is most extreme of all scenarios considered for this study, so the resulting emission rate is also the lowest and provides the worst match to the real-world data with an underestimation of 41% (Table 3.2). The magnitude SO_2 measured in the main plume is the lowest of all scenarios but the main plume now appears to not contain a stacked ghost plume. The magnitude of the ghost plume is higher than other scenarios, but still fails to perfectly match the real-world dataset (Figure 3.6B, orange line). Additionally, the extent of the ghost plume is kilometers beyond the margins of the real-world traverse. In this case our mismatch of the ghost plume extent would signify that a lower plume altitude is most probable.

Table 3.2 Simulated or measured parameters and SO_2 emission rate (kt day^{-1}) derived from those values

Scenario	Model Input Plume VCD (molec cm^{-2})[1]	Max Measured or Simulated SCD (molec cm^{-2})[2]	Model Input Cross Sectional SO_2 Burden Along Traverse (molec cm^{-1})[3]	Cross Sectional SO_2 Burden Along Traverse (molec cm^{-1})[4]	Model Input SO_2 Emission Rate (kt day^{-1})[5]	Measured or Simulated SO_2 Emission Rate (kt day^{-1})[6]	Relative to Conventional Method (%)[7]
Cumbre Vieja, November 27th traverse	N/A	1.78×10^{19}	N/A	1.12×10^{25}	N/A	92	N/A
Scenario A (2 km altitude plume, no laze)	1.5×10^{19}	1.52×10^{19}	9.55×10^{24}	9.37×10^{24}	79	77	85
Scenario B (2 km altitude plume with laze)	1.5×10^{19}	1.65×10^{19}	9.55×10^{24}	8.87×10^{24}	79	73	85
Scenario C (4 km altitude plume with laze)	2.75×10^{19}	1.2×10^{19}	1.75×10^{25}	8.09×10^{24}	144	67	156
Scenario D (5 km altitude plume with laze)	2.75×10^{19}	8.73×10^{18}	1.75×10^{25}	6.64×10^{24}	144	55	156

1: Defined as the input SO_2 VCD within the McArtim model space designed to best optimize for real-world measurements.
2: Defined as the output SO_2 VCD within the McArtim model space or the approximate average value of the main plume VCD in the real-world dataset.
3: Defined as the theoretical cross sectional burden based on the known input SO_2 VCD.
4: Defined as the measured or modeled CSB based on the known input SO_2 VCD or real-world traverse VCD.
5: Defined as the theoretical SO_2 emission rate based on the model input CSB
6: Defined as the measured or modeled SO_2 emission rate based on the model output or real-world traverse CSB
7: Defined as the ratio of the model input emission rate CSB to the measured CSB in real-world data

3.6 Ghost plume effects in real-world data

Our simulated traverses show that plume modification due to the presence of atmospheric laze (or haze) with low AOD values may be prevalent and have a substantial impact on retrieved SO_2 VCD values or derived emission rates depending on the plume elevation and solar geometry. Marine layer AOD values of 0.5 have been measured during the Cumbre Vieja eruption (Filonchyk et al., 2022) and are within the range for marine layers in the North Atlantic Ocean, for which ambient AOD may vary between 0.0 – 0.8 depending on the contribution of salt spray, dust, and anthropogenic pollutants (Mulchay et al., 2008; 2009). Similar AOD values of up to 0.8 may also be found on land in some urban environments (Zhang et al., 2020). Despite plume shape modification likely occurring with the presence of laze, we have demonstrated that the resulting SO_2 CSBs from these traverses with low-AOD laze will still be approximately equivalent to counterparts without laze, if plumes are transparent. This suggests that future traverses in the presence of haze or laze may be conducted with little concern, but measured plumes may be broader than the actual plume width. Because of this plume broadening in the presence of laze, a small apparent offset to the plume center may occur which could potentially contribute additional emission rate uncertainty when considering the actual versus measured plume center and wind direction. It is likely that the largest source of underestimation and uncertainty in our measurement is the effect of light dilution, as demonstrated by the increasing underestimation in plume SO_2 CSBs as we sequentially raised the plume altitude in scenarios C and D.

At plume altitudes of 4 and 5 km we were not able to reproduce the magnitude of the measured main or ghost plume SO_2 VCD in our model space, suggesting that the real-world plume was likely not as high as assumed in these scenarios, and that other processes must have been responsible for the pronounced secondary plume to the north of the main peak (see alternative scenario below. The problem of light dilution for plumes at high altitude has been noted in Kern et al. (2010), Varnam et al. (2020), and Galle et al. (2023), among others; the problem with DOAS measurements at high SO_2 concentrations has been noted under similar conditions at Kilauea Volcano (Elias et al., 2018), Aso Volcano (Mori et al., 2006), and has been studied with simulations using McArtim (Kern et al., 2010). Our inability to replicate the exact magnitude of the measured SO_2 VCD from the Cumbre Vieja dataset with a realistic plume morphology suggests that other factors not accounted for in our model may be at play. Factors such as complex plume morphology, non-homogenous chemical distribution of SO_2 within the plume, and the potential of multiple SO_2 sources or plumes could be preventing us from fully replicating the real-world observations in model space. Notwithstanding, our ability to approximate the CSB of the real-world traverse with simple geometric and atmospheric assumptions demonstrates the strength of modeled traverses in accurately representing associated inaccuracies.

Further challenges to constraining the plume geometry include the large uncertainty in estimating plume altitude from webcam imagery and the fact that the available imagery is not temporally coincident with the time of the traverse. Even with these challenges, we find that the ghost plume width for a modeled plume between 2 – 4 km altitude agrees with the measured Cumbre Vieja ghost plume width (Figure 3.6B). Satellite observations from earlier explosive phases of the eruption suggest that the plume frequently reached an altitude of 6 – 8 km (Filonchyk et al., 2022) though explosive activity had largely ceased by November 27 (Romero et al., 2022), so it is feasible that our measured plume could represent a lower altitude consistent with scenarios C and D. At plume altitudes of 2 – 4 km, the ghost plume manifests within the extent of the main plume, unlike what was observed in the DOAS transect. This would suggest that the true altitude of the plume is higher than what we have assumed or more likely that the plume shape is more geometrically complex than what was modeled here.

3.6.1 SO_2 plumes at multiple altitudes

An alternative explanation for the apparent ghost plume measured at Cumbre Vieja on November 27 may be that SO_2 in this traverse was captured from either a bifurcated plume or multiple SO_2 emission sources. In the case of a bifurcated plume, atmospheric instability or internal plume mechanisms may split an initially intact plume (Ernst et al., 1995) to create two distinct, separate lobes. If we have erroneously interpreted our traverse as a main plume and ghost plume instead of a plume with higher amounts of SO_2 and a detached lobe with less SO_2, then the resulting CSB could appear to be similar in shape to a main plume and ghost plume. Similarly, if an additional source was emitting SO_2, potentially from the flank fissure, in addition to the main vent, two somewhat distinct SO_2 plumes may be seen in traverse measurements of SO_2 VCD. Elias et al. (2018), Kern et al. (2020), and Lerner et al. (2021) documented that significant quantities of SO_2 were released from rifts and lava flows in addition to the main vent during the 2018 Kilauea eruption, so it is likely that some quantity of SO_2 was also emitted during the Cumbre Vieja eruption at or near ground level. Local news reports the day of the traverse in *El Confidencial* (2021, November 28) indicate elevated SO_2 at ground level at Cumbre Vieja, however the concentration of measured ground-level SO_2 (724 $\mu g\ m^{-3}$) would require an unrealistic thickness of laze (e.g., > 10 km) to match the observed ghost plume VCD (~3,000 ppm•m). This suggests that SO_2 was present at multiple altitudes, with the real-world measurement capturing SO_2 from a plume at a high altitude in addition to SO_2 emitted at a lower altitude producing what we had been referring to as laze. The additional presence of SO_2 in a lower laze layer or a secondary low-altitude source of SO_2 would also contribute to higher recovered VCDs and explain our inability to match real-world VCD values in the main plume traverse.

3.6.2 Comparison to literature emission rates

Overall, the emission rates derived from the real-world SO_2 measurements and our simulated SO_2 VCD data are higher than but within realistic margins for existing measurements reported for the 2021 Cumbre Vieja eruption. Ground-based traverses by Albertos et al. (2022) suggest SO_2 emission rates over 30 kt day^{-1}, decreasing towards the end of the eruption on December 12, 2022. Satellite analysis in Filonchyk et al. (2022) using TROPOMI suggests SO_2 emission rates up to ~55 kt day^{-1} at the height of eruption in early to middle October, however their studied period ends on October 16 and does not overlap with our observations. In total, the maximum reported emission rates during the period when eruptive plumes were also highest approach the values simulated for a plume at 5 km altitude (scenario D) and suggest that the true emission rate during this eruption may well have been underestimated in previous studies.

3.6.3 Likely plume scenario

We find that none of our modeled scenarios adequately replicate both the magnitude of the measured SO_2 VCD and the size or shape of what we have chosen to interpret as a ghost plume in the real-world observations. While we have chosen to discuss several potential scenarios, the true plume conditions which produced the observed cross section at Cumbre Vieja may involve some combination of a geometrically complex plume with multiple SO_2 sources, a main plume at an elevation between 2 – 5 km, and a secondary SO_2 source or laze layer at ground level. All these factors would allow for a sufficiently separated secondary ghost plume while not hindering our ability to capture very high VCDs in the main plume due to light dilution. Ultimately, this dataset represents an example of a situation in which conventional DOAS retrievals may fail due to very high VCD values encountered in the main plume. However, the many unknown atmospheric parameters make it difficult to provide robust corrections for the complex radiative transfer using the model simulations. While we can effectively reproduce the main characteristics of the measurement, we are not able to capture all details in a single model scenario, likely due to the much more complex plume morphology of the real-world measurement. Still, the presented model scenarios give an idea of the range of SO_2 emission rates which can be considered consistent with the measurements (85 – 156 kt d^{-1}, see table 3.2), as well as an understanding of the measurement uncertainty.

3.7 Conclusions

The emergence of ghost plumes is a known, but until now relatively poorly studied phenomenon in remote sensing of volcanic SO_2 plumes. While it is commonly accepted that different atmospheric conditions may impact SO_2 column density retrievals from individual DOAS measurements, we have expanded on the current body of knowledge to constrain the influence of solar zenith angle and below-

plume cloud AOD on SO_2 vertical column density (VCD) measurements. We have presented a visual and quantitative guide for how varying low-cloud atmospheric conditions modify plume shapes and generate ghost plumes in DOAS traverses. Furthermore, we have demonstrated that, for concentrations of SO_2 commonly measured during persistent degassing, a below-plume cloud will modify the shape of a plume VCD profile along the traverse, but the resulting cross-sectional burden will generally agree within ± 25% of the input value if the plume AOD is < 1. Our research demonstrates an application of the McArtim model to simulate DOAS traverses of simple volcanic plumes; however, due to the complex nature of real-world plumes, our simulations may not perfectly match real-world observations. We have also shown that modification of plume shapes due to low clouds may be more common than previously thought and provide real-world observations and simulations for a rather extreme case observed during the 2021 Cumbre Vieja eruption. Our findings indicate that DOAS traverse measurements made under suboptimal atmospheric conditions can still yield relatively accurate SO_2 emission rate measurements for volcano monitoring purposes.

3.8 Acknowledgements

We would like to thank Bo Galle for constructive feedback and José Barrancos Martínez for helping to collect the Cumbre Vieja DOAS measurements. This work was partially funded through U.S. Geological Survey Cooperative Agreement No. G21AC10384. SA was funded through a grant (Dr. No. 149/18) from the Swedish National Space Agency. Any use of trade, product, or firm names is for descriptive purposes only and does not imply endorsement by the United States Government.

3.9 References

Albertos, V.T., Recio, G., Alonso, M., Amonte, C., Rodríguez, F., Rodríguez, C., Pitti, L., Leal, V., Cervigón, G., González, J., Przeor, M., Santana-León, J.M., Barrancos, J., Hernández, P.A., Padilla, G.D., Melián, G.V., Padrón, E., Asensio-Ramos, M., and Pérez, N.M. (2022). Sulphur dioxide (SO2) emissions by means of miniDOAS measurements during the 2021 eruption of Cumbre Vieja volcano, La Palma, Canary Islands. *EGU General Assembly 2022*, Vienna, Austria, 23–27 May 2022, EGU22-5603. doi:10.5194/egusphere-egu22-5603.

Arellano, S., Galle, B., Apaza, F., Avard, G., Barrington, C., Bobrowski, N., Bucarey, C., Burbano, V., Burton, M., Chacón, Z., Chigna, G., Clarito, C.J., Conde, V., Costa, F., De Moor, M., Delgado-Granados, H., Di Muro, A., Fernandez, D., Garzón, G., Gunawan, H., Haerani, N., Hansteen, T. H., Hidalgo, S., Inguaggiato, S., Johansson, M., Kern, C., Kihlman, M., Kowalski, P., Masias, P., Montalvo, F., Möller, J., Platt, U., Rivera, C., Saballos, A., Salerno, G., Taisne, B., Vásconez, F., Velásquez, G., Vita, F., and Yalire, M. (2021). Synoptic analysis of a decade of daily measurements of SO_2 emission in the troposphere from volcanoes of the global ground-based Network for Observation of Volcanic and Atmospheric Change. *Earth Systems Science Data*, 13, 1167–1188. doi:10.5194/essd-13-1167-2021.

Deutschmann, T., Beirle, S., Frieß, U., Grzegorski, M., Kern, C., Kritten, L., Platt, U., Prados-Román, C., Puķı¯te, J., Wagner, T., Werner, B.,and Pfeilsticker, K. (2011). The Monte Carlo atmospheric radiative transfer model McArtim: Introduction and validation of Jacobians and 3D features; *Journal of Quantitative Spectroscopy and Radiative Transfer*, 112(6), 1119-1137. doi:10.1016/j.jqsrt.2010.12.009.

Edmonds, M. and Gerlach, T.M. (2006). The airborne lava–seawater interaction plume at Kīlauea Volcano, Hawai'i. *Earth and Planetary Science Letters*, 244(1-2), 83–96. doi:10.1016/j.epsl.2006.02.005.

Edmonds M., Herd R.A., Galle B., and Oppenheimer C.M. (2003). Automated, high time resolution measurements of SO2 flux at Soufrière Hills Volcano, Montserrat; *Bulletin of Volcanology*, 65(8), 578 – 586. doi:10.1007/s00445-003-0286-x.

El Confidencial (2021, November 28). El volcán de Cumbre Vieja genera una nueva colada por la ladera noreste. https://www.elconfidencial.com/espana/2021-11-28/ultima-hora-volcan-la-palma-alertan-coladas-sismicidad_3328346/. Retrieved 05/12/2023.

Elias, T., Kern, C., Horton, K.A., Sutton, A.J., and Garbeil, H. (2018). Measuring SO2 Emission Rates at Kilauea Volcano, Hawaii, Using an Array of Upward-Luuking UV Spectrometers, 2014-2017. Frontiers in Earth Science, 6(214). doi:10.3389/feart.2018.00214.

Ernst, G.G.J., Davis, J.P., and Sparks, R.S.J. (1994). Bifurcation of volcanic plumes in a crosswind. *Bulletin of Volcanology*, 56, 159–169. doi.org/10.1007/BF00279601.

Fickel, M., and Delgado-Granados H. (2017). On the use of different spectral windows in DOAS evaluations: Effects on the estimation of SO_2 emission rate and mixing ratios during strong emission of Popocatépetl volcano. *Chemical Geology*, 462, 67–73. doi:10.1016/j.chemgeo.2017.05.001.

Filonchyk, M., Peterson, M.P., Gusev, A., Hu, F., Yan, H., and Zhou, L. (2022). Measuring air pollution from the 2021 Canary Islands volcanic eruption. *Science of The Total Environment*, 849. doi:10.1016/j.scitotenv.2022.157827.

Fischer, T.P., Roggensack, K., and Kyle, P.R. (2002). Open and almost shut case for explosive eruptions: Vent processes determined by SO_2 emission rates at Karymsky volcano, Kamchatka; *Geology*, 30(12), 1059–1062. doi:10.1130/0091-7613(2002)030<1059:OAASCF>2.0.CO;2.

Galle, B., Johansson, M., Rivera, C., Zhang, Y., Kihlman, M., Kern, C., Lehmann, T., Platt, U., Arellano, S., and Hidalgo, S. (2010). Network for Observation of Volcanic and Atmospheric Change (NOVAC)—A global network for volcanic gas monitoring: Network layout and instrument description. *Journal of Geophysical Research*, 115. doi:10.1029/2009JD011823.

Galle, B., Oppenheimer, C., Geyer, A., McGonigle, A.J.S., Edmonds, M., and Horrocks, L. (2003). A miniaturised ultraviolet spectrometer for remote sensing of SO2 fluxes: a new tool for volcano surveillance. *Journal of Volcanology and Geothermal Research*, 119(1–4), 241-254. doi:10.1016/S0377-0273(02)00356-6.

Galle, B., Arellano, S., Johansson, M., Kern, C., and Pfeffer, M.A. (2023). An algorithm for correction of atmospheric scattering dilution effects in volcanic gas emission measurements using skylight differential optical absorption spectroscopy. *Frontiers in Earth Science*, 11:1088768, 1–14. doi:10.3389/feart.2023.1088768.

Grainger, J.F., & Ring, J. (1962). Anomalous Fraunhofer line profiles. *Nature*, 193(4817), 762–762. doi:10.1038/193762a0.

Kern, C., Deutschmann, T., Vogel, L., Wöhrbach, M., Wagner, T., and Platt, U. (2010). Radiative transfer corrections for accurate spectroscopic measurements of volcanic gas emissions. *Bulletin of Volcanology*, 72, 233–247. doi:10.1007/s00445-009-0313-7.

Kern, C., Lerner, A.H., Elias, T., Nadeau, P.A., Holland, L., Kelly, P.J., Werner, C.A., Clor, L.E., and Cappos, M. (2020). Quantifying gas emissions associated with the 2018 rift eruption of Kīlauea Volcano using ground-based DOAS measurements. *Bulletin of Volcanology*, 82. doi:10.1007/s00445-020-01390-8.

Kraus, S. (2006). DOASIS – A Framework Design for DOAS. PhD Thesis, University of Mannheim. 184 pages. https://www.shaker.eu/en/content/catalogue/index.asp?lang=en&ID=8&ISBN=978-3-8322-5452-0

Kunrat, S., Kern, C., Alfianti, H., and Lerner, A.H. (2022). Forecasting explosions at Sinabung Volcano, Indonesia, based on SO_2 emission rates. *Frontiers in Earth Science*. doi:10.3389/feart.2022.976928.

Lerner, A.H., Wallace, P.J., Shea, T., Mourey, A.J., Kelly, P.J., Nadeau, P.A., Elias, T., Kern, C., Clor, L.E., Gansecki, C. Lee, R.L., Moore, L.R., Werner, C.A. (2021). The petrologic and degassing behavior of sulfur and other magmatic volatiles from the 2018 eruption of Kīlauea, Hawai'i: melt concentrations, magma storage depths, and magma recycling. *Bulletin of Volcanology*, 83, 43. doi:10.1007/s00445-021-01459-y.

Mather, T.A. (2015). Volcanoes and the environment: lessons for understanding Earth's past and future from studies of present-day volcanic emissions. *Journal of Volcanology and Geothermal Research*, 304, 160-179. doi:10.1016/j.jvolgeores.2015.08.016.

Matsushima, N., and Shinohara, H. (2006). Visible and invisible volcanic plumes, *Geophysical. Research Letters*, 33, L24309. doi:10.1029/2006GL026506.

McGonigle, A.J.S., Hilton, D.R., Fischer, T.P., and Oppenheimer, C. (2005). Plume velocity determination for volcanic SO_2 flux measurements. *Geophysical Research Letters*, 32. doi:10.1029/2005GL022470.

Millán, M.M. (1980). Remote sensing of air pollutants. A study of some atmospheric scattering effects. *Atmospheric Environment*, 14(11), 1241 – 1253. doi:10.1016/0004-6981(80)90226-7.

Mori, T., Mori, T., Kazahaya, K., Ohwada, M., Hirabayashi, J., and Yoshikawa, S. (2006). Effect of UV scattering on SO_2 emission rate measurements. *Geophysical Research Letters*, 33. doi:10.1029/2006GL026285.

Mulcahy, J.P., O'Dowd, C.D., Jennings, S.G., and Ceburnis, D. (2008). Significant enhancement of aerosol optical depth in marine air under high wind conditions, *Geophysical Research Letters*, 35. doi:10.1029/2008GL034303.

Mulcahy, J.P., O'Dowd, C.D., and Jennings, S.G. (2009). Aerosol optical depth in clean marine and continental northeast Atlantic air, *Journal of Geophysical. Research*, 114, D20204. doi:10.1029/2009JD011992.

Oppenheimer, C., Fischer, T., and Scaillet, B. (2014). Volcanic degassing: process and impact. H.D. Holland, K.K. Turekian (Eds.), *Treatise on Geochemistry* (Second edition), Elsevier, 111-179. doi:10.1016/B978-0-08-095975-7.00304-1.

Platt, U. and Stutz, J. (2008). Differential Optical Absorption Spectroscopy: Principles and Applications; Springer Berlin Heidelberg

Radio National (2021, November 27). #ErupciónLaPalma | (12:00 hora) Se cumplen hoy 70 días de erupción en el Valle de Aridane. Así vemos esta mañana desde Tajuya el cono, sus emisiones y el campo de coladas. #LaPalma [video attached][Tweet]. Twitter. https://twitter.com/ArchipielagoRNE/status/1464567547701911558?s=20

Romero, J.E., Burton, M., Cáceres, F., Taddeucci, J., Civico, R., Ricci, T., Pankhurst, M.J., Hernández, P.A., Bonadonna, C., Llewellin, E.W., Pistolesi, M., Polacci, M., Solana, C., D'Auria, L., Arzilli, F., Andronico, D., Rodríguez, F., Asensio-Ramos, M., Martín-Lorenzo, A., Hayer, C., Scarlato, P., and Perez, N.M. (2022). The initial phase of the 2021 Cumbre Vieja ridge eruption (Canary Islands): Products and dynamics controlling edifice growth and collapse; *Journal of Volcanology and Geothermal Research*, 431. doi:10.1016/j.jvolgeores.2022.107642.

Theys, N., De Smedt, I., Yu, H., Danckaert, T., van Gent, J., Hörmann, C., Wagner, T., Hedelt, P., Bauer, H., Romahn, F., Pedergnana, M., Loyola, D., and Van Roozendael, M. (2017). Sulfur dioxide retrievals from TROPOMI onboard Sentinel-5 Precursor: algorithm theoretical basis. *Atmospheric Measurement Techniques*, 10, 119–153. doi:10.5194/amt-10-119-2017

Varnam, M., Burton, M., Esse, B., Kazahaya, R., Salerno, G., Caltabiano, T., and Ibarra, M. (2020). Quantifying Light Dilution in Ultraviolet Spectroscopic Measurements of Volcanic SO2 Using Dual-Band Modeling. *Frontiers in Earth Science*, 8:528753. doi:10.3389/feart.2020.528753.

Wagner, T., Warnach, S., Beirle, S., Bobrowski, N., Jost, A., Puķīte, J., and Theys, N. (2023). Investigation of three-dimensional radiative transfer effects for UV–Vis satellite and ground-based observations of volcanic plumes. *Atmospheric Measurement Techniques*, 16, 1609–1662. doi.10.5194/amt-16-1609-2023.

Williams-Jones, G., Stix, J., and Hickson, C. (2008). The COSPEC Cookbook: Making SO2 Measurements at Active Volcanoes. *IAVCEI Methods in Volcanology* 1: 121-167. doi:10.13140/RG.2.2.13728.99845.

Zhang, T., Zhao, C., Gong, C., and Pu, Z. (2020). Simulation of Wind Speed Based on Different Driving Datasets and Parameterization Schemes Near Dunhuang Wind Farms in Northwest of China. *Atmosphere*, 11(6), 647. doi:10.3390/atmos11060647.

Chapter 4 Using modeled wind speeds to estimate volcanic plume altitude with application to single-station scanning DOAS-derived SO_2 emission rates from Cleveland, Korovin and Gareloi Volcanoes, Alaska[3]

4.1 Introduction

Monitoring volcanic SO_2 emissions is an important tool for establishing long-term emission trends and identifying periods of unrest. Relative increases or decreases in SO_2 may indicate changes in underlying magmatic, hydrothermal, or conduit conditions. For some volcanoes, especially open-conduit systems during passive degassing, the SO_2 emission rate, or flux — the total mass of volcanically-sourced SO_2 degassed to the atmosphere over a time period (e.g. kg SO_2 s^{-1} or t SO_2 day^{-1}) — may vary by orders of magnitude (de Moor et al., 2017; Arellano et al., 2021). Characterizing background activity and identifying changes in SO_2 emissions that may indicate volcanic unrest requires accurate measurements at high temporal resolution over extended time periods.

Volcanic SO_2 emissions are commonly quantified via Differential Optical Absorption Spectroscopy (DOAS), an ultraviolet (UV) remote sensing technique which uses scattered sunlight as a radiation source (Platt and Stutz, 2008). This method removes broadband scattering to concentrate on narrowband absorption features through a variation of the conventional Beer-Lambert law. DOAS measurements allow calculation of the number of molecules of SO_2 within an atmospheric column, commonly referred to as column density (molecules cm^{-2}). These measurements can be collected in series along a cross section of a volcanic plume, and the integral of these measurements over the plume width (m) can be computed to determine a two-dimensional SO_2 cross sectional burden (molecules m^{-1}). The SO_2 cross sectional burden is then multiplied by wind speed and converted to mass units using the molar mass of SO_2 to calculate an emission rate (in units of tons per day [t SO_2 d^{-1}] or kilograms per second [kg SO_2 s^{-1}]) (Galle et al., 2002; Galle et al., 2010). The plume SO_2 cross section is typically measured using DOAS instruments via one of two applications: traverse or scanning, described below.

DOAS traverses are acquired by moving the DOAS instrument, installed on a vehicle, perpendicular to and below the plume to acquire upward-looking measurements of SO_2 column density (McGee, 1992; Platt and Stutz, 2008). This method has several advantages including lower errors stemming from better defined plume geometry. When performed via aircraft (e.g. Stoiber et al., 1983), the traverse method reduces light dilution because it gets closer to the plume and allows for near-coincident

[3] Kushner, D.S., Lopez, T.M., Kern, C., Lerner, A.H., Kelly, P.J., and Werner, C. (in prep). Using modeled wind speeds to estimate volcanic plume altitude with application to single-station scanning DOAS-derived SO_2 emission rates from Cleveland Volcano, Korovin Volcano, and Gareloi Volcano, Alaska.

accurate measurements of wind speed through the wind-circle method (Doukas et al. 2002; Kern and Kelly, 2023).

Scanning DOAS instruments measure SO_2 as a slant column density (SCD), defined as the concentration of SO_2 (c) integrated over the entire path length (l):

$$SCD = \int_0^L c(l)\, dl \quad \text{(Eq. 4.1)}$$

By collecting SCD measurements incrementally at set angles through a swath of sky from a fixed position, it is possible to calculate the cross-sectional burden of an intersected plume (Figure 4.1). Because scanning DOAS instruments are stationary, the scanning routine may be automated to collect measurements without a human operator, and thus can provide the type of high-frequency monitoring which has been used to identify long to short term trends in degassing through the Network for Observation of Volcanic and Atmospheric Change (NOVAC; www.novac-community.org) program (Galle et al., 2010; Arellano et al., 2021). NOVAC-monitored volcanoes all have scanning DOAS instruments collecting high-frequency measurements which are ingested into a software package for automatic evaluation of SO_2 cross sectional burdens. Real-time monitoring of emission rates within the NOVAC program uses Global Forecast System (GFS) products, a wind speed forecast provided through the National Oceanic and Atmospheric Administration (NOAA). While there are several methods used to determine the plume cross section (detailed in Kern, 2009), the NOVAC software uses the lateral integration method for real-time monitoring (Johansson et al., 2009a).

In the lateral method (Figure 4.1), a DOAS scan detecting a gas species of interest is used to determine the lateral distance of the plume start from the instrument (d_i) which is calculated from the instrument scanning position from zenith (α_i) and plume altitude (h):

$$d_i = h \cdot \tan(\alpha_i) \quad \text{(Eq. 4.2)}$$

The lateral distance is combined with subsequent DOAS scans ($\Delta\alpha$) at known step angles to determine the horizontal distance across the plume (Δd):

$$\Delta d = h \cdot \tan(\alpha_i + \Delta\alpha) - d_i \quad \text{(Eq. 4.3)}$$

Vertical column density (VCD), or the concentration of an absorbing species directly vertical from a point in space, is used for these calculations and may be converted from SCD as follows:

$$VCD = SCD \cdot \cos(\alpha) \quad \text{(Eq. 4.4)}$$

The average VCD between two scan positions (VCD_i) is expressed as:

$$VCD_i = \frac{1}{2}(SCD_i \cdot \cos(\alpha_i) + SCD_{i+1} \cdot \cos(\alpha_i + \Delta\alpha)) \quad \text{(Eq. 4.5)}$$

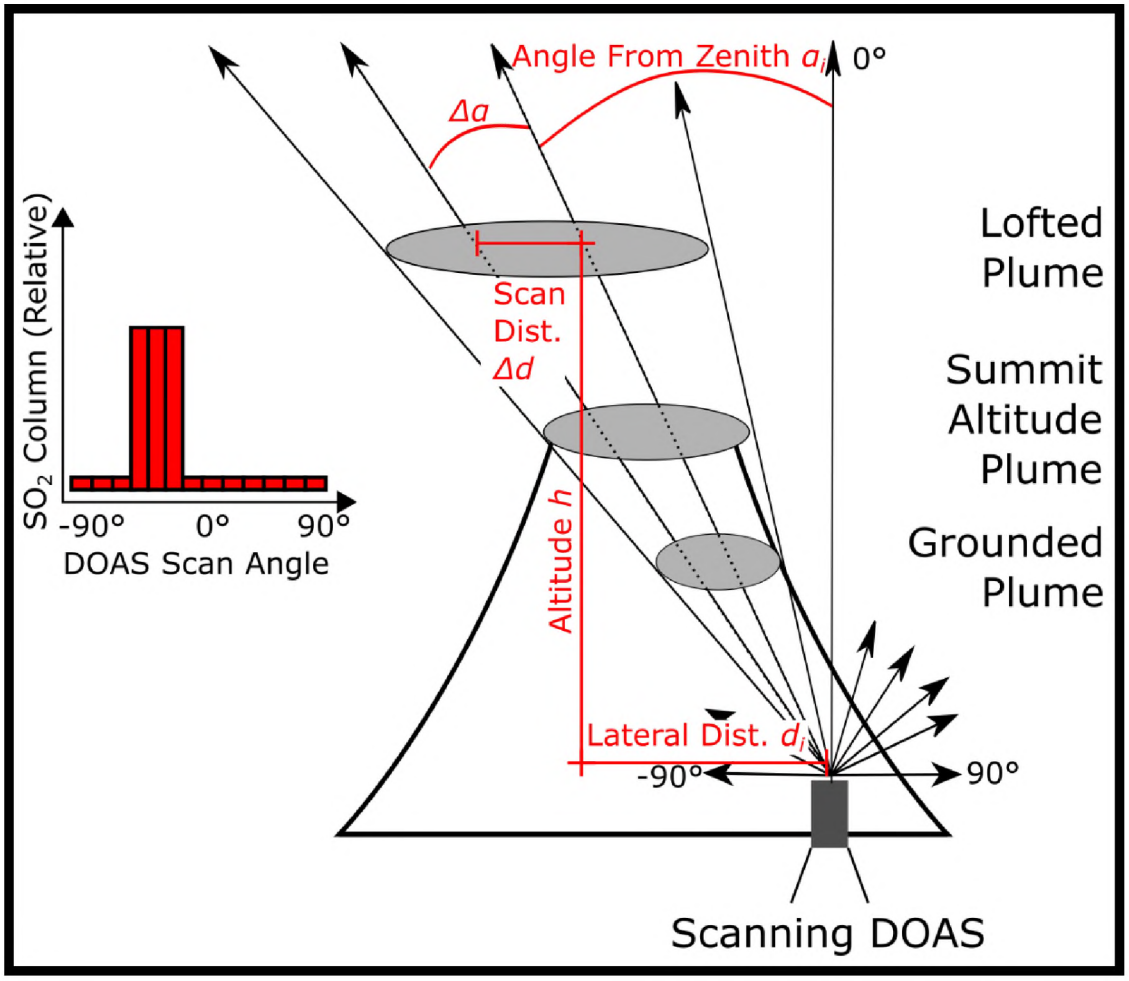

Figure 4.1 Illustration of the plume altitude problem with single scanning DOAS instruments. Each instrument viewing position from horizon to horizon, indicated by black arrows, measures the column of SO_2 in that direction. Despite having different plume widths and cross-sectional burdens, a grounded, summit altitude, and lofted plume with the same SO_2 column density along a given viewing geometry would all produce the same plume SO_2 column density at each scan position of the instrument, illustrated to the left. Important variables for use in the lateral integration method are depicted in red text.

By combining the horizontal plume distance with average vertical column densities and assuming a perpendicular intersection of the scan with the plume, the cross section of the plume (X) may then be calculated as:

$$X = \sum_{i \epsilon plume} (VCD_i \cdot \Delta d_i) \qquad \text{(Eq. 4.6)}$$

Finally, an emission rate (ϕ) can be obtained by multiplying the wind speed (v) at plume altitude by the cross section:

$$\phi = X \cdot v \quad \text{(Eq. 4.7)}$$

One major complication of the lateral integration method arises from the dependence of Δd, and thus the cross section, on knowledge of the plume altitude. Substituting equation equations 4.2 and 4.3 into equation 4.6 allows for cross section to be framed in relation to plume altitude:

$$\mathrm{X} = h \cdot \sum_{i \epsilon plume} (VCD_i \cdot \tan(\alpha_i + \Delta\alpha) - \tan(\alpha_i)) \quad \text{(Eq. 4.8)}$$

Equation 4.8 shows a linear relationship between plume altitude and SO_2 cross section. Because the cross section, and thus emission rate, is dependent on the plume altitude, proper constraints on plume altitude are necessary to ensure accurate emission rates. In the case of Figure 4.1, if we assume that a lofted plume is twice the distance from a scanning DOAS as a plume at summit altitude, then the lofted plume would have twice the SO_2 cross section of plume at summit altitude despite producing the same plume SO_2 scan. One method to constrain plume altitude is through geometric resolution when two or more scanning DOAS stations (Edmonds et al., 2003; Galle et al., 2010), simultaneously measure the same plume. This geometric method to constrain plume altitude is not currently implemented in real-time and cannot be used in situations where only one scanning DOAS station is present or operating.

Here we assess scanning DOAS SO_2 measurements acquired via single-station instruments and develop a new methodology to estimate plume altitude during quiescent (non-eruptive) degassing based on wind-speed data. The initial properties of volcanic plumes are complex but may largely be governed by the plume's capacity to expand and transfer latent heat to the surrounding atmosphere (Morton et al., 1956). In quiescently degassing environments where the mass ejection rate is relatively low, wind becomes increasingly important for promoting plume mixing with cooler ambient air and mechanically forcing the plume down volcanic flanks (Sparks et al., 1997; Bursik, 2001). Because plume altitude for quiescently degassing volcanoes varies largely as a function of wind speed, we investigate using modeled wind speed data to estimate plume altitude, which we then use to calculate SO_2 emission rate from single-station scanning DOAS instruments. We show that our method produces more accurate SO_2 emission rates relative to those calculated assuming a summit plume altitude (as is commonly done in the absence of better plume altitude information) when compared to coincident or semi-coincident airborne measurements from the target volcanoes. We present scanning DOAS measurements collected from three remote and persistently degassing volcanoes during field campaigns in 2019 and 2023. Our target volcanoes are Cleveland Volcano, Gareloi Volcano, and Korovin Volcano (Figure 4.2A), all located in the Aleutian Islands, Alaska. We anticipate that this method can be applied to other locations for improved real-time monitoring with additional validation for different volcanic sites.

4.2 Methods

We employed several different datasets to develop and evaluate our method to estimate plume-altitude using modeled wind speed data. First, we use coincident webcam imagery and modeled wind speed data for Cleveland volcano to calculate a linear relationship between summit modeled wind speed and observed plume altitude. Then we apply our method to NOVAC-campaign-style single-station scanning DOAS data collected at Cleveland, Korovin, and Gareloi Volcanoes in 2019 and one permanent NOVAC scanning DOAS instrument deployed at Cleveland Volcano in September 2022 to estimate plume-altitude and calculate SO_2 emission rates. Finally, we compare our plume altitude estimated SO_2 emission rates against those acquired during coincident to near-coincident airborne DOAS traverses for validation purposes. Below we describe these methods in detail.

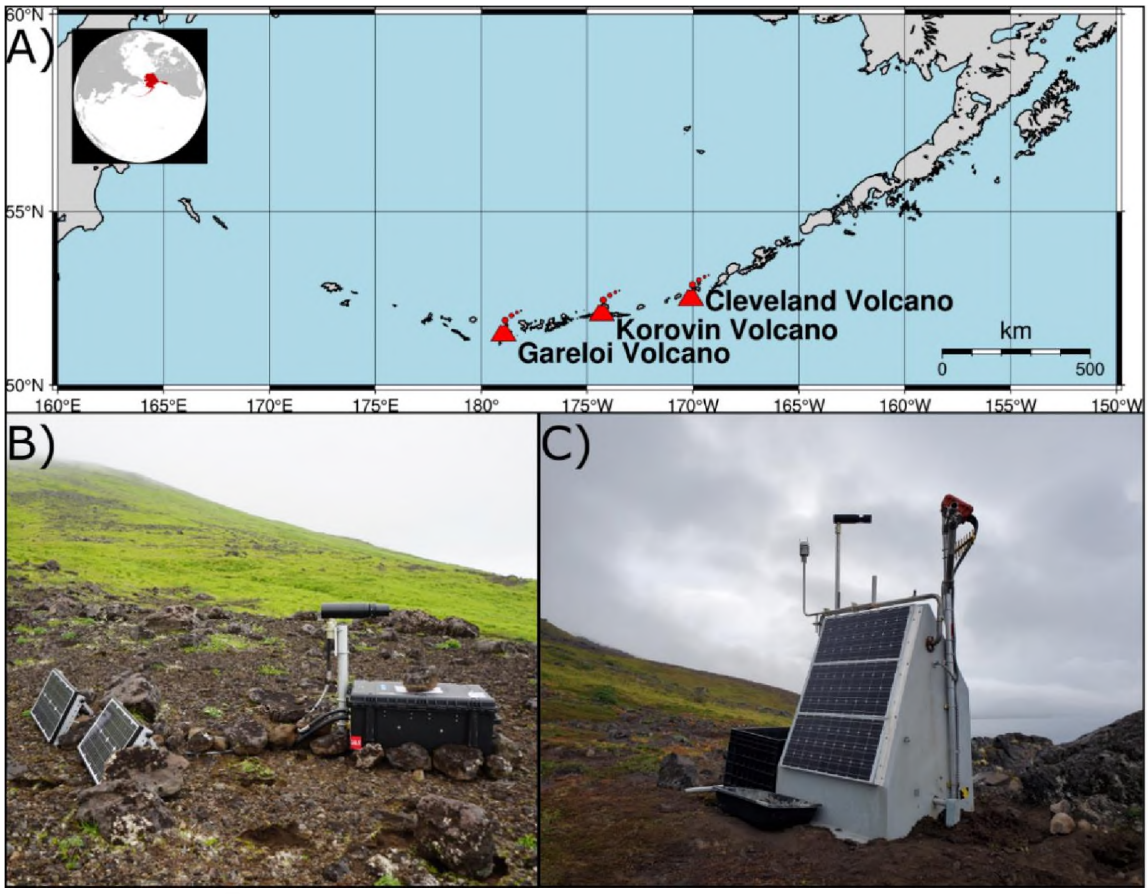

Figure 4.2 A) Map of the Aleutian Islands with Gareloi Volcano, Korovin Volcano, and Cleveland Volcano indicated. B) A deployment of the campaign scanning DOAS at Gareloi Volcano in 2019 showing the scanning head, box with electronic components, and solar panels. C) The permanent scanning DOAS station CLNE installed at Cleveland Volcano in 2022 showing the scanning head, hut containing electrical components, and solar panels.

4.2.1 Plume altitude estimation

Here we aim to estimate plume altitude for single-station scanning DOAS derived SO_2 measurements using modeled wind data. We exploit the inverse relationship between wind speed and plume altitude during periods of passive (non-eruptive) degassing, where higher wind speeds lead to volcanic plumes being blown down volcanic flanks (referred to throughout as "grounded" plumes), while low wind speeds often result in lofted volcanic plumes which ascend vertically before being blown over at higher altitudes. We combined visual observations of plume altitude from AVO-operated webcam imagery (Station CLCO at 52.7866°N, -169.7229°W, 260 m.a.s.l.) of Cleveland Volcano to near-coincident modeled wind data for Cleveland's summit altitude to calculate a linear relationship between these parameters. We identified 23 clear images of Cleveland Volcano between 2014 and 2022 with clear summit conditions and a discernable plume nearly perpendicular to camera direction (Figure 4.1). For the selection process, we consider only images where the plume was visibly near perpendicular (±45°) to the camera angle. We do not anticipate that concentrating on a narrow range of plume directions (typically from the southwest to be measured by our instrument located on Cleveland's northeast flank) will affect our measurements because Cleveland Volcano is relatively conical and surrounded by ocean. The plume altitude was selected at the plume center, defined here as the midpoint of the plume. Plume altitude was determined from the point in the image where the plume maintains a stable altitude following emission. Further, we excluded cases where the plume cannot be confidently distinguished from clouds. After identifying usable images, we calculated plume altitude based on the number of pixels between the plume center and sea level (Figure 4.3A, B). The approximate dimensions of each pixel were calculated by dividing the known summit elevation of Cleveland Volcano by the number of pixels between the volcano's base and summit. The webcam is located ~15.5 km away from Cleveland and positioned approximately horizontally so distortions in pixel size within the image by altitude are minimal.

Wind speeds for Cleveland's summit altitude (1730 m.a.s.l.) at the time of each image acquisition were determined using two datasets: (1) the NOAA-based GFS (1 degree, 3 hourly resolution, forecast product), which are the wind data automatically ingested into the NOVAC program for real-time analysis, and (2) the European Centre for Medium-range Weather Forecasts (ECMWF; 30 km, hourly resolution) ERA5 reanalysis products, which are generally thought to be the most accurate modeled wind data in terms of wind speed but are not available in near-real-time.

Wind speeds for each webcam volcanic plume observation were calculated for Cleveland Volcano's summit altitude, for GFS and ERA5 altitudes separately, by linearly interpolating in time and altitude space between the two closest datapoints from the respective model. Each plume altitude observation was assigned to its corresponding modeled summit wind speed. Then webcam-derived plume altitudes were plotted against the near-coincident modeled wind speed for summit altitude in a scatterplot.

A linear regression was calculated to derive an equation relating plume altitude with modeled wind speed (Figure 4.3C).

We find a good linear correlation between both GFS and ERA5 modeled wind speeds during our 23 webcam observations ($p = 0.66$), indicating that using either model will produce statistically similar plume altitude estimates (Figure 4.3). Emission rates calculated from the estimated plume altitude, an assumed summit plume altitude, and from airborne traverses (when available) were then plotted against each other and compared visually and statistically to assess the utility of our new method. We note that, while estimated scanning DOAS emission rates were calculated for all scanning DOAS scans, for simplicity we present and discuss data derived solely from ERA5 reanalysis products.

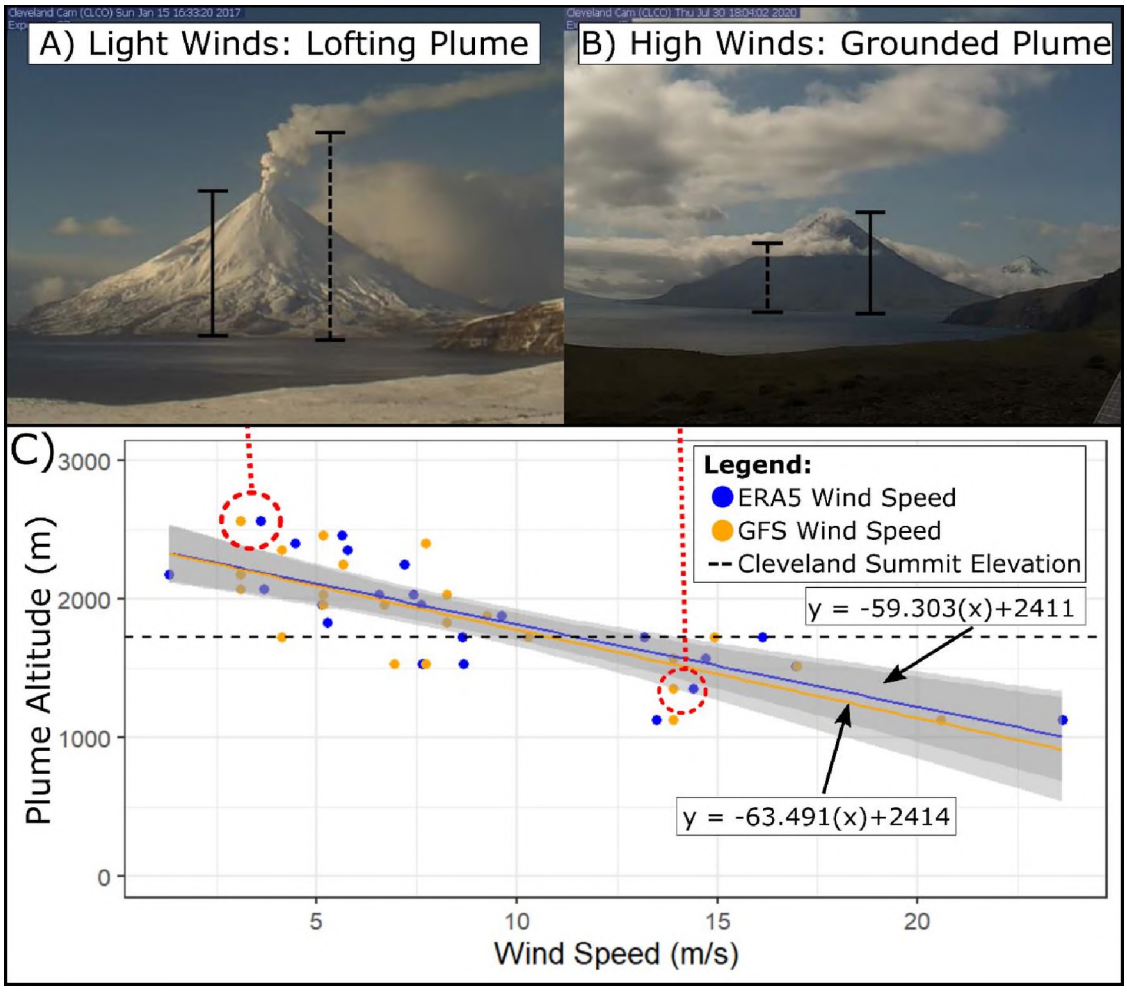

Figure 4.3 Examples of webcam imagery demonstrating a lofted plume at low wind speed (A) and a grounded plume at high wind speed (B). The distance between sea level and approximate plume altitude (meters above sea level) is indicated by the solid yellow and blue lines and the distance between sea level and summit altitude is indicated by the solid black line. C) Linear regression and 95% confidence intervals for ERA5 (blue) and GFS (yellow) estimated plume altitudes are plotted against wind speeds as gray shaded regions.

Due to a lack of sufficient webcam imagery containing a visible plume for the other target volcanoes required to replicate this analysis, we applied the same linear relationship determined for Cleveland to Gareloi and Korovin Volcanoes. We justify this extrapolation based on the relatively similar conditions of the volcanoes, which are all islands in the same geographical environment with well-defined conical edifices and summit altitudes between 1533 – 1730 m.a.s.l.. For use in data processing, where a key input parameter is the altitude of the plume above the scanning DOAS instrument, we modified the y-intercept of each equation for each volcano to reflect the known distance between the instrument and summit elevation, which we refer to in the following as the relative plume altitude. For example, the Korovin Volcano edifice is 197 m lower than Cleveland and the campaign scanning DOAS was deployed at 222 m.a.s.l. (relative to the Cleveland station installed at 326 m.a.s.l.), thus 419 m was subtracted from the y-intercept for both ERA5 and GFS equations. The automatically generated wind speed file for each dataset was then modified to assign a wind speed-derived, estimated (relative) plume altitude. With the estimated plume altitude, SO_2 cross sectional burdens could be calculated and then used with the same modeled wind speeds to calculate emission rates.

4.2.2 Campaign scanning DOAS instrument and measurements

A campaign-style NOVAC scanning DOAS station was deployed at Cleveland Volcano from 21:14, 8 August – 01:47, 10 August, 2019 Coordinated Universal Time (UTC) (instrument at 52.8222°N, -169.945°W, 43 m.a.s.l., AZ 161°), at Korovin Volcano from 18:40 on 27 July to 04:34 on 30 July 2019 UTC (instrument at 52.37934°N, -174.1548°W, 222 m.a.s.l., AZ 239°), and at Gareloi Volcano from 21:14 on 18 July to 05:50 on 22 July 2019 UTC (instrument at 51.8178°N, -178.7787°W, 277 m.a.s.l., AZ 202°; Figure 4.2). Each station consisted of an open conical scanning head (Galle et al, 2010) connected to an Ocean Optics S2000 spectrometer which was housed within a weather-resistant Pelican case (Figure 4.2B). Power to the scanning DOAS was supplied by internal batteries connected to solar panels and controlled by a timer so that continuous scans occurred only during daylight hours. A full scan was performed every 3 – 10 minutes, depending on sunlight intensity, during a 9-hour window from 21:00 – 6:00 UTC. All scanning DOAS data analysis was performed using standard procedures for NOVAC stations (Galle et al., 2010; Arellano et al., 2021). Each scan was processed through the NOVAC software program (version 3.3) to obtain an SO_2 cross section (in SO_2 molecules m^{-1}). Each DOAS scan examined a wavelength range between 310 – 325 nm and was fit following the methods outlined in the post-processing version of the NOVAC program (Johansson et al., 2021) for the trace-gas absorption cross-sections of SO_2 and O_3 (Bogumil et al., 2003; Vandaele et al., 2009), in addition to a Ring effect correction (Grainger & Ring, 1962). SO_2 emission rates were initially calculated for each scan within the NOVAC program assuming a fixed plume altitude at summit altitude. A "plume completeness" algorithm defined in Johansson et al. (2009b) was set to 60% in this study, which is lower than other literature

examples examining scanning DOAS deployments (Arellano et al, 2021; Kunrat et al., 2022) which typically use an 80% threshold. We used this lower threshold to retain a larger amount of data than would be possible with the 80% cutoff, which retains only a small fraction of data for these campaigns. The permanent scanning DOAS dataset at Cleveland volcano at the time of this writing consisted of 11,700 complete scans, 3216 of which are above a plume threshold completeness of 60% and 842 of which are above a plume completeness threshold of 80%.

4.2.3 Permanent scanning DOAS instruments and measurements

The September 2022 – June 2023 data were collected through the installation of two permanent scanning DOAS stations at Cleveland Volcano designed to operate continuously throughout the year and telemeter data directly back to the Alaska Volcano Observatory (AVO; www.avo.alaska.edu) in collaboration with the Anticipating Volcanic Eruptions in Real-Time (AVERT; www.avert.ldeo.columbia.edu) project. Initially, a single instrument on the Northeast side of Cleveland Volcano (Station CLNE at 52.8408°N, -169.9215°W, 326 m.a.s.l.; scanning head oriented at AZ 213°) was installed on 14 September 2022. The CLNE station consists of an Ocean Optics Maya2000 Pro spectrometer placed within an enclosed hut (Figure 4.2C). Fiber optic cables connect the spectrometer to the enclosed conical scanning head via an attached mast. To conserve power, the station is equipped with a manual switch and continuously collects measurements within predefined time periods. The scanning DOAS station at CLNE is set to collect during an 8-hour window each day from 22:00 – 6:00 UTC (11:00 – 19:00 HST) and is currently in operation, continuously telemetering data as of October 2023. A secondary scanning DOAS instrument was installed on the East-northeast side of Cleveland Volcano (Station CLES at 52.8235°N, -169.8951°W, 255 m.a.s.l.; scanning head oriented at AZ 265°) on 31 May 2023; however, telemetry issues have interrupted the acquisition of data which is stored internally on the instruments. Because of the lack of CLES data, this study focuses only on scans from CLNE that are currently available. Scanning DOAS data analysis for these stations is identical to the campaign stations described above.

4.2.4 Upward-facing helicopter DOAS traverses and measurements

A series of helicopter DOAS traverses were conducted with a zenith-facing microDOAS instrument attached to the helicopter step either coincident to or within 1 day of (referred to here as semi-coincident) the operating period of each scanning DOAS instrument. The microDOAS is similar to that described in Galle et al. (2002) and consists of a telescope, Ocean Optics USB2000+ spectrometer, GPS, and computer within a hardshell container. All helicopter DOAS traverse data were processed using a custom MATLAB program for spatial analysis of mobile DOAS data (mDOAS version 3.17, as used by Kern et al., 2020). The DOAS fit of each individual spectrum was analyzed on DOASIS software (Kraus,

2006) between 310 – 325 nm to account for the absorption cross sections of SO2 (Bogumil et al., 2003), O3 (Vandaele et al., 2009), and a Ring-effect correction (Grainger & Ring, 1962). For the purposes of comparability between scanning DOAS and helicopter DOAS measurements, all helicopter DOAS-derived emission rates were calculated using ERA5 modeled wind speeds. Wind circles were conducted when possible during DOAS traverses and were used to evaluate the accuracy of modeled wind speeds.

4.3 Results

4.3.1 Plume altitude results

Our empirical analysis finds an inverse linear relationship between webcam-derived plume altitudes and wind speed for Cleveland volcano (Figure 4.3). In general form, we find that relationship can be expressed as:

$$H_P = H_S + (v_N - v) \cdot k \quad \text{(Eq. 4.9)}$$

Where H_P is the estimated altitude of the plume relative to the scanning DOAS which we refer to as the relative plume altitude (equivalent to h in figure 4.1), and H_S is the vertical distance between the scanning DOAS instrument and the summit elevation. We define v_N as the windspeed at which a potentially buoyant plume remains at summit elevation (in the case of Cleveland found to be 11.5 m s^{-1}; Figure 4.3) and define v as the modeled wind speed at summit altitude at the time of the scan. A plume altitude sensitivity correction factor, k, is the empirically found factor used to scale the relative plume altitude, which we calculate as -59.3 s (Figure 4.3).

4.3.2 Error estimation

Galle et al. (2010) provide a discussion of error sources for scanning DOAS measurements of volcanic gas emission rates. In the following, we examine how our new method for estimating plume altitude (Eq. 4.4) influences the uncertainty of derived emission rates. As discussed in section 4.1, the volcanic gas emission rate is derived from the product of the cross-sectional gas burden X and the wind speed v. The cross-sectional burden X itself depends linearly on the plume altitude (Eq. 4.8).

In our proposed empirical approach, we assign an inverse linear relationship between wind speed and plume altitude (Eq. 4.9). In simplified form, we assume:

$$h = k \cdot v \quad \text{(Eq. 4.10)}$$

Entering this relationship into Eq. 4.8 yields:

$$\phi = k \cdot v^2 \cdot \sum_{ieplume}(VCD_i \cdot \tan(\alpha_i + \Delta\alpha) - \tan(\alpha_i)) \quad \text{(Eq. 4.11)}$$

For the purposes of examining the errors associated with wind speed and plume altitude arising from our novel approach, we choose to momentarily neglect errors associated with the spectroscopic retrievals of VCD or angular positioning of the DOAS scanner α (see Kern, 2009 for a full discussion of these error sources). In the following, we abbreviate the sum over the column densities in the scan as $\sum VCD$.

The standard error of the emission rate ϕ is then given by the equation:

$$\sigma_\phi{}^2 = \left(\frac{d\phi}{dk}\right)^2 \sigma_k{}^2 + \left(\frac{d\phi}{dv}\right)^2 \sigma_v{}^2 \quad \text{(Eq. 4.12)}$$

Calculating the partial derivatives yields:

$$\frac{d\phi}{dk} = v^2 \cdot \sum VCD \quad \text{(Eq. 4.13)}$$

$$\frac{d\Phi}{dv} = 2kv \cdot \sum VCD \quad \text{(Eq. 4.14)}$$

Entering Equations 4.13 and 4.14 into 4.12 results in:

$$\sigma_\phi{}^2 = (v^2 \sum VCD)^2 \sigma_k{}^2 + (2kv \sum VCD)^2 \sigma_v{}^2$$

$$= \frac{\phi^2}{k^2}\sigma_k^2 + \frac{4\phi^2}{v^2}\sigma_v^2 \quad \text{(Eq. 4.15)}$$

Solving for the relative error in emission rate yields:

$$\frac{\sigma_\phi}{\phi} = \sqrt{(\frac{\sigma_k}{k})^2 + 4(\frac{\sigma_v}{v})^2} \quad \text{(Eq. 4.16)}$$

Where $(\frac{\sigma_v}{v})$ is the relative error in modeled wind speed data (~25%; Galle et al., 2010) and $(\frac{\sigma_k}{k})$ is the relative error in the slope of the linear fit of webcam plume altitudes (~10%, Figure 4.3). Eq. 4.16 shows that, when using our new method, the wind speed error becomes a dominant source of uncertainty as it now not only describes the motion of the plume but also factors into the calculation of the cross-sectional gas burden. Entering the uncertainties mentioned above yields a standard error of 51% for the emission rate.

4.3.3 Overview of measurement period

Permanent scanning DOAS SO_2 emission rates were evaluated between 13 September 2022 – 7 June 2023 except for between 22 September – 19 October 2022 when there was a network power outage which resulted in lost data. The processed data consist of 3264 individual scans which met our plume completeness criteria (>60%), with a plume detected in at least one scan on 164 of 267 total operating

days. Summary statistics for an estimated and assumed summit plume altitude are presented for the entirety of the available Cleveland September 2022 – June 2023 data in Table 4.1 in aggregate and monthly formats. The measurement period of campaign scanning DOAS deployments in 2019 covers 105 scans at Cleveland Volcano between 7 – 10 August, 178 scans at Korovin Volcano between 27 – 30 July, and 85 scans at Gareloi Volcano between 18 – 20 July. Summary statistics for estimated and assumed summit plume altitudes are presented for campaign deployments in Table 4.2 in aggregate and as daily measurements due to the short duration of each deployment. Coincident helicopter DOAS data were collected for the September 2022 – June 2023 Cleveland dataset, in addition to the 2019 Cleveland and Gareloi datasets. Semi-coincident helicopter DOAS traverses were made within 24-hours of a scanning DOAS scan for the Gareloi and Korovin Volcano datasets. These observations can be used to help evaluate our plume altitude method, in addition to our corresponding wind speed and emission rate results. Summary statistics and available plume speed constraints based on wind circle data for all coincident and semi-coincident traverses are presented in Table 4.3.

4.3.4 Plume altitude validation

Wind circles performed during helicopter traverses provide an independent verification of modeled wind speed. Helicopter wind circles performed at Cleveland Volcano on 20 September 2022 UTC were 7.7 (± 0.6) m s^{-1} and agree well with ERA5 models for the time (7.7 m s^{-1}; Table 4.3). Helicopter wind circles performed at Korovin Volcano on 26 July 2019 UTC indicate a wind speed of 7.6 (± 0.6) m s^{-1}, ~2 m s^{-1} less than ERA5 modeled wind speed for that time. Based on these limited comparison results, we estimate uncertainty in ERA5 modeled wind data used here to be $\leq$ 2 m/s, which we use for the remainder of our estimations.

Helicopter traverses also provide an additional validation of estimated plume altitude during flight configurations where a series of in situ sensors (e.g., MultiGAS, Aiuppa et al, 2005) are onboard to measure volcanic plume composition. Direct encounters of the plume by the helicopter at specific altitudes can be compared with estimated plume altitude for a given wind speed at the time of intersection. On 9 August 2019 the Cleveland Volcano plume was intersected during a gas flight between 1400 – 1800 m when we estimate a plume altitude of 1937 m. On 26 July 2019 the Korovin Volcano plume was intersected by the helicopter between 1290 – 1500 m when we estimate a plume altitude of 1426 m. On 19 July 2019 the Gareloi Volcano plume was intersected at 1185 – 1525 m when we estimate a plume altitude of 2114 m. These three validation opportunities find plume altitudes at + 137 m, within range, and + 589 m of our estimates for Cleveland, Korovin and Gareloi respectively. Indicating that our method works to within 7% for Cleveland where the method was developed and to within 38% for the other volcanoes. We note that the measured plume altitudes may not reflect the true upper or lower extent of the plume as they may have been acquired directly above the vent, rather than downwind where the

plumes are assumed to have reached a stable altitude. Measured plume altitude also represents where plume intersections have occurred rather than an absolute constraint of the plume, and helicopter flights may have not occurred above or below any of the intersected altitudes. Future work will aim to further validate our method as described in section 4.6.1.

4.4 SO_2 Emission rate results

4.4.1 Cleveland Volcano (2019)

During the 2019 Cleveland Volcano campaign scanning DOAS deployment wind speeds ranged from 3.0 – 8.2 m s^{-1} (median 4.4 m s^{-1}; Table 4.2), which was relatively stable compared to the other campaign deployments and resulted in an estimated plume altitude that was ~200 – 500 m higher than what would be assumed for an assumed summit plume altitude. For the entire campaign, the median SO_2 emission rate calculated using our estimated plume altitude was 321 ± 131 t SO_2 day^{-1} (range: 121 – 631 t SO_2 day^{-1}; Table 4.2). The median estimated plume altitude was 61 t SO_2 day^{-1} higher, and the standard deviation was 27 t SO_2 day^{-1} larger than those calculated with an assumed summit altitude plume. These emission rates are within range of a coincident helicopter traverse on August 10 of 149 ± 50 t SO_2 day^{-1}. This emission rate range is also lower but within range of the permanent scanning DOAS data from 2022 (299 ± 133 t SO_2 day^{-1}; Table 4.3). A noticeable decrease and subsequent increase in SO_2 emission rate on August 8 was correlated to a drop and rise in wind speed and can be seen for both the estimated (Figure 4.4A) and assumed summit (Figure 4.4B) plume altitude derived results.

4.4.2 Korovin Volcano (2019)

A wide range in wind speeds at Korovin Volcano of 3.8 – 12.7 m s^{-1} (median 5.1 m s^{-1}; Table 4.2) resulted in estimated plume altitudes between 200 m lower and 50 m higher than for an assumed summit plume altitude. Korovin Volcano emission rates calculated using our estimated plume altitudes were nearly identical to those calculated assuming a summit plume altitude. The aggregate emission rate for the entire measurement period using an estimated plume altitude was 435 ± 219 t SO_2 day^{-1} (range: 144 – 1451 t SO_2 day^{-1}; Table 4.2) compared to emission rates assuming a fixed summit plume altitude of 394 ± 214 t SO_2 day^{-1} (range: 114 – 1315 t SO_2 day^{-1}). For this period the median SO_2 emission rate calculated using an estimated plume altitude was 77 t SO_2 day^{-1} higher and the standard deviation was 3 t SO_2 day^{-1} larger than those with an assumed fixed summit altitude plume. One set of coincident helicopter DOAS transects were performed one day after (30 July 2019 UTC) the scanning DOAS deployment period had a median emission rate of 361 ± 107 t SO_2 day^{-1} (range: 282 – 611 t SO_2 day^{-1}; Table 4.3), which is within range of scanning DOAS SO_2 emission rate measurements calculated with either an estimated (Figure 4.5A) or fixed (Figure 4.5B) plume altitude. Average calculated scanning DOAS emission rates over the entire deployment period are heavily weighted by an apparent pattern of increasing SO_2 emission rate

over 2 hours on July 30 (Figure 4.5A), culminating in a maximum of 1451 t SO_2 day^{-1} at 22:40 UTC. This emission rate pattern does not appear to be related to a corresponding increase or decrease in wind speed and occurs when reanalysis products calculate a wind speed of ~10 m s^{-1}. As a result of similar predicted plume altitudes, this feature is prominent in both estimated and summit altitude plume emission rate calculations.

4.4.3 Gareloi Volcano (2019)

Wind speeds at Gareloi Volcano for the entirety of the scanning DOAS campaign measurement period ranged from 0.2 – 5.4 m s^{-1} (median 1.8 m s^{-1}; Table 4.2), thus all scans were estimated to a plume altitude 300 – 700 m higher than an assumed summit plume altitude. Wind speed through the scanning DOAS collection period was constrained by ERA5 reanalysis products to be initially very low at < 1 m s^{-1} and steadily increased through the deployment period to 6 m s^{-1}. Calculated SO_2 emission rates via scanning DOAS were positively correlated with increased wind speed (as expected). Over the entirety of the scanning DOAS measurement periods, the median SO_2 emission rate at Gareloi Volcano was 164 ± 115 t SO_2 day^{-1} (range: 13 – 635 t SO_2 day^{-1}; Table 4.2). For this period the median emission rate calculated using the estimated plume altitude method was 29 t SO_2 day^{-1} higher and the standard deviation was 52 t SO_2 day^{-1} larger than those calculated assuming a summit altitude plume. Both estimated and assumed summit plume altitude emission rates were within range of coincident helicopter DOAS traverses on 19 – 20 July at 121 ± 16 t SO_2 day^{-1} (range: 91 – 135 t SO_2 day^{-1}; Table 4.3). Earlier semi-coincident DOAS traverses on 16 and 17 July were conducted under higher wind speeds and yielded larger emission rates. Because of the consistently low wind speed during this measurement period, our plume altitude regression predicted that the plume was lofted above summit elevation for the entirety of the scanning DOAS deployment, and thus employing an estimated plume altitude (Figure 4.6A) over this time at Gareloi Volcano produced higher SO_2 emission rates than assuming a summit plume altitude (Figure 4.6B) of 113 ± 86 t SO_2 day^{-1} (range: 8 – 476 t SO_2 day^{-1}).

Table 4.1 Summary statistics for the permanent single-station scanning DOAS deployment at Cleveland Volcano, 13 September 2022 – 7 June 2023, subdivided by month assuming an estimated and fixed plume altitude.

			Emission rate (t SO_2 day^{-1}) for estimated plume altitude			**Emission rate (t SO_2 day^{-1}) for a fixed summit plume altitude**			**Wind speed (m s^{-1}) during measurement period**		
	Days with plume detections	**n**	**median**	**SD[A]**	**IQR[B]**	**median**	**SD[A]**	**IQR[B]**	**median**	**SD[A]**	**range[C]**
Cleveland total	164	3216	278	250	167 – 450	330	319	175 – 558	9.9	6.2	0.8 – 44.6
September	6	196	289	133	213 – 364	520	318	253 – 753	19.9	8.2	3.6 – 29.0
October	12	392	399	204	290 – 558	565	346	337 – 827	16.1	6.3	3.5 – 44.6
November	28	482	340	289	211 – 525	375	304	205 – 602	8.7	4.5	5.0 – 26.3
December	17	193	294	280	201 – 473	330	399	189 – 631	12.0	5.2	4.2 – 27.5
January	20	345	477	312	256 – 645	438	341	245 – 648	8.1	3.6	0.8 – 18.4
February	20	253	255	155	188 – 339	388	222	277 – 516	16.0	7.3	5.1 – 32.9
March	20	428	163	120	111 – 233	179	204	107 – 299	9.4	5.8	3.0 – 30.9
April	21	529	245	222	143 – 389	268	268	134 – 445	9.4	4.8	2.5 – 24.6
May	14	191	116	205	58 – 200	97	272	44 – 179	5.0	5.1	1.0 – 18.7
June	6	211	349	262	221 – 479	353	247	214 – 489	9.0	1.9	4.6 – 13.2

A: SD here is the 1σ standard deviation

B: IQR represents the inter quartile range, or the range from the 25th percentile to the 75th percentile of the observations

C: Range indicates the full range of measured values

Table 4.2 Summary statistics for each single-station scanning DOAS deployment period in this study. Each deployment is broken up into 8-hour periods (UTC time) when the instrument was operating.

		Emission rate (t SO_2 day^{-1}) for estimated plume altitude			Emission rate (t SO_2 day^{-1}) for a fixed summit plume altitude			Wind speed (m s^{-1}) during measurement period		
Volcano (year)	**n**	**median**	**SD[A]**	**IQR[B]**	**median**	**SD[A]**	**IQR[B]**	**median**	**SD[A]**	**range[C]**
Cleveland total (2019)	105	308	131	213 – 404	247	104	169 – 347	4.4	1.5	3.0 – 8.2
Aug 7 – 8	37	455	82	401 – 506	389	69	335 – 429	6.4	0.7	5.8 – 6.8
Aug 8 – 9	58	220	60	185 – 280	173	48	144 – 222	4.1	0.4	3.5 – 4.2
Aug 9 – 10	10	352	61	334 – 369	314	54	292 – 329	8.1	0.3	8.0 – 8.2
Korovin total (2019)	178	365	219	310 – 449	288	214	237 – 374	5.1	2.5	3.8 – 12.7
Jul 27 – 28	68	352	53	310 – 388	269	44	237 – 304	4.4	0.6	4.0 – 4.9
Jul 28 – 29	65	326	84	275 – 387	254	68	216 – 300	5.1	0.4	4.9 – 6.1
Jul 29 – 30	45	716	267	512 – 843	663	227	519 – 774	9.7	1.2	8.8 – 12.7
Gareloi total (2019)	85	159	115	100 – 207	107	86	65 – 140	1.8	1.3	0.2 – 5.4
Jul 18 – 19	17	27	9	19 – 36	17	6	12 – 22	0.3	0.1	0.2 – 0.4
Jul 19 – 20	63	179	60	124 – 208	121	42	82 – 141	1.9	0.7	1.6 – 2.7
Jul 20	5	436	119	399 – 591	327	89	299 – 443	5.4	0.0	5.4 – 5.5

A: Standard deviation here 1σ of the mean value

B: The inter quartile range, or the range in which 25% of measurements fall above and below the median value

C: Full range of measured values

Table 4.3 Summary statistics for each helicopter DOAS traverse period in this study

	Helicopter DOAS traverse emission rate (t SO_2 day^{-1})				Wind speed from model (m s^{-1})			Wind speed from wind circles (m s^{-1}) (± SD)	Plume altitude (m)
Volcano (day, year)	**n**	**median**	**SD[A]**	**range[B]**	**median**	**SD[A]**	**range[B]**		
Cleveland (20 Sept 2022)	8	400	80	263 – 511	7.7	NA	NA	7.7 (± 0.6)	> 1300
Cleveland (9 Aug 2019)	1	147	NA	NA	8.4	NA	NA		1400 – 1800
Korovin (2019)	8	361	107	282 – 611	12.3	2.3	9.3 – 14.7		
Jul 25	0	NA	NA	NA	9.7	0.1	9.7 – 9.9	7.6 (± 0.6)	1290 – 1500
Jul 30	8	361	107	282 – 611	12.4	2.3	9.3 – 14.7		
Gareloi (2019)	6	130	57	91 – 268	1.8	1.2	1.5 – 5.8		
Jul 16	1	268	NA	NA	5.8	NA	NA		
Jul 17	1	157	NA	NA	4.2	NA	NA		
Jul 19 – 20	4	121	16	91 – 135	1.7	0.4	1.5 – 2.9		1185 – 1525

A: Standard deviation here 1σ of the mean value
B: Full range of measured values

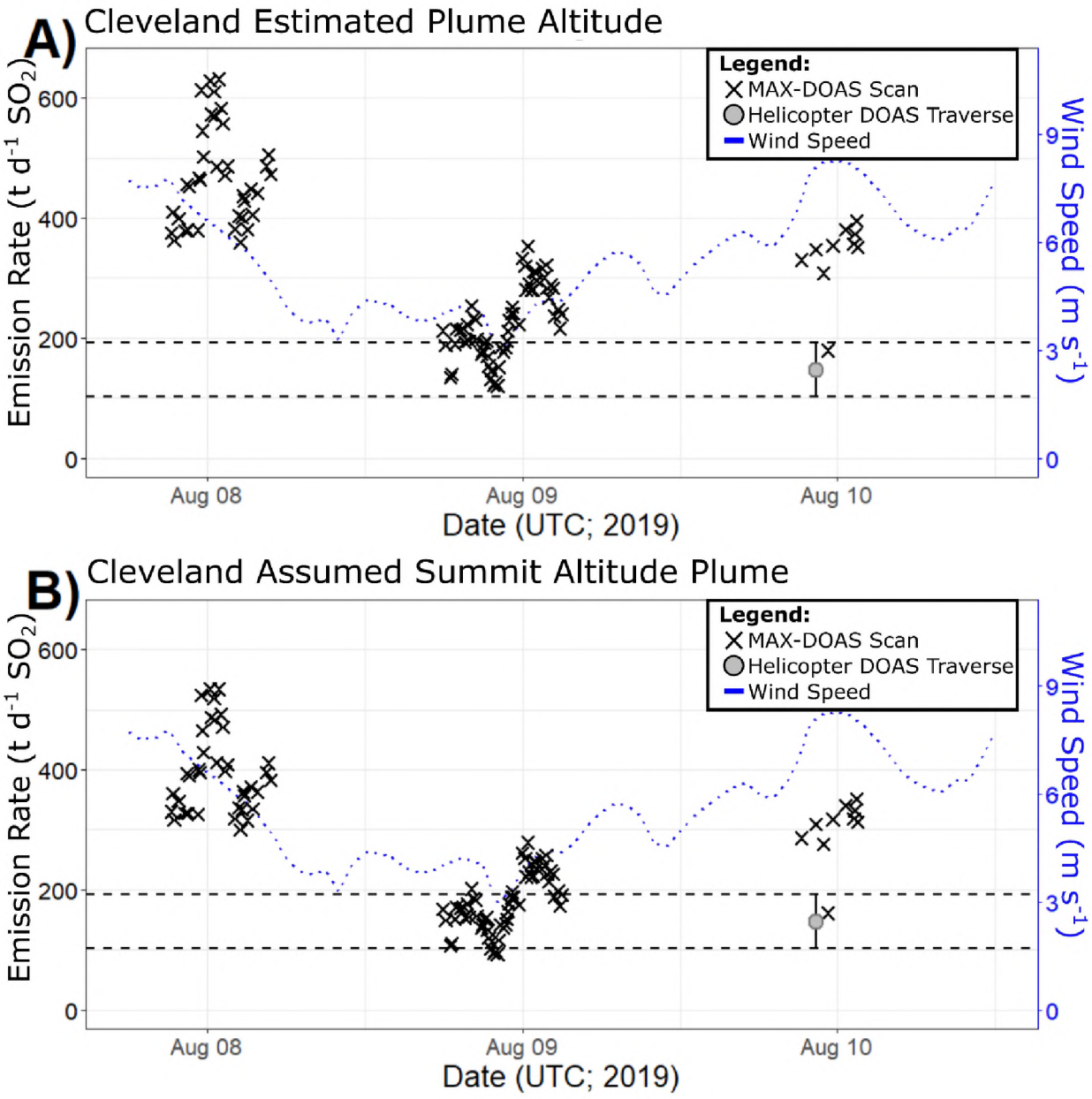

Figure 4.4 A) SO_2 emission rates from Cleveland Volcano between August 7 – 10, 2019 assuming an estimated plume altitude. Each scanning DOAS measurement with a plume completeness > 0.6 is shown as a black X and helicopter DOAS traverses are shown as grey-filled circles with the maximum and minimum uncertainties projected horizontally as dashed black lines. ERA-5 wind speeds through the measurement period are plotted as a dotted blue line measured on the right axis and wind speeds from wind circles are plotted as blue dots. B) Same as A but assuming a fixed plume altitude at summit elevation.

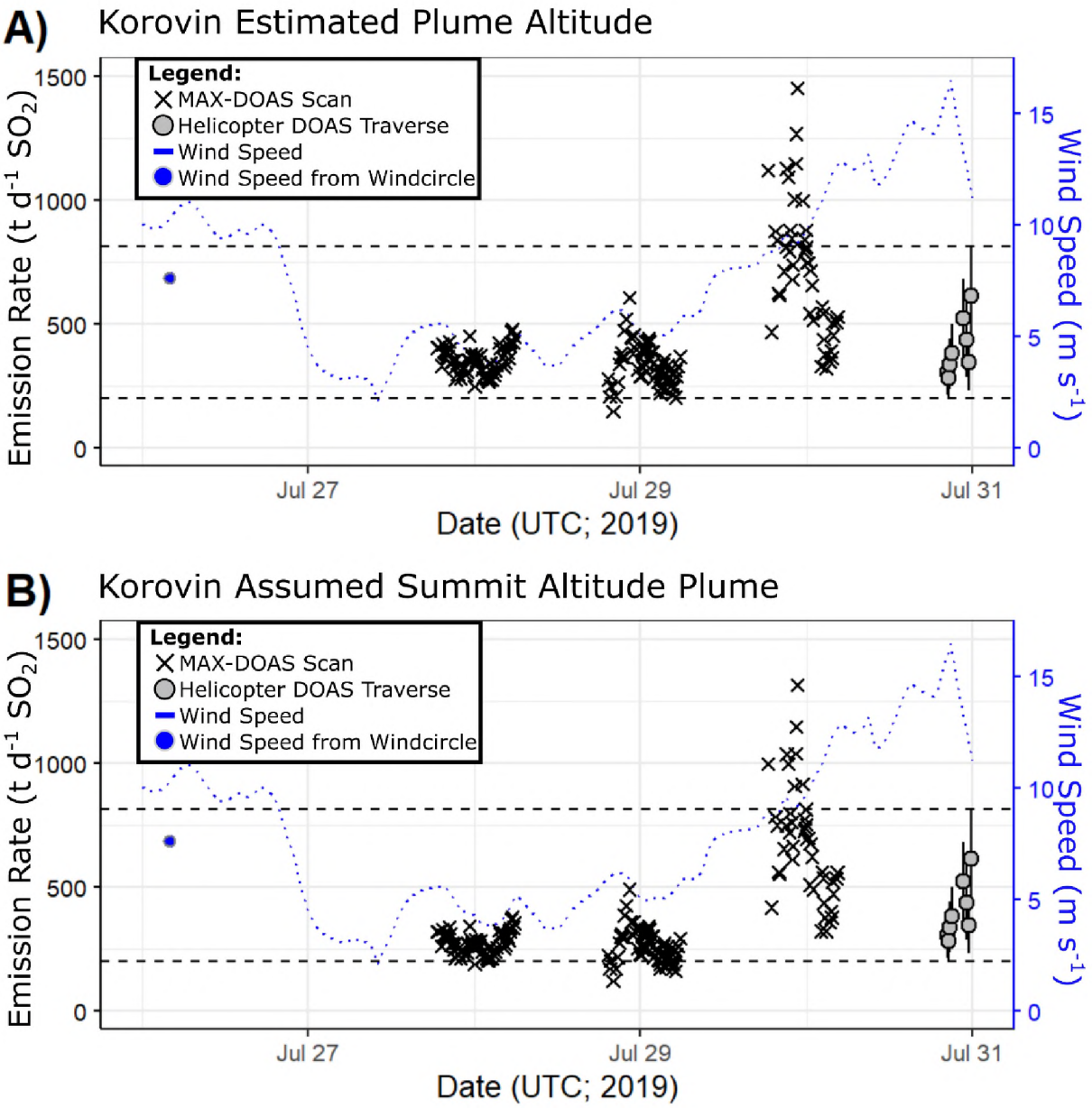

Figure 4.5 A) Emission rate from Korovin Volcano between 26 – 30 July 2019 assuming an estimated plume altitude. Each scanning DOAS measurement with a plume completeness > 0.6 is shown as a black X and helicopter DOAS traverses are shown as grey-filled circles with the maximum and minimum traverse error projected horizontally as dashed black lines. ERA-5 wind speeds through the measurement period are plotted as a dotted blue line measured on the right axis and wind speeds from wind circles are plotted as a blue dot. B) Emission rate from Korovin Volcano in 2019 assuming a fixed plume altitude at summit elevation. All symbols used in part B are the same as part A.

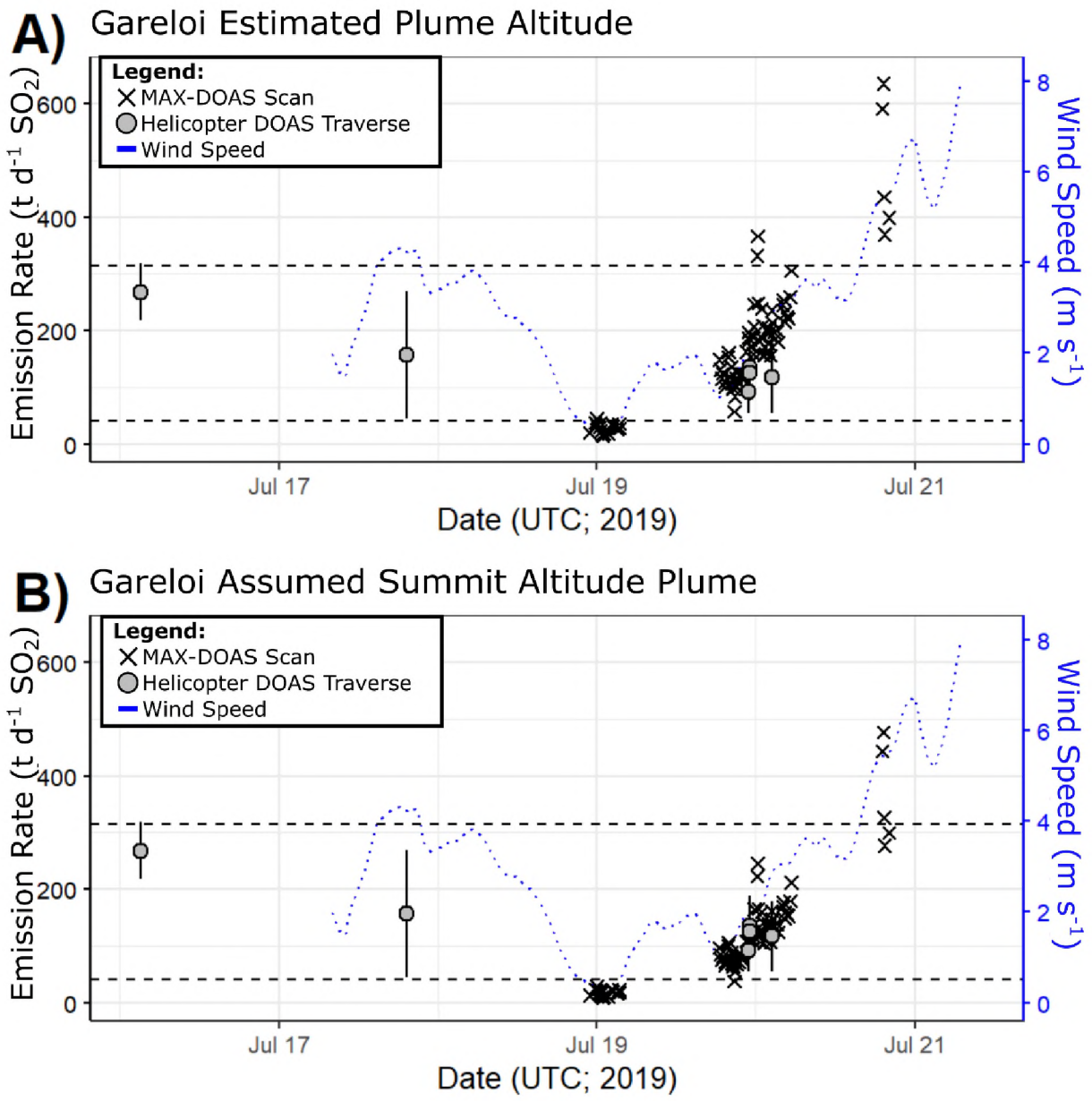

Figure 4.6 A) Emission rate from Gareloi Volcano between 18 – 20 July 2019 assuming an estimated plume altitude. Each scanning DOAS measurement with a plume completeness > 0.6 is shown as a black X and helicopter DOAS traverses are shown as grey-filled circles with the maximum and minimum traverse uncertainty projected horizontally as dashed black lines. ERA-5 wind speeds through the measurement period are plotted as a dotted blue line measured on the right axis. B) Same as A but assuming a fixed plume altitude at summit elevation.

4.5 SO_2 Emission rate results from permanent scanning DOAS deployments

4.5.1 Cleveland Volcano (September 2022 – June 2023)

The permanent September 2022 – June 2023 Cleveland Volcano scanning DOAS deployment dataset includes months of operation. Individual scans span a large range of wind speeds between 0.8 – 44 m s^{-1} (median 9.9 m s^{-1}; Table 4.1). As a result of this larger dataset, the interpreted plume altitude using the NOVAC program for this period of time was between 1700 m lower (just above the instrument) to 700 m higher than for an assumed summit plume altitude. We find that using an estimated plume altitude yielded a lower median emission rate and standard deviation than assuming a summit plume altitude. The median estimated SO_2 emission rate over the entire measurement period was 278 ± 250 t SO_2 day^{-1} (range: 9 – 1817 t SO_2 day^{-1}; Table 4.1) which is within range of helicopter transects collected on 20 September, 2022 of 400 ± 80 t SO_2 day^{-1} (range: 263 – 511 t SO_2 day^{-1}; Table 4.2). Subdivided into monthly periods of measurements, the median monthly emission rates agree within ± 200 t SO_2 day^{-1} of each other (Table 4.1). Over the entire measurement period, we find a 52 t SO_2 day^{-1} lower median emission rate using an estimated plume altitude than with an assumed summit plume altitude. While this is a relatively small difference in aggregate, individual scans or smaller timespans which contain high wind speeds typically produce large emission rates when assuming a summit altitude plume. During these periods of high wind speed, emission rates are notably reduced by our method of estimating plume altitude (Figure 4.8).

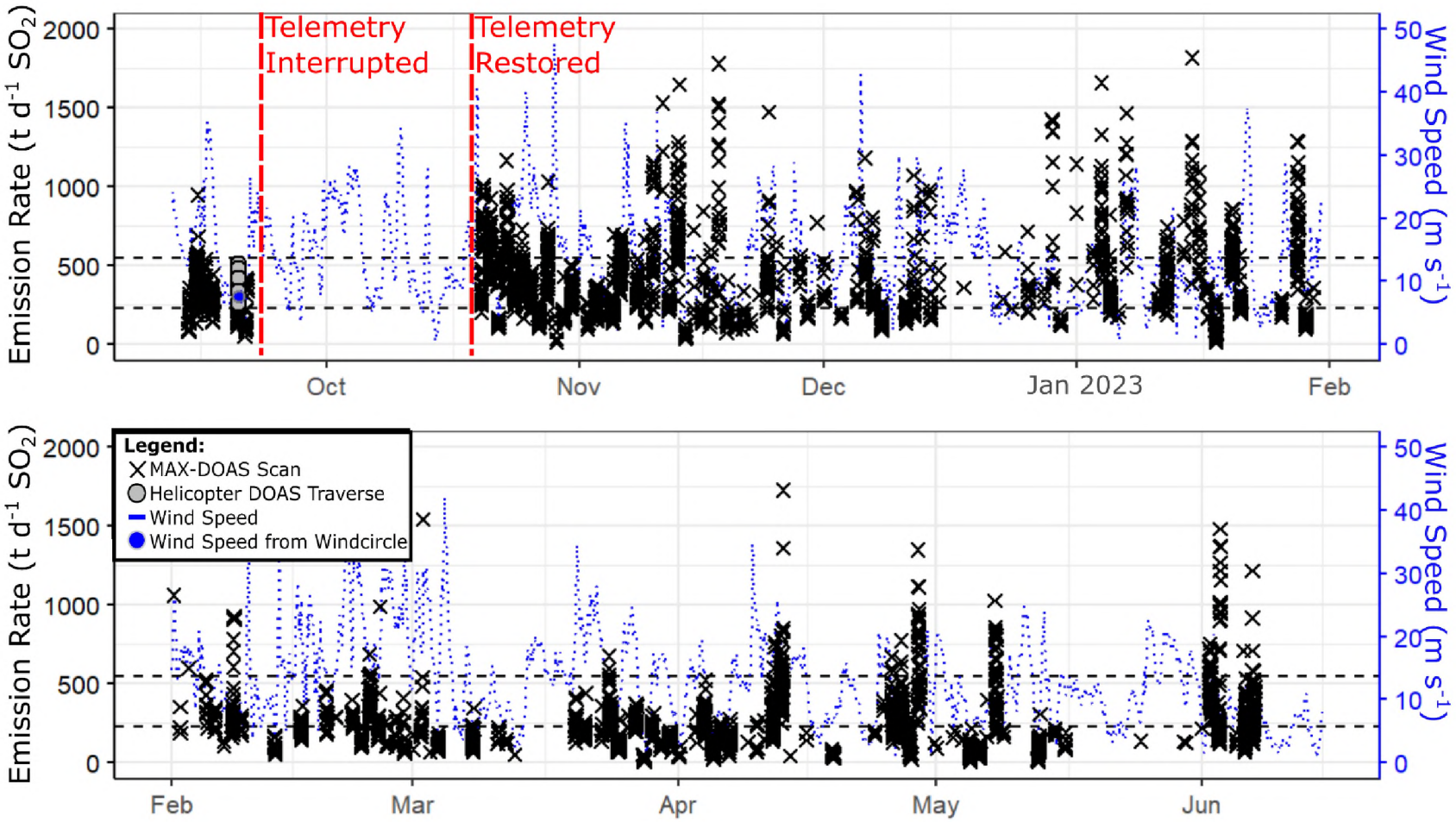

Figure 4.7 A time series of emission rate from the permanent scanning DOAS deployment at Cleveland Volcano between September 2022 – June 2023 assuming an estimated plume altitude. Each scanning DOAS measurement with a plume completeness > 0.6 is shown as a black X and helicopter DOAS traverses performed in September 2022 are shown as grey-filled circles with the maximum and minimum traverse error projected horizontally as dashed black lines. ERA-5 wind speeds through the measurement period are plotted as a dotted blue line measured on the right axis and wind speeds from wind circles are plotted as a blue dot. The period during which telemetry was interrupted is indicated by vertical red dashed lines. Other periods with missing data are due to wind directions that did not bring the plume over the scanner.

4.6 Discussion

4.6.1 Improvements from estimated plume altitudes

We find from our measurements that using an estimated plume altitude based on modeled wind data and our derived linear equation provides a smaller range in calculated emission rates, and lower standard deviations in cases of large wind speed variation. The available data from the permanent scanning DOAS station at Cleveland Volcano from September 2022 – June 2023 contain several examples of periods where emission rate over short periods of time is more consistent with the mean value for the full deployment period when calculated using an estimated plume altitude. A lofted plume above summit elevation yields SO_2 scans representing a larger area and producing larger calculated emission rates than the same scan for a plume observed at summit elevation (Fig. 4.9). The converse is true for a grounded plume, where the same SO_2 scan would yield a lower SO_2 cross sectional burden and emission rate than a summit altitude plume. A good illustration of the reduced variation in SO_2 emission rate is during the period of 16 – 17 September 2022 at CLNE after the scanning DOAS was installed and before telemetry to the instrument was lost (Figure 4.8). During this time, the median modeled wind speed was consistently higher than any other individual month at 19.9 m s^{-1} (Table 4.1), which corresponds to a plume altitude of 820 m. During this period, we observe the largest difference between calculated emission rate using an estimated plume altitude (Figure 4.8A) and those derived from an assumed summit altitude (Figure 4.8B). Specifically, from 16 – 17 September the median emission rate decreases by up to 595 t SO_2 day^{-1} and the standard deviation for each scanning period decreases by up to an order of magnitude between the estimated and assumed summit plume altitude calculations.

One limitation of our method, which affects the permanent scanning DOAS dataset presented here, stems from estimating emission rates at wind speeds much higher than those used to generate our linear correlation (~25 m s^{-1}; Figure 4.3). Because we derive only an empirical relationship, the uncertainty in plume altitudes at wind speeds > 25 m s^{-1} is not constrained and is likely larger than estimated. A further problem arises when the wind data from the permanent Cleveland dataset reaches values in excess of 35.1 m s^{-1}. Equation 4.9 indicates that these high wind speeds would result in an estimated plume altitude below the scanning DOAS stationed at CLNE. While it may be physically possible for the plume to be below the instrument but still above the ground-surface in cases where the plume is spatially offset, we think any results that give a negative relative plume altitude or are calculated for wind speeds > 25 m s^{-1} should be considered less reliable. In the September 2022 – June 2023 dataset, only 116 scans meet those criteria, representing under 0.03% of all measurements. We therefore recommend that applications of our method remove all negative plume altitudes from analysis or note those results based on windspeeds > 25 m s^{-1} as questionable. Wind speeds did not exceed 12.7 m s^{-1} for

any period of the campaign scanning DOAS deployments (Table 4.2) and therefore did not produce negative relative plume altitudes.

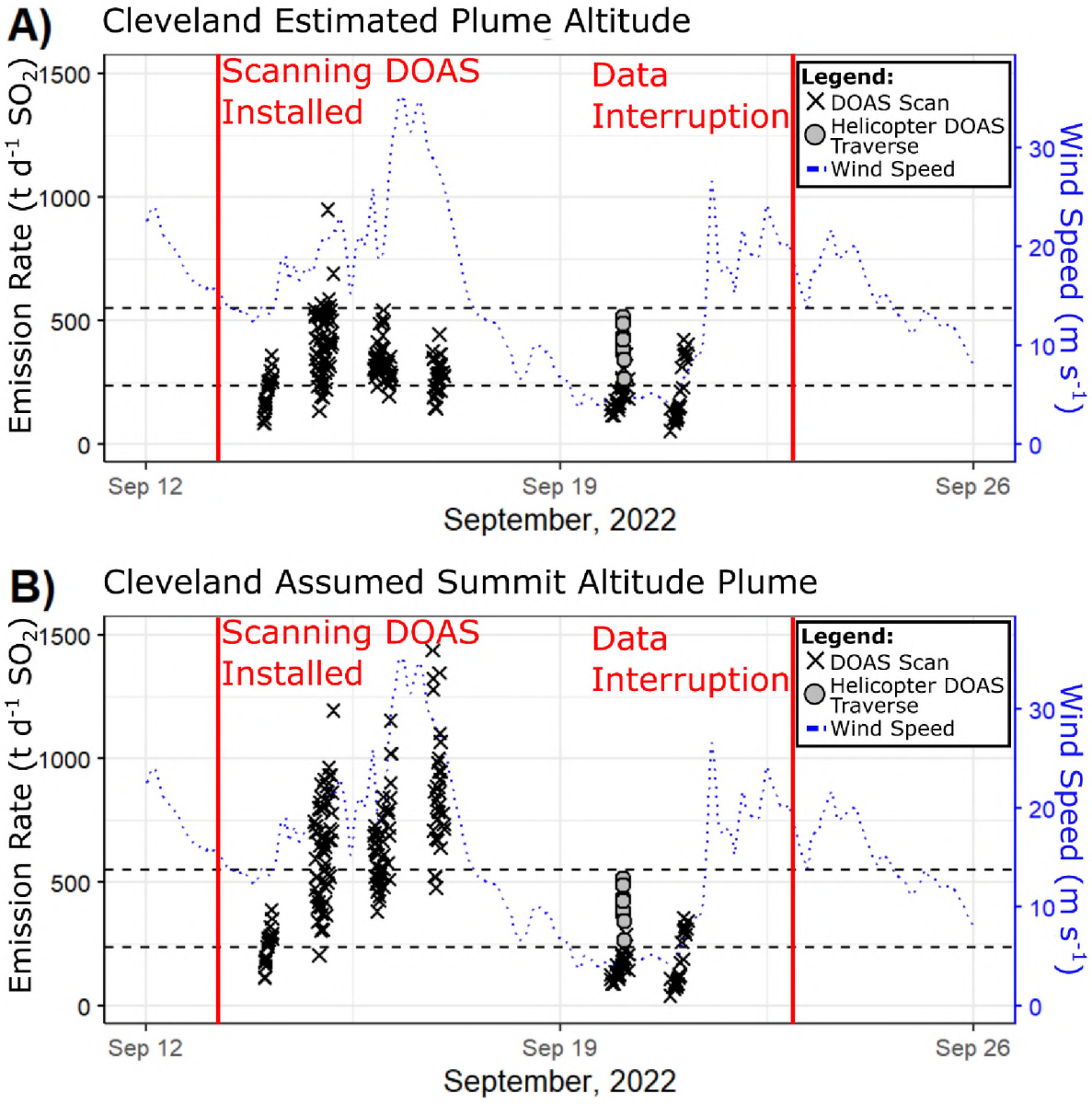

Figure 4.8 A) SO_2 emission rate from Cleveland Volcano between 14 – 21 September 2022 assuming an estimated plume altitude. Each scanning DOAS measurement with a plume completeness > 0.6 is shown as a black X and helicopter DOAS traverses are shown as grey-filled circles with the maximum and minimum traverse error projected horizontally as dashed black lines. ERA-5 wind speeds through the measurement period are plotted as a dotted blue line measured on the right axis. The initiation and interruption of dataflow is denoted by a vertical red line. B) Same as seen in A, but assuming a fixed plume altitude at summit elevation.

In contrast to our long-term dataset findings, we document a marginally (< 52 t SO_2 day^{-1}) larger standard deviation in SO_2 emission rates calculated using our estimate plume altitude during all our short-dataset periods using campaign scanning DOAS in 2019. This increased variation is likely because all short-term datasets were collected during periods of relatively low wind speed with a small amount of variability (Table 4.2). While our estimated plume altitude method predicts that all lofted plumes will result in increased SO_2 emission rates, our findings suggest that emission rates calculated using this method are less impacted by very low wind conditions (< ~3 m s^{-1}) relative to light to moderate wind speeds (~3 – 11.5 m s^{-1}), with the largest impact appearing to be on measurements ~9 m s^{-1}.

Galle et al. (2010) discusses four main causes of uncertainty in scanning DOAS emission rate measurements broadly: errors in spectroscopy, atmospheric scattering, measurement geometry, and wind speed. While these are all treated as independent variables, we contend that in the case of single-station measurements, wind speed is both an inherent uncertainty in the emission rate calculation and may also help reduce uncertainties in measurement geometry. If the SO_2 emission rate is static over short periods of time then it is expected that wind speed should be independent of emission rate, with high wind speeds producing a smaller cross-sectional burden than low wind speed counterparts. Still, in our Cleveland September 2022 – June 2023 dataset of 3216 SO_2 emission rates, we find a Kendall rank correlation coefficient of 0.44 between plume speed and emission rate for an assumed summit plume altitude suggesting at least a moderate degree of correlation between these two variables. When we replicate this analysis using an estimated plume altitude, we find a much lower correlation between wind speed and emission rate to 0.20, suggesting that a large part of the uncertainty related to measurement geometry has been reduced in the case when estimated plume altitudes were used.

We find that for all other datasets, including Cleveland, Korovin, and Gareloi 2019 measurements, wind speeds lower than those which produce a summit altitude plume yielded similar emission rates to those calculated with a summit altitude plume. All three measurement periods calculated using both the estimated and assumed summit plume altitudes are within range of what was measured during helicopter DOAS traverses, though the Korovin Volcano and Cleveland Volcano 2019 emission rate datasets calculated using an estimated plume altitude are in slightly better agreement with helicopter observations' median value. Even for scenarios where the estimated plume altitude method is within error of helicopter DOAS traverses, such as that for Gareloi Volcano, the difference in calculated emission rate is negligible and entirely within the error associated with scanning DOAS data in good conditions (40 – 90%; Kern et al., 2009). When considering the aggregate measurements over the full campaign deployment for each volcano we find better agreement with helicopter DOAS transects when using estimated plume altitude in datasets examined with the exception of the Cleveland Volcano 2019 campaign deployment. Because of the improvement in emission rate using our method for estimating a

plume altitude at varying wind speeds, and generally better agreement with complementary helicopter traverses, we suggest that this approach may be usable in similar geographic conditions to Cleveland volcano (conical island volcanoes), with summit altitude of ~1700 m, when only a single-station scanning DOAS instrument is available. More robust testing at different sites globally should be performed in order to determine if this method can be readily applied to degassing at other volcanoes.

Having developed a method to estimate plume altitude for incorporation into SO_2 cross sectional burden and derived emission rate measurements at Cleveland Volcano, it will be possible to better characterize long-term degassing trends in SO_2 emission rate. Variability in emission rate upwards of an order of magnitude during persistent degassing has been found in other long-term volcanic scanning DOAS datasets in Arellano et al. (2021). For Cleveland, discerning natural variability in measurements from signs of volcanic unrest will become increasingly important now that measurements are collected continuously and at higher temporal resolution than possible through campaign studies (e.g., Werner et al., 2020). When telemetry is restored and a large database of overlapping scans from both permanent scanning DOAS stations (CLNE and CLES) is established, it will be possible to robustly validate our plume altitude estimate method using the geometry of intersecting plume detections. With newly restored access to web cameras at CLNE, it may also be possible to test whether remaining fluctuations in measured emission rate are related to atmospheric scattering due to the presence of condensed plumes or clouds (Galle et al., 2010; Kern et al., 2009) or potentially a change in the volcanic system itself.

4.6.2 Uncertainties in wind speed

Despite the differences in calculated emission rates which may arise from using various methods to determine wind speed, there is no standardized method within the volcanological community to determine wind speed, each group often using the best resource available to them at the time. Both ERA5 and GFS models remain widely in use for scanning DOAS scanning measurements and have a notable advantage of being globally available at high temporal resolution. Other studies may employ the "wind circle" method if done via helicopter or other aircraft (Kern and Kelly, 2023), readings from an anemometer or nearby meteorological station (de Moor et al., 2016), or cross-correlation of SO_2 burden time series at different downwind distances (Johansson et al., 2009b), each with its own advantages and disadvantages with respect to accuracy, precision, and temporal resolution. Corresponding wind circles at Korovin and Gareloi Volcanoes are a helpful validation point for the interpolated modeled wind data during those periods of time and suggest an agreement within ± 22%. It is also important to note that our limited validation helicopter data is only conducted under relatively low windspeeds and validation under high wind speed may not be possible due to the challenges of flying the helicopter through a turbulent plume. Wind speed from ERA5 models perform marginally better than but are mostly comparable to GFS wind speed models (Zhang et al., 2020). Our analysis of both ERA5 and GFS wind speeds in Figure 4.3C

demonstrates nearly identical linear regressions, with ~4 m difference in predicted plume altitude change for each 1 m s^{-1} change in wind speed. The largest discrepancies we find between these models come at either extremely low (<2 m s^{-1}) or high (>15 m s^{-1}) wind speeds, which is also evident in Figure 4.3C. Though we only examine 27 datapoints to extrapolate wind speed, we also down sample ERA5 data to every 3 hours to match GFS forecasts over the entirety of 2022 to find a Spearman correlation coefficient of 0.81, indicating that the datasets are very similar. These findings suggest that existing automated NOVAC analysis procedures incorporating GFS forecasts are adequate for the majority of the year, and that future efforts to provide reanalysis products may yield only marginally different results.

4.7 Cleveland Volcano long-term monitoring

According to the metrics used by AVO for determining volcano alert level, commonly referred to by its color code (detailed in Cameron et al., 2018), Cleveland Volcano was assigned as yellow/advisory during the installation of the CLNE scanning DOAS station in 2022. It remained at yellow/advisory until 5 January 2023, whereupon it was moved to unmonitored due to a long period without any significant periods of detected seismic activity and an insufficient number of operating stations to assign a level of green/normal. Cleveland Volcano then remained unassigned until beyond the period we cover in this study. Through this entire period the AVO weekly updates (www.avo.alaska.edu) list one seismic detection on 23 October 2022 (Magnitude 1.4), one seismic detection on 12 March 2023 (Magnitude 1.9), and regular satellite detections of moderate to barely elevated surface temperatures (qualitative scale). Consistent detections of moderate to barely elevated surface temperatures have been made at Cleveland Volcano during background activity and suggest that, based on the monitoring tools in place, the volcano appears to have been relatively quiet during our study period such that detected changes in volcanic activity cannot obviously explain the high variability in SO_2 emission rates (9 – 1817 t SO_2 day^{-1}) measured during September 2022 – June 2023. During the campaign DOAS deployments in 2019, Cleveland was at yellow/advisory, Korovin was at green/normal, and Gareloi was at green/normal. No anomalous activity above background was noted for our campaign periods, indicating that the scanning DOAS data presented here likely represents background levels of degassing for the monitoring period.

Despite short-term variability in this and other scanning DOAS data (Arellano et al., 2021), monthly trends in emitted SO_2 remain relatively stable and consistent with findings in previous studies. While our method of estimating plume altitude provides one path to provide more accurate measurements, interpreting remaining deviations in emission over time will be a challenge for volcano monitoring. The median average for the entire Cleveland Volcano measurement period of 278 t SO_2 day^{-1} falls within the interquartile range of all months except March and May 2023 (Figure 4.9). The low median SO_2 emission rate in May 2023 of 116 t SO_2 day^{-1} could be due to lower wind speeds than other months covered in the dataset (Table 4.1), which we have found to be less affected by our plume altitude

corrections. March 2023 also has a slightly lower median SO_2 emission rate 163 t SO_2 day^{-1} than other monthly values and much less variance in measured emissions, despite a relatively similar median wind speed to higher emission rate months. It is possible that lowered emissions during March 2023 may be related to an environmental factor scrubbing SO_2 during ascent, such as the reemergence of shallow hydrothermal systems with early spring snowmelt (Symonds et al., 2001). All monthly median values are within range of previous years' studies, including helicopter-based traverses in Werner et al. (2020) collected during 2016 of 324 ± 55 t SO_2 day^{-1} (range 270 – 393; n = 6) and satellite-based mean SO_2 averages in Carn et al. (2017) from 2005 – 2015 of 152 t SO_2 day^{-1} (1σ = 142).

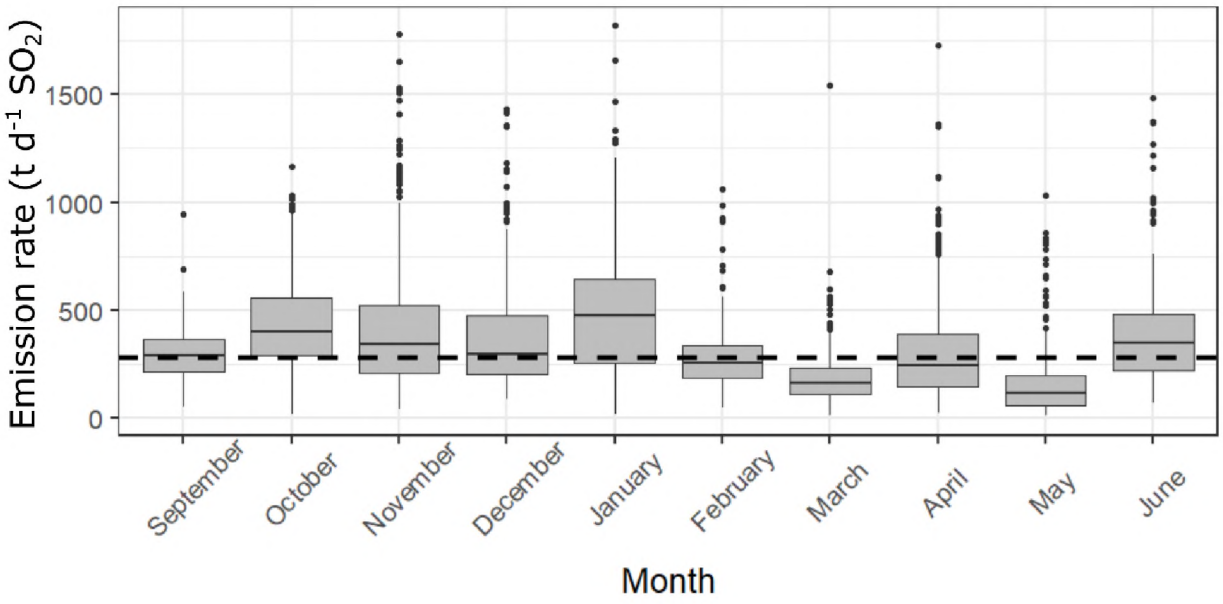

Figure 4.9 Boxplot of monthly SO_2 emission rates from Cleveland Volcano between 13 September 2022 – 7 June 2023 assuming an estimated plume altitude. Mean monthly emission rate is shown as a thick black line within each box, interquartile range is shown as the shaded grey area, and outlying measurements are shown as black dots. The median SO_2 emission rate over the entire measurement period of 278 t SO_2 day^{-1} is presented as a horizontal dashed black line.

4.8 Practical applications in the field

Considering the agreement within error of SO_2 emission rates calculated from single-station scanning DOAS deployments and those calculated from helicopter traverses using an estimated plume altitude based on the method developed here, we believe single-station scanning DOAS instruments can be applied to calculate accurate SO_2 emission rates (to within ~±50%) in situations when other constraints on plume altitude are unavailable. We suggest that our results support deployment of single-station monitoring equipment in scenarios where temporal, environmental, or financial barriers prevent the deployment of multiple stations. In the case of networks with multiple permanent scanning DOAS stations around one volcano, we also suggest that data may be used with confidence in scenarios where

only one scanning DOAS is operational for periods of time due to power outages, or when only one scanning DOAS in a network sees the plume due to wind direction. This new approach to interpreting single-station data provides an opportunity for higher confidence in an inherently variable dataset.

The current structure of real-time monitoring within the NOVAC program is set up to ingest data from each scanning DOAS station with a fixed plume altitude defined by the difference between the instrument GPS elevation and the volcano summit elevation. Geometric solutions for the true plume altitude are only resolved in post-processing when two stations complete scans that detect a plume within 10 minutes of each other. In essence then, without post-processing of data, all scanning DOAS instruments within the NOVAC network may be thought of as operating as single stations with a fixed plume altitude assumption. Because a forecasted wind speed is also ingested into the NOVAC program it may be possible to apply an estimated plume altitude to real-time monitoring data such that it is usable in operational forecasting as data comes in. With a complete network of scanning DOAS instruments at each volcano in the NOVAC network it may be possible to use geometrically resolved altitudes tailored for individual volcanoes.

4.9 Conclusion

Uncertainties related to plume altitude in scanning DOAS scans are understood as a known cause of error in derived SO_2 emission rates. We have developed a method that relates wind speed to plume altitude and identifies a linear correlation that can be applied to other volcanoes with single scanning DOAS instruments to estimate plume altitude for emission rate calculations when this parameter is not constrained via other methods. We have demonstrated that our method of correlating plume altitude to wind speed removes some variability in emission rates for cases with a large range of winds conditions. We find a strong reduction in calculated emission rates during periods of especially high (> 20 m s^{-1}) winds when the plume is expected to be grounded and a small increase in emission rate during periods of low (<11.5 m s^{-1}) winds when the plume is expected to be lofted. Our method for correcting plume altitude using wind speed seems to work well for conical island volcanoes of ~1500 – 1700 m elevation where emitted gases are emitted to the atmosphere passively (at low over-pressure) but should be tested at volcanoes with different morphologies and plume degassing behavior. Our method uses wind data already automatically incorporated into NOVACs real-time processing routine, suggesting that this correction could be implemented for real-time volcano monitoring conducted by observatories.

4.10 Acknowledgements

We would like to acknowledge the Network for Observation of Volcanic and Atmospheric Change (NOVAC) community for providing hardware and software support without which the reported gas measurements would not have been possible. This work was partially funded through U.S. Geological Survey Cooperative Agreement No. G21AC10384. Any use of trade, firm, or product names is for descriptive purposes only and does not imply endorsement by the U.S. Government.

4.11 References

Aiuppa, A., Federico, C., Giudice, G., and Gurrieri, S. (2005). Chemical mapping of a fumarolic field: La Fossa Crater, Vulcano Island (Aeolian Islands, Italy). *Geophysical Research Letters*, 32, L13309. doi:10.1029/2005GL023207.

Arellano, S., Galle, B., Apaza, F., Avard, G., Barrington, C., Bobrowski, N., Bucarey, C., Burbano, V., Burton, M., Chacón, Z., Chigna, G., Clarito, C. J., Conde, V., Costa, F., De Moor, M., Delgado-Granados, H., Di Muro, A., Fernandez, D., Garzón, G., Gunawan, H., Haerani, N., Hansteen, T.H., Hidalgo, S., Inguaggiato, S., Johansson, M., Kern, C., Kihlman, M., Kowalski, P., Masias, P., Montalvo, F., Möller, J., Platt, U., Rivera, C., Saballos, A., Salerno, G., Taisne, B., Vásconez, F., Velásquez, G., Vita, F., and Yalire, M. (2021). Synoptic analysis of a decade of daily measurements of SO_2 emission in the troposphere from volcanoes of the global ground-based Network for Observation of Volcanic and Atmospheric Change, *Earth Systems Science Data*, 13, 1167–1188. doi:10.5194/essd-13-1167-2021.

Bogumil, K., Orphal, J., Homann, T., Voigt, S., Spietz, P., Fleischmann, O., Vogel, A., Hartmann, M., Kromminga, H., and Bovensmann, H. (2003). Measurements of molecular absorption spectra with the SCIAMACHY pre-flight model: Instrument characterization and reference data for atmospheric remote-sensing in the 230–2380 nm region. *Journal of Photochemistry and Photobiology A: Chemistry*, 157(2–3), 167-184. doi:10.1016/S1010-6030(03)00062-5.

Bursik, M. (2001). Effect of wind on the rise height of volcanic plumes. Geophysical Research Letters, 28, 3621-3624. doi:10.1029/2001GL013393.

Cameron, C.E., Prejean, S.G., Coombs, M.L., Wallace, K.L., Power, J.A., and Roman, D.C. (2018). Alaska Volcano Observatory Alert and Forecasting Timeliness: 1989–2017. *Frontiers in Earth Science*, 6(86). doi:10.3389/feart.2018.00086.

Carn, S.A., Fioletov, V.E., McLinden, C.A., Li, C., and Krotkov, N.A. (2017). A decade of global volcanic SO_2 emissions measured from space. *Scientific Reports*, 7, 44095. doi:10.1038/srep44095.

Doukas, M.P. (2002). A new method for GPS-based wind speed determinations during airborne volcanic plume measurements (Open-file report 02-395), U.S. Geological Survey, David A. Johnston Cascades Volcano Observatory.

Edmonds, M., Herd, R.A., Galle, B., and Oppenheimer, C.M. (2003). Automated, high time-resolution measurements of SO_2 flux at Soufrière Hills Volcano, Montserrat. *Bulletin of Volcanology*, 65, 578–586. doi:10.1007/s00445-003-0286-x.

Galle, B., Johansson, M., Rivera, C., Zhang, Y., Kihlman, M., Kern, C., Lehmann, T., Platt, U., Arellano, S., and Hidalgo, S. (2010). Network for Observation of Volcanic and Atmospheric Change (NOVAC)—A global network for volcanic gas monitoring: Network layout and instrument description. *Journal of Geophysical Research*, 115. doi:10.1029/2009JD011823.

Galle, B., Oppenheimer, C., Geyer, A., McGonigle, A.J.S., Edmonds, M., and Horrocks, L. (2002). A miniaturised ultraviolet spectrometer for remote sensing of SO2 fluxes: a new tool for volcano surveillance. *Journal of Volcanology and Geothermal Research*, 119(1–4), 241-254. doi:10.1016/S0377-0273(02)00356-6.

Grainger, J.F., & Ring, J. (1962). Anomalous Fraunhofer line profiles. *Nature*, 193(4817), 762–762. doi:10.1038/193762a0.

Johansson, M. (2009a). Application of Passive DOAS for Studies of Megacity Air Pollution and Volcanic Gas Emissions, PhD thesis, Chalmers University of Technology, Gothenburg, 64 pp.

Johansson, M., Galle, B., Zhang, Y., and Rivera, C. (2009b). The dual-beam mini-DOAS technique–measurements of volcanic gas emission, plume height and plume speed with a single instrument. *Bulletin of Volcanology*, 71, 747–751. doi:10.1007/s00445-008-0260- 8.

Johansson, M. (2021). NOVACProject/NovacPPP: NovacPPP (Post Processing Program) (Version 2.0.0), Zenodo, doi:10.5281/zenodo.4615189.

Kern C. (2009). Spectroscopic measurements of volcanic gas in the ultra-violet wavelength region. PhD Dissertation, University of Heidelberg. 318 pp. doi: 10.11588/heidok.00009574.

Kern, C., and Kelly, P. J. (2023). Weak degassing from remote Alaska volcanoes characterized with a new airborne imaging DOAS instrument and a suite of in situ sensors. *Frontiers in Earth Science*, 11:1088056, 1–22. doi:10.3389/feart.2023.1088056.

Kern C., Lerner, A.H., Elias. T., et al (2020). Quantifying gas emissions associated with the 2018 rift eruption of Kīlauea Volcano using ground-based DOAS measurements. *Bulletin of Volcanology*, 82. doi:10.1007/s00445-020-01390-8

Kraus, S. (2006). DOASIS – A Framework Design for DOAS. PhD Thesis, University of Mannheim. 184 pp.

Kunrat, S., Kern, C., Alfianti, H., and Lerner, A.H. (2022). Forecasting explosions at Sinabung Volcano, Indonesia, based on SO_2 emission rates. *Frontiers in Earth Science*. doi:10.3389/feart.2022.976928.

McGee, K.A. (1992). The structure, dynamics, and chemical composition of noneruptive plumes from Mount St. Helens, 1980–88. *Journal of Volcanology and Geothermal Research*, 51, 269–282.

de Moor, J.M., Aiuppa, A., Avard, G., Wehrmann, H., Dunbar, N., Muller, C., Tamburello, G., Giudice, G., Liuzzo, M., Moretti, R., Conde, V., and Galle, B. (2016). Turmoil at Turrialba Volcano (Costa Rica): Degassing and eruptive processes inferred from high-frequency gas monitoring. *Journal of Geophysical Research: Solid Earth*, 121, 5761–5775. doi:10.1002/2016JB013150.

de Moor, J.M., Kern, C., Avard, G., Muller, C., Aiuppa, A., Saballos, A., Ibarra, A. LaFemina, P., Protti, M., and Fischer, T.P. (2017). A new sulfur and carbon degassing inventory for the Southern Central American Volcanic Arc: The importance of accurate time-series data sets and possible tectonic processes responsible for temporal variations in arc-scale volatile emissions. *Geochemistry, Geophysics, Geosystems*, 18, 4437–4468. doi:10.1002/2017GC007141.

Morton, B.R., Taylor, G.I., and Turner, J.S. (1956). Turbulent gravitational convection from maintained and instantaneous sources. *Proceedings of the Royal Society of London*. A, 234, 1-24. doi:10.1098/rspa.1956.0011.

Platt, U. and Stutz, J. (2008). Differential Optical Absorption Spectroscopy: Principles and Applications; Springer Berlin Heidelberg.

Sparks, R.S.J., Bursik, M.I., Carey, S.N., Gilbert, J.S., Glaze, L., Sigurdsson, H., and Woods, A.W. (1997). Volcanic plumes. John Wiley & Sons, Inc. 557 pages.

Stoiber, R.E., L.L. Malinconico Jr., and S.N. Williams (1983). Use of the correlation spectrometer at volcanoes, Forecasting Volcanic Eruptions, edited by H. Tazieff and J.C. Sabroux pp. 425–444, Elsevier, New York.

Symonds, R.B., Gerlach, T.M., and Reed, M.H. (2001). Magmatic gas scrubbing: implications for volcano monitoring. *Journal of Volcanology and Geothermal Research*, 108(1-4), 303–341. doi:10.1016/S0377-0273(00)00292-4.

Werner, C., Rasmussen, D.J., Plank, T., Kelly, P.J., Kern, C., Lopez, T., Gliss, J., Power, J.A., Roman, D.C., Izbekov, P., and Lyons, J. (2020). Linking subsurface to surface using gas emission and melt inclusion data at Mount Cleveland volcano, Alaska. *Geochemistry, Geophysics, Geosystems*, 125, e2019GC008882. doi:10.1029/2019GC008882.

Vandaele, A.C., Hermans, C., and Fally, S. (2009). Fourier transform measurements of SO_2 absorption cross sections: II.: Temperature dependence in the 29000–44000cm−1 (227–345nm) region. *Journal of Quantitative Spectroscopy and Radiative Transfer*, 110(18), 2115– 2126. doi:10.1016/j.jqsrt.2009.05.006

Zhang, T., Zhao, C., Gong, C., and Pu, Z. (2020). Simulation of Wind Speed Based on Different Driving Datasets and Parameterization Schemes Near Dunhuang Wind Farms in Northwest of China. *Atmosphere*, 11(6), 647. doi:10.3390/atmos11060647.

Chapter 5 Conclusions, implications, and future work

5.1 Conclusions

As the body of research into magmatic volatile phases grows, it is becoming an increasingly important task to accurately measure volcanic gases. The research presented in previous chapters dealt with the quantification of volcanic gas emissions, namely SO_2 and Hg, and demonstrated that quantification of these volcanic gas species may be possible at a higher accuracy and over a wider array of volcanic behavior and atmospheric conditions than previously thought. This dissertation found novel solutions to volcanic gas quantification in some cases where measurements were previously not thought to be possible. Below, I summarize the broad implications of each chapter to the volcanic gas and volcano monitoring communities and discuss clear next steps for impactful research.

5.2 Implications

Chapter 2 provided a novel solution for the lack of Hg measurements from erupting volcanoes. This project was motivated by the large discrepancy between eruptive Hg estimates and those from persistent degassing (Edwards et al., 2021 and references therein). This study developed a new method to gain insight into eruptive Hg emissions through quantification of Hg adsorbed onto volcanic ash. Prior to this study, only small sample sizes of volcanic ash had been analyzed and the rate of Hg adsorbed onto ash was not well understood. The research in this dissertation tested three hypotheses aimed at identifying statistical differences in the concentration of Hg adsorbed onto ash with distance, eruptive event, or between volcanoes. Hg is emitted as a gas, so the eventual depositional trends are dependent on the efficiency of Hg adsorption onto ash or if the conditions facilitating adsorption are present. A gaseous metal emission would be expected to produce a different depositional pattern to other trace metals, which tend to be emitted in the particulate phase and deposit in decreasing concentrations further away from the plume (Ilyinskaya et al., 2021). Second, Hg partitioning was anticipated to be concentrated onto finer ash particles with a larger available surface area, which was predicted to result in higher concentrations of Hg on more distal ash samples (Ermolin et al., 2018). Despite the robust sample sizes of volcanic ash for our target eruptions, no patterns of Hg deposition could be discerned besides those between volcanoes. Because the statistical analysis finds no patterns in Hg concentration on ash with distance or event, it was possible to simplify the process of estimating eruptive Hg mass based on calculated ash masses using only the mean measured Hg concentration on ash.

Chapter 3 provided a framework for estimating the uncertainties, and therefore the utility, of upward-facing DOAS traverse measurements of volcanic SO_2 cross sectional burdens and derived emission rates collected in the presence of below-plume clouds. As an addition, this study also provided a definition of ghost plumes and suggested some atmospheric conditions under which they may be

expected, even showing that ghost plume formation may occur in the presence of small amounts of atmospheric haze. This project was motivated by the prevalence of poor weather conditions while conducting fieldwork in Alaska and built upon earlier work by Kern et al. (2010) to constrain the effects of non-transparent atmospheric and plume conditions on derived SO_2 emission rates. Work in this dissertation used a Monte Carlo radiative transfer model to simulate DOAS measured SO_2 column densities of a volcanic plume under varying geometric, atmospheric, and plume conditions. This study demonstrated that while individual measured column densities may be modified by low-cloud conditions, in many cases—especially for transparent plumes—the total SO_2 cross-sectional burden will remain within 25 % of theoretical. Because the measured and known SO_2 cross sectional burden agreed within a reasonable uncertainty, the calculated SO_2 emission rates can be considered to be representative of the volcanic plume, even when clouds are present between the DOAS instrument and the volcanic plume. This discovery opens the possibility of conducting DOAS traverses in cloudy or foggy weather and allows for more confidence to be placed on these types of datasets. Chapter 3 then explored this effect on a challenging real-world dataset and found that heavy shape modification of the volcanic plumes' measured SO_2 cross-sectional burden may occur even with a thin layer of translucent atmospheric haze above the instrument, indicating that shape modification may be more common than previously thought.

Chapter 4 provided a new method to estimate volcanic plume altitude using modeled wind data, an important input parameter into the equations for calculating SO_2 emission rate from scanning DOAS measurements. This method found that high wind speeds (>11.5 m s^{-1}) yielded grounded plumes, while light wind speeds (<11.5 m s^{-1}) yielded lofted plumes at Cleveland Volcano. These observations were validated against in-situ plume measurements. This study established that proper continuous monitoring of SO_2 is possible from campaign or permanently established single-instrument ground-based scanning DOAS stations. Furthermore, this study provided high-temporal SO_2 emission rates for three days each during campaigns at three remote Alaska volcanoes, and a single permanent scanning DOAS instrument that ran for 9 months in 2022 – 2023 at Cleveland Volcano. These data provided new constraints on the variability in SO_2 emissions at Cleveland Volcano, which is historically very active and often shows minimal geophysical signals of volcanic unrest for the purposes of eruption forecasting. These data can be used to characterize background degassing and better recognize increased gas emissions as a potential sign of volcanic unrest.

5.3 Future work

This dissertation provided several key advances to constrain volcanic gas emissions under challenging or resource-limited conditions. These methods were developed and applied to a subset of primarily Alaska volcanoes. Below, recommendations are made to highlight key opportunities where future work could be conducted.

The methodology employed for Chapter 2 to estimate eruptive Hg flux is not specific to Alaska volcanoes and has broad applicability to improve global Hg eruptive emissions estimates globally if ash samples exist. The methods typically employed to calculate ash eruption masses, requiring a large sample size and ash samples collected, suggest that our method could readily be applied to volcanoes where eruptive mass estimates have been conducted using freshly-preserved ash samples. A National Science Foundation proposal has been submitted to build on chapter 2 with the goal of validating the assumptions pertaining to Hg uptake and retention on deposited volcanic ash samples and further application to Alaska volcanoes. The proposed work is of high relevance since recent work by Koenig et al. (2023) has documented rapid Hg oxidation in the eruptive plume of Piton de la Fournaise, Réunion Island, further validating Chapter 2 findings.

Chapter 3 provided a comprehensive guide to the volcanic gas community for conducting DOAS plume traverses under low-cloud atmospheric conditions. As a real-world example the eruption of Cumbre Vieja included several complexities including no constraints on plume conditions at the time of measurement and exceptionally high SO_2 column densities that prohibited a robust real-world validation of our results. Future validation of this project could include modeling a new set of well-documented DOAS traverses performed under cloudy conditions at a volcano undergoing persistent degassing. While the modification of plume shapes is now better quantified for upward-facing DOAS traverses, questions remain about the modification of plumes during scanning DOAS retrievals of plume cross sectional burden. Future work could theoretically assess the impact of different atmospheric conditions on scanning DOAS within a model space by using the same atmospheric parameters as in chapter 3. Instead of simulating a traverse by iterating through different DOAS positions, it would be possible to simulate a scan by iterating through different DOAS viewing geometries.

Chapter 4 provided a new method to estimate plume altitude, which can significantly increase the accuracy and usability of data acquired from single-station scanning DOAS instrument deployments for quantification of volcanic SO_2 emission rates. The installation of a second scanning DOAS instrument on Cleveland has presented an opportunity to more accurately validate the linear webcam-based relationship between wind speed and plume altitude used in this study. The chapter 4 method was developed empirically using 23 near-coincident airborne volcanic plume measurements and modeled wind data, but further validation would test if this method can be readily applied to other volcanoes. A high-priority future task is therefore to validate the plume altitude constraints estimated here using webcam imagery against the second scanning DOAS instrument now deployed at Cleveland. Additional validation and testing of the method could be possible for other volcano morphologies by using existing data from other volcanoes within the NOVAC network. If applicability at other volcanic sites is shown to be feasible, then

this study makes several recommendations towards how current processing of incoming scans could be altered within the NOVAC program to aid in real-time monitoring efforts.

Prior to establishing permanent scanning DOAS stations at Cleveland Volcano, the only permanent scanning DOAS station installed within the U.S. was at Mt. St. Helens volcano. Of the 57 U.S. volcanoes identified in Ewert et al. (2018) as high priority targets for volcano monitoring, 35 of them are in Alaska and a large subset of those would be relatively good targets for establishing scanning DOAS networks for monitoring volcanic SO_2 emissions. This dissertation shows that remote deployments of single-station scanning DOAS instruments are feasible in the harsh conditions of the Aleutian-Alaska volcanic arc as a proof of concept to expand domestic monitoring capabilities.

5.4 References

Edwards, B.A., Kushner, D.S., Outridge, P.M., and Wang, F. (2021). Fifty years of volcanic mercury emission research: Knowledge gaps and future directions. *Science of the Total Environment,* 757, 143800. doi:10.1016/j.scitotenv.2020.143800

Ermolin, M.S., Fedotov, P.S., Malik, N.A., and Karandashev, V.K. (2018). Nanoparticles of volcanic ash as a carrier for toxic elements on the global scale. *Chemosphere*, 200, 16-22. doi:10.1016/j.chemosphere.2018.02.089

Ewert, J.W., Diefenbach, A.K., and Ramsey, D.W. (2018). 2018 update to the U.S. Geological Survey national volcanic threat assessment. *USGS Scientific Investigations Report* 2018-5140. doi:10.3133/sir20185140

Ilyinskaya, E., Mason, E., Wieser, P.E., Holland, L., Liu, E.J., Mather, T.A., Edmonds, M., Whitty, R.C., Elias, T., Nadeau, P.A., Schneider, D., McQuaid, J.B., Allen, S.E., Harvey, J., Oppenheimer, C., Kern, C., and Damby, D. (2021). Rapid metal pollutant deposition from the volcanic plume of Kīlauea, Hawai'i. *Communications Earth & Environment*, 2, 78. doi:10.1038/s43247-021-001462

Kern, C., Deutschmann, T., Vogel, L., Wöhrbach, M., Wagner, T., and Platt, U. (2010). Radiative transfer corrections for accurate spectroscopic measurements of volcanic gas emissions. *Bulletin of Volcanology*, 72, 233-247. doi:10.1007/s00445-009-0313-7.

Koenig, A.M., Magand, O., Rose, C., Muro, A.D., Miyazaki, Y., Colomb, A., Rissanen, M., Lee., C.F., Koenig, T.K., Volkamer, R., Brioude, J., Verreyken, B., Roberts, T., Edwards, B.A., Sellegri, K., Arellano, S., Kowalski, P., Aiuppa, A., Sonke, J.E., and Dommergue, A. (2023). Observed in-plume gaseous elemental mercury depletion suggests significant mercury scavenging by volcanic aerosols. *Environmental Science: Atmospheres*. doi:10.1039/d3ea00063j